UNIVERSITY OF CALIFORNIA SAN DIEGO

Performance Analysis of an Ultra-Low Power MFSK System

A dissertation submitted in partial satisfaction of the
requirements for the degree
Doctor of Philosophy

in

Electrical Engineering
(Communication Theory and Systems)

by

Yi Xiang

Committee in charge:

Professor Laurence B. Milstein, Chair
Professor Patrick J. Fitzsimmons
Professor Patrick P. Mercier
Professor Paul H. Siegel

2022

The thesis of Yi Xiang is approved, and it is acceptable in quality and form for publication on microfilm and electronically.

University of California San Diego

2022

DEDICATION

To my beloved family.

TABLE OF CONTENTS

LIST OF FIGURES

LIST OF TABLES

ACKNOWLEDGEMENTS

First and foremost, I am eternally grateful to my advisor Professor Laurence B. Milstein for his guidance and support throughout my Ph.D. journey. Without him, my Ph.D. journey wouldn't have been so smooth and pleasant.

I really appreciate the help and feedback from my committee members Professor Patrick Fitzsimmons, Professor Patrick Mercier, Professor Paul Siegel and Professor Alexander Vardy on my qualifying and/or defense exams.

I would like to thank my past and current lab mates, Jianze Mao, Yishen Yeh, Turki Alkhamees, Ziyu Ye, just to name a few, for their help and support.

I am grateful to my family members and my girlfriend, Fan Mo, for their company and support during the global pandemic.

The text of Chapter 2 is, in part, a reprint of the paper, Y. Xiang and L. B. Milstein, "Design and Performance Analysis for Short Range, Very Low-Power Communications," in *IEEE Transactions on Communications*, vol. 68, no. 9, pp. 5938-5950, Sept. 2020, doi: 10.1109/TCOMM.2020.3005454. The dissertation author is the primary researcher and author of the paper.

The text of Chapter 3 is, in part, a reprint of the papers, Y. Xiang and L. B. Milstein, "Design of an ultra-low power MFSK system in the presence of jamming," MILCOM 2021 - 2021 IEEE Military Communications Conference (MILCOM), 2021, pp. 652-657, doi: 10.1109/MILCOM52596.2021.9653041, and "On the use of FFH-MFSK for ultra-low power communications", submitted to *IEEE Transactions on Vehicular Technology*. The dissertation author is the primary researcher and author of these papers.

The text of Chapter 4 is, in part, a reprint of the paper, "Performance analysis for an ultra-low power GFSK system", submitted to *IEEE Transactions on Communications*. The dissertation author is the primary researcher and author of the paper.

VITA

2017	B. S. in Electrical Engineering, University of California San Diego
2019	M. S. in Electrical Engineering (Communications theory and systems), University of California San Diego
2022	Ph. D.in Electrical Engineering (Communications theory and systems), University of California San Diego

PUBLICATIONS

Y. Xiang and L. B. Milstein, "Design and Performance Analysis for Short Range, Very Low-Power Communications," in *IEEE Transactions on Communications*, vol. 68, no. 9, pp. 5938-5950, Sept. 2020, doi: 10.1109/TCOMM.2020.3005454.

Y. Xiang and L. B. Milstein, "Design of an ultra-low power MFSK system in the presence of jamming," MILCOM 2021 - 2021 IEEE Military Communications Conference (MILCOM), 2021, pp. 652-657, doi: 10.1109/MILCOM52596.2021.9653041.

Y. Xiang and L. B. Milstein, "On the use of FFH-MFSK for ultra-low power communications", submitted to *IEEE Transactions on Vehicular Technology*.

Y. Xiang and L. B. Milstein, "Performance analysis for an ultra-low power GFSK system", submitted to *IEEE Transactions on Communications*.

ABSTRACT OF THE DISSERTATION

Performance Analysis of an Ultra-Low Power MFSK System

by

Yi Xiang

Doctor of Philosophy in Electrical Engineering
(Communication Theory and Systems)

University of California San Diego, 2022

Professor Laurence B. Milstein, Chair

In this dissertation, we investigate the problem of designing an ultra-low power M-ary frequency shift keying (MFSK) system. In Chapter 2, we design a communication system that operates under stringent power constraints, but is flexible with bandwidth constraints. Our approach is to consider some of the key elements in a transceiver and optimize them for low power consumption, as opposed to optimizing them to minimize, say, average probability of error. An obvious consequence of this is that high complexity components of the system, such as matched filters, forward error correction that employs iterative decoders, coherent demodulators, and bandwidth-efficient modulation formats, are not feasible for this research. Rather, our system

is designed using MFSK with non-coherent detection, optimized two-pole bandpass filters (BPFs), and Reed-Solomon (RS) codes with hard-decision decoding. Among other things, we show that by properly optimizing the key parameters of the BPFs and RS codes, we can design the system to be significantly less complex than an optimal one, and only lose about 1.2 dB in terms of performance.

In Chapter 3, we extend the results from Chapter 2 to incorporate fast frequency hopping (FFH) and intelligent jamming. The system still operates under stringent power constraints, but is flexible with bandwidth constraints. Our system is designed using MFSK with non-coherent detection and FFH, optimized two-pole BPFs, and RS codes with hard-decision decoding. Among other things, we show that by properly optimizing the key parameters of the BPFs and RS codes, we can design the system to be significantly less complex than the MF system with a performance loss of less than 1.4 dB in terms of performance in most scenarios that we considered. Further, the 2-pole BPF system can actually outperform the corresponding MF system by up to 2.4 dB with multi-tone jamming.

In Chapter 4, we extend the results from Chapter 2 to incorporate Gaussian filtering. We improve our previous design by considering the power-bandwidth tradeoff, and we show that we can save a large percentage of system bandwidth by sacrificing a small amount of power, when the demodulator and coding parameters are optimized. For example, we can save 50% of system bandwidth at the cost of 1 dB loss in performance compared to our previous system design. We quantify the performance loss as a function of both the system bandwidth saved and the time-bandwidth product of the Gaussian filter. We keep $M = 16$ as our baseline design, and compare the performance of the M-ary GFSK system with the corresponding MFSK system.

Chapter 1

Introduction

1.1 MFSK System Operating with Ultra-low Power Consumption

The motivation for this research is the need for low-power communications systems that yield good performance at very low power levels. Examples of the need for such systems vary from reducing the size and weight of batteries used by foot soldiers who carry tens of pounds of equipment in their backpacks, to various low-power internet-of-things (IoT) applications that have a wide spread of applications from wearable fitness trackers to transportation, healthcare, consumer electronics and many others [1] -[3]. Note that with very stringent power constraints, many of the routine functions in a communications systems have to be carefully chosen. For example, some types of forward error correction (FEC) that rely upon complex decoders, such as those employing iterative decoding, would be unacceptable because of power consumption at the decoder.

To make such a system plausible, we assume that, while power is a very scarce resource, bandwidth is not. Similarly, while most systems use as a design criterion that of optimizing the receiver so as to minimize, say, the average probability of bit error, our approach is to use ad

hoc designs based upon power consumption, and optimize the key components of the resulting suboptimal receivers.

According to a survey that studies recent ultra-low power receivers [4, Fig.4], nearly all low-power receivers (whose power is $<$1mW) use non-coherent modulation techniques. Most designs use either envelope detection based On-Off keying (OOK) or binary non-coherent FSK [5]. Coherent communication requires significantly higher power to demodulate the received waveform because the carrier phase has to be accurately tracked to enable low BER detection, and thus a phase lock loop (PLL) is necessary in the receiver [4]. The problem is that, to the best of our knowledge, the state-of-the-art in power consumption of PLLs that have sufficiently low levels of phase noise is 550 microwatts [6], meaning the PLL of a coherent receiver alone requires more than 50% of our total budget of 1 mW. As a result, rather than looking for modulation formats that are bandwidth efficient, such as the commonly used MQAM and MPSK, we limited our modulation techniques to those that are power efficient, such as orthogonal MFSK. Similarly, regarding the filtering at the receiver, rather than attempting to implement a matched filter, we chose the simplest type of bandpass filter (BPF) we are aware of, which was a two-pole BPF. For the same reason, we limited our FEC to Reed-Solomon block codes with hard-decision decoding. While Reed-Solomon codes with soft-decision decoding are seldom used with non-coherent MFSK, a non-coherent MFSK system with Reed-Solomon codes and hybrid soft decision-hard decision decoding has been shown to have an additional coding gain of a fraction of a dB compared to hard decision decoding [7].

The total power consumption consists of both transmission power and circuit power, and references such as [8] -[11] consider jointly optimizing the tradeoff between the two. As an example, it is found that 80% of power saving is achievable by optimizing transmission time and modulation parameters [11]. In this paper, we consider only minimizing transmission power, subject to a given level of performance.

The demodulator consists of a parallel bank of M branches, each with a BPF whose center

frequency is the frequency of the corresponding tone, followed by an envelope detector and a sampler, and we choose the largest among the M test statistics from the samplers to make a decision. As a point of comparison, this structure, if used with matched filters, is the optimal non-coherent receiver when the input waveform does not have phase continuity at the symbol transition times (i.e., the phase of each pulse is i.i.d. with a uniform pdf from 0 to 2π). The performance of this optimal structure in comparison with some other modulation techniques in flat Rician fading channels is analyzed in [12], and the performance analysis for non-coherent orthogonal BFSK in correlated Rician channels is presented in [13]. We reduce the complexity of this structure by using 2-pole BPFs at the price of sacrificing some performance.

The problem with 2-pole BPFs is that they are non-orthogonal, and they cause both inter-carrier interference (ICI) and inter-symbol interference (ISI). Our goal is to optimize modulation parameters (filter bandwidth, tone spacing and sampling time) in the presence of ICI and ISI to achieve the best system performance, i.e., to minimize the E_b/N_0 (or SNR per bit) required to reach a certain probability of error. In this paper, we choose the symbol error rate (SER) $P_s = 10^{-3}$ for an uncoded system and bit error rate $P_b = 10^{-5}$ for a coded system. We consider two types of channels: additive white Gaussian noise (AWGN) channels and Rician fading channels (including Rayleigh fading channels as a special case).

1.2 FFH-MFSK System operating in the Presence of Intelligent Jamming for Ultra-low Power Communications

Frequency-hopping spread-spectrum (FHSS) frequency shift keying (FSK) is widely used in military communication systems because of its anti-jamming capability. In particular, fast FH with M-ary FSK (FFH/MFSK) is a typical non-coherent communication scheme with the potential for applications in both military and civilian communication systems [19]–[22]. Among the intelligent jamming strategies are partial-band noise jamming (PBJ) and multi-tone

jamming (MTJ). Attempts have been made to study and combat various intelligent jammers and interferences in different channel conditions with appropriate signal selection and error-correction coding [22]–[30]. The combined effects of diversity and coding to combat MTJ in a Rayleigh fading channel are studied in [22]; the performance of an optimal ML receiver in PBJ and frequency-selective Rician fading channels is derived in [23]; the composite effect of MTJ and PBJ in a Rayleigh fading channel with time and frequency offsets is analyzed in [24]; the performances of an FFH/MFSK system with various receivers under MTJ are compared in [25], [26]. The performance of an FFH/BFSK system with a suboptimal ML receiver under MTJ in frequency-selective Rayleigh fading channels is studied in [27]. The performance of an FFH/MFSK system with product combining under PBJ in Rayleigh fading channels is analyzed in [28]. The use of RS codes to combat PBJ and MTJ in a slow FH system is studied in [29], [30]. The use of index modulation based FHSS to combat a reactive symbol-level jammer is proposed in [31]. The design of waveforms to mitigate the effect of single tone jamming signals in time hopping SS systems is studied in [32]. The effect of phase noise in the frequency synthesizer on an FFH/MFSK system is analyzed in [33].

In [34], we addressed the design and performance analysis of an ultra-low power communications system. As a concrete example of constraints that ultra-low power consumption impose on system design, such as in [34], consider a scenario where it is required to communicate over a range of at least 1km, with a data rate of at least 100kb/sec, and an uncoded bit error rate (BER) of 10^{-3} or less, in an AWGN channel, subject to a total power constraint, which includes both transmitter and receiver power consumption, as well as the power consumption required for transmission, of 1mW [35].

However, what was missing from [34] was the presence of intelligent jammers. Therefore, in this chapter, we add the presence of a partial-band jammer which maximizes the performance degradation by optimizing the fraction of total spread spectrum bandwidth jammed. We also add the presence of a multi-tone jammer which maximizes the performance degradation by optimizing

the amount of power in each jammed slot. Further, we revise our system design to include FFH.

1.3 M-ary GFSK System in Ultra-low Power Communications

In Gaussian FSK (GFSK) modulation, a Gaussian filter is used to reshape the transmitted signal, resulting in a smoother transition between symbols, and thus decreasing out-of-band spectrum. GFSK is frequently used in applications such as Bluetooth receivers [47] – [50]. Attempts have been made to study and implement GFSK receivers for the purpose of reducing power consumption and improving system performance. A mixed-signal GFSK demodulator was proposed in [50], with a power consumption of 6 mW, which can tolerate up to 200 kHz frequency offset at a 2 MHz intermediate frequency. A GFSK receiver with an ultra-low power consumption based on injection-locking was presented in [49], achieving a power consumption of 1.8 mW, and a Bluetooth GFSK data rate of 1Mb/s. GFSK demodulators with large frequency offset tolerance between the transmitter and receiver were proposed in [48]. An optimized differential GFSK demodulator that outperforms conventional differential demodulators was developed in [47]. The use of GFSK with frequency hopping spread spectrum (FHSS-GFSK) to detect drone communication signals in a non-cooperative scenario was proposed in [53]. The theoretical performance of a FHSS-GFSK system considering the effect of a post-detection filter was calculated in [54].

While we used orthogonal signaling in [34] and [43] for optimal performance, in this chapter, we study the power-bandwidth tradeoff for the system proposed in [34], by employing Gaussian filtering. We show that we can save a large fraction of bandwidth at the cost of a small performance degradation, when all the parameters of the demodulator and code are optimized for the proposed M-ary GFSK systems.

Chapter 2

Design and performance analysis for short range, very low-power communications

2.1 Demodulator performance in AWGN channel

In this section, we analyze the performance of an MFSK non-coherent demodulator in an AWGN channel. We first find the optimal performance when we use 2-pole BPFs under the idealized condition of no interference. We will see that with continuous phase, we can derive a closed-form formula to calculate symbol error rate. We also find the demodulator performance when the signal phase is not continuous. Note that both of these latter two results incorporate all sources of degradations, including ICI and ISI.

2.1.1 System model

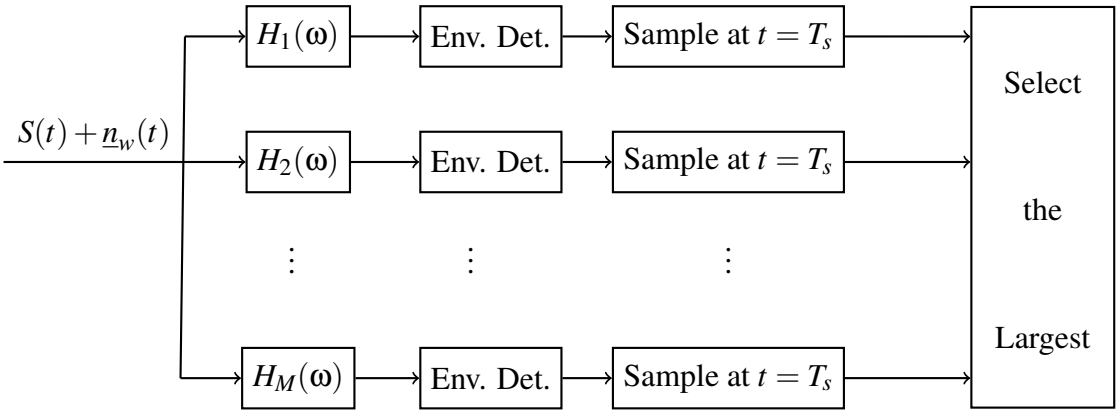

Figure 2.1: MFSK non-coherent demodulator

The block diagram of an MFSK non-coherent demodulator structure is shown in Fig. 2.1, where $\underline{n}_w(t)$ is additive white Gaussian noise with single-sided power spectral density N_0, T_s is the duration of time from the start of any pulse to the time when that pulse is sampled (as part of the test statistic), and the dehopped signal $S(t)$ is given by

$$S(t) = \sum_{l=1}^{\infty} AP_{\frac{T}{2}}(t-(l-1)T-\frac{T}{2})\cos(2\pi f^{(l)}[t-(l-1)T]+\underline{\theta}_l), \tag{2.1}$$

where A is the pulse amplitude, and T is the pulse duration, so that the bit energy is given by $E_b = A^2T/2$, and

$$P_a(x) \triangleq \begin{cases} 1, & |x| \leqslant a, \\ 0, & \text{elsewhere.} \end{cases} \tag{2.2}$$

Also, $\underline{\theta}_l$ is the random phase associated with the l^{th} pulse, and is uniformly distributed between 0 and 2π, and $f^{(l)}$ is the carrier frequency of the l^{th} pulse. Note that

$$f^{(l)} \in \{f_1, f_2, \ldots, f_M\}, \quad l = 1,2,3,\ldots \tag{2.3}$$

where $f_1, \cdots, f_M$ are the center frequencies of each tone, and the filters are 2-pole BPFs with transfer function and corresponding impulse response

$$\begin{aligned} H_i(s) &= \frac{2\pi W s}{s^2 + 2\pi W s + (2\pi f_i)^2} \quad i = 1,2,\ldots,M, \\ h_i(t) &= 2\pi W e^{-\pi W t}\cos(2\pi f_i t)u(t) \quad i = 1,2,\ldots,M. \end{aligned} \tag{2.4}$$

respectively, where W is the filter bandwidth and $\Delta f \triangleq f_2 - f_1$ is the tone spacing. We assumed $f_i \gg W, \forall i$ when we derived the impulse response from the transfer function. The goal is to minimize E_b/N_0 required to reach a certain level of symbol error rate, P_s. The parameters we optimize are the time-bandwidth parameter, z, the modulation index, h. and ratio between T_s and T, r, defined as

$$z = W \cdot T, \quad h = \Delta f \cdot T, \quad r = T_s/T. \tag{2.5}$$

2.1.2 Idealized baseline system

In this subsection, we initially present the performance of BFSK in an AWGN channel, assuming we use 2-pole BPFs, but ignore the effects of interference. With those simplifications, we only optimize the parameter z in (2.5). The resulting performance will be used as a baseline for comparison to realistic models in Sections II, III and IV. Without loss of generality, assuming that frequency f_1 is transmitted, the bandpass transmitted signal is given by

$$s_1(t) = A\cos(2\pi f_1 t + \underline{\theta})P_{\frac{T}{2}}(t - \frac{T}{2}). \tag{2.6}$$

The output of $H_1(\omega)$ is

$$x_1(t) = s_1(t) * h_1(t) = \begin{cases} A(1-e^{-\pi Wt})\cos(2\pi f_1 t + \underline{\theta}), & 0 \leqslant t \leqslant T, \\ A(e^{\pi WT}-1)e^{-\pi Wt}\cos(2\pi f_1 t + \underline{\theta}) & t \geqslant T. \end{cases} \tag{2.7}$$

Finally, after the envelope detector and sampler, the noiseless test statistic $g_1(T)$ is

$$g_1(T) = A(1-e^{-\pi WT}) = A(1-e^{-\pi z}). \tag{2.8}$$

The noise power, after filtering, is easily shown to be $\sigma^2 = \frac{N_0 \pi W}{2}$, and the bit error rate is

$$P_{s,2-pole} = \frac{1}{2}e^{-\frac{g_1(T)^2}{4\sigma^2}} = \frac{1}{2}e^{-\frac{E_b}{2N_0}\frac{2(1-e^{-\pi z})^2}{\pi z}} \triangleq \frac{1}{2}e^{-\frac{E_b}{2N_0}\cdot\frac{1}{f(z)}}. \tag{2.9}$$

Since the performance of a matched filter system is

$$P_{s,MF} = \frac{1}{2}e^{-\frac{E_b}{2N_0}}. \tag{2.10}$$

the performance loss by using the 2-pole filter is

$$f(z) = \frac{\pi z}{2(1-e^{-\pi z})^2}. \tag{2.11}$$

We find the minimum of $f(z)$, in dB, as shown in Fig. 2.2. The optimal parameter is seen in Fig. 2.2 to be $z = 0.4$, and the minimal performance loss is 0.89dB. Figure 2.3 compares the performance results.

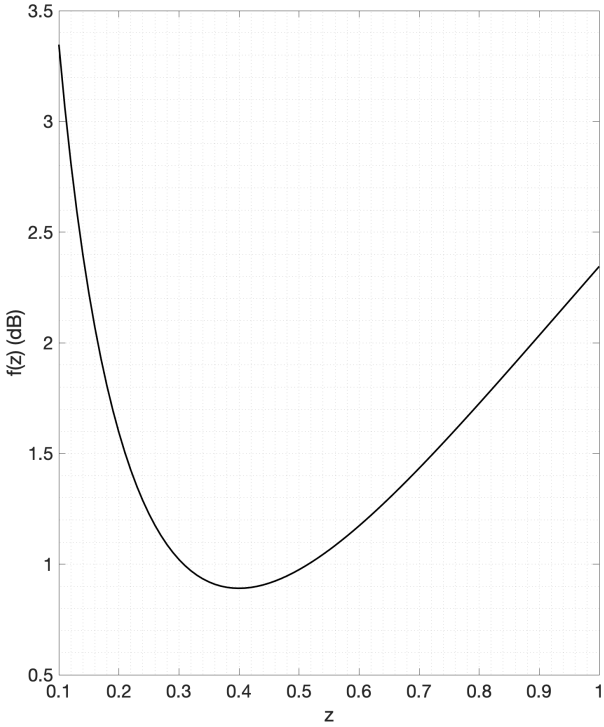

Figure 2.2: Performance loss vs. z

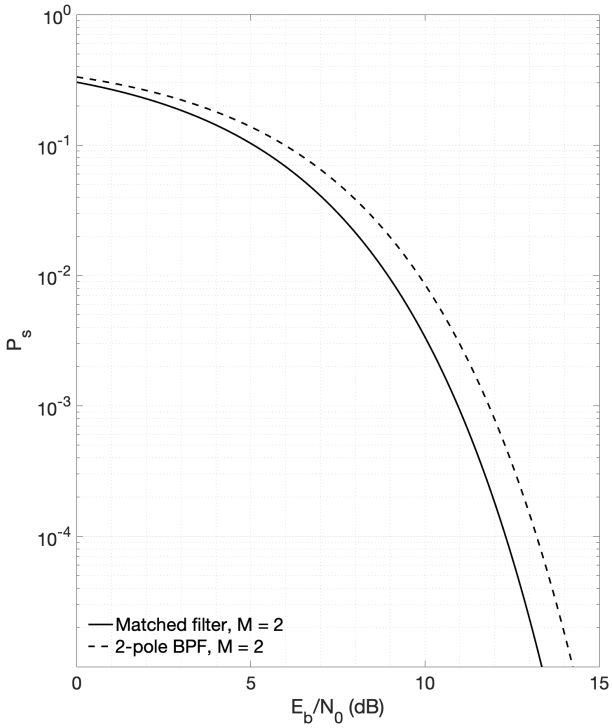

Figure 2.3: Optimal performance w/o interference

The result shown above is for BFSK, but it can be easily generalized to MFSK. From chapter 4 of [14], the symbol error rate of MFSK with non-coherent matched filters detection is

$$P_{s,MF} = \sum_{n=1}^{M-1} \frac{(-1)^{n+1}}{n+1} \binom{M-1}{n} e^{-\frac{n\log_2 M}{n+1}\frac{E_b}{N_0}}. \tag{2.12}$$

The symbol error rate of MFSK with non-coherent detection with 2-pole BPFs, when ignoring interference, is given by

$$P_{s,2-pole} = \sum_{n=1}^{M-1} \frac{(-1)^{n+1}}{n+1} \binom{M-1}{n} e^{-\frac{n\log_2 M}{n+1}\frac{E_b}{N_0}\cdot\frac{1}{f(z)}}, \tag{2.13}$$

where $f(z)$ is defined in (2.11).

2.1.3 Demodulator performance with continuous phase in an AWGN channel

In this subsection, we analyze the system performance in an AWGN channel, assuming we have continuous phase between pulses. To be specific, the goal is to find the optimal 3-tuple: (z,h,r), at a given symbol error rate ($P_s = 10^{-3}$). We first consider non-orthogonal tone spacing and arbitrary sampling time. We then consider the special case of orthogonal signaling ($h \in \mathbb{I}^+$) and sampling at the end of the pulse ($r = 1$). Finally, we compare the results and see how much is the gain that non-orthogonal signaling can yield.

Non-orthogonal signaling

As we will see in Section V, Figs. 2.4 and 2.7, the analysis that accounts for ISI only from the previous pulse matches very well with simulation results that incorporate many previous pulses. Hence, in this section, we consider only the previous pulse as the source of ISI. Consider detecting the symbol number p in the pulse train, with the demodulator shown in Fig. 2.1. We

define in (2.14) $s_i^m(t)$, which consists only of the pulses number p and $p-1$, where the frequency of the pulses numbered p and $p-1$ are f_i and f_m, respectively:

$$\begin{aligned} s_i^m(t) \triangleq & AP_{\frac{T}{2}}(t-\frac{T}{2}-(p-1)T)\cdot\cos(2\pi f_i[t-(p-1)T]+\theta_p)+ \\ & AP_{\frac{T}{2}}(t-\frac{T}{2}-(p-2)T)\cdot\cos(2\pi f_m[t-(p-2)T]+\theta_{p-1}). \end{aligned} \tag{2.14}$$

where $i,m \in \{1,2,\ldots,M\}$. To achieve phase continuity, the relationship between θ_p and θ_{p-1} is $\theta_p = \theta_{p-1} + 2\pi f_m T \mod 2\pi$. Without loss of generality, we assume $\theta_{p-1} = 0$ and thus $\theta_p = 2\pi f_m T$, and the sampling time to detect the pulse number p is $T' = (p-1)T + T_s$. Let Ps_{in}^m denote the probability that the current symbol (number p) is at frequency f_i but is detected as $f_n, n \neq i$, and where the previous symbol is at frequency f_m. Then the *union bound* on the average symbol error rate is

$$\bar{P}_s = \frac{1}{M^2}\sum_{i=1}^{M}\sum_{n=1,n\neq i}^{M}\sum_{m=1}^{M} Ps_{in}^m. \tag{2.15}$$

By symmetry, the above equation can be simplified to

$$\bar{P}_s = \frac{2}{M^2}\sum_{i=1}^{M/2}\sum_{n=1,n\neq i}^{M}\sum_{m=1}^{M} Ps_{in}^m, \tag{2.16}$$

where, from chapter 9 of [15],

$$Ps_{in}^m = \frac{1}{2}\left[1 - Q(\sqrt{b_{in}^m}, \sqrt{a_{in}^m}) + Q(\sqrt{a_{in}^m}, \sqrt{b_{in}^m})\right], \tag{2.17}$$

and

$$\begin{Bmatrix} a_{in}^m \\ b_{in}^m \end{Bmatrix} = \frac{1}{2\sigma^2}\left[\frac{\frac{A_1^2+A_2^2}{2} - 2|\rho_{in}|\sqrt{\frac{A_1^2}{2}\frac{A_2^2}{2}}\cos(\theta_1-\theta_2+\phi_{in})}{1-|\rho_{in}|^2} \mp \frac{\frac{A_1^2}{2}-\frac{A_2^2}{2}}{\sqrt{1-|\rho_{in}|^2}}\right]. \tag{2.18}$$

In (2.17), the $Q(\cdot,\cdot)$ is the Marcum-Q function, defined as

$$Q(a,b) = \int_b^\infty x e^{-\frac{x^2+a^2}{2}} I_0(ax) dx, \tag{2.19}$$

where $I_0(\cdot)$ is the modified Bessel function, defined as

$$I_0(x) = \frac{1}{2\pi} \int_{-\pi}^{\pi} e^x \cos\theta d\theta. \tag{2.20}$$

The parameters are defined as follows: A_1 and A_2 are signal amplitudes at the output of the filters $H_i(\omega)$ and $H_n(\omega)$, respectively, θ_1 and θ_2 are the corresponding phases; ρ_{in} is the normalized complex cross-covariance between the two complex Gaussian processes, and σ^2 is the noise power at the output of any filter. Detailed analysis can be found in Appendix A.

We do a 3D optimization to find the optimal 3-tuple (at the symbol error rate $P_s = 10^{-3}$) of (z,h,r). The optimal performance curves for $M = 2$ and 16 are shown in Fig. 2.4 and Fig. 2.5, respectively, in Section 2.4. We compare results from analysis and simulation, where we collected 1000 errors for each data point in the simulation.

Orthogonal signaling

In this section, we consider the special case of orthogonal signaling and sampling at the end of each pulse ($r = 1$). We assume that $2\pi f_i = \frac{2n_i\pi}{T}, \quad n_i \in \mathbb{I}^+ \Rightarrow f_i = \frac{n_i}{T}$. Therefore, the tone spacing is

$$\Delta f = |f_2 - f_1| = \left|\frac{n_2}{T} - \frac{n_1}{T}\right| = \frac{|n_2 - n_1|}{T}, \quad n_1, n_2 \in \mathbb{I}^+. \tag{2.21}$$

This can be simplified to $h = \Delta f T \in \mathbb{I}^+$. Note that for spectral efficiency, the positive integer h is often chosen to be 1, and phase continuity with orthogonal signaling simply means $\theta_1 = \theta_2 = \theta_3 = \cdots \triangleq \theta$.

Since orthogonal signaling is a special case of non-orthogonal signaling, and sampling at the end of each pulse is a special case of sampling at an arbitrary time, the analysis in the previous subsection still applies here. It can be greatly simplified though, as shown in Appendix B.1.

Assuming we choose the minimum tone spacing satisfying orthogonal signaling, that is, $h = \Delta f T = 1$, then we are left with only one variable to optimize with respect to, namely, the time-bandwidth parameter, $z = WT$. We do an exhaustive search to find the optimal z for MFSK for $M = 2, 4, 8, 16$ and 32 at symbol error rate $P_s = 10^{-3}$. The E_b/N_0 required by a matched filter and a 2-pole BPF, along with the optimal parameter z, are shown in Table 2.1.

Table 2.1: Optimal parameter z and performance when $h = 1$

Filter \ M	2	4	8	16	32
MF	10.95	8.60	7.30	6.40	5.75
2-pole	11.73	9.69	8.48	7.60	6.94
z_{opt}	0.6	0.56	0.54	0.52	0.5

The comparison between orthogonal signaling and non-orthogonal signaling is shown is Fig. 2.6 in Section 2.4. As we can see, there is not much room for improvement by using non-orthogonal signaling, especially when M is large.

The analysis here holds for general M. As a special case, when $M = 2$, it reduces to BFSK, where symbol error rate P_s equals bit error rate P_b. From (2.16), we have for $M = 2$

$$P_s = P_b = \frac{2}{M^2} \sum_{i=1}^{M/2} \sum_{n=1, n\neq i}^{M} \sum_{m=1}^{M} Ps_{in}^m = \frac{1}{2}\left(Ps_{12}^1 + Ps_{12}^2\right). \tag{2.22}$$

From (2.17),

$$Ps_{12}^m = \frac{1}{2}\left[1 - Q(\sqrt{b_{12}^m}, \sqrt{a_{12}^m}) + Q(\sqrt{a_{12}^m}, \sqrt{b_{12}^m})\right], \tag{2.23}$$

where

$$\begin{Bmatrix} a_{12}^1 \\ b_{12}^1 \end{Bmatrix} = \frac{E_b}{N_0} \cdot \frac{2(1-e^{-2\pi z})^2(\sqrt{k^2+z^2} \mp k)^2}{\pi z(4k^2+z^2)}, \tag{2.24}$$

and

$$\begin{Bmatrix} a_{12}^2 \\ b_{12}^2 \end{Bmatrix} = \frac{E_b}{N_0} \cdot \frac{2(1-e^{-\pi z})^2}{\pi z(4k^2+z^2)} \cdot \{[\sqrt{k^2+z^2}(1+e^{-\pi z}) \mp k(1-e^{-\pi z})]^2 - \frac{16k^2z^2e^{-\pi z}}{4k^2+z^2}\}, \tag{2.25}$$

as shown in Appendix B.2.

2.1.4 Demodulator performance with discontinuous phase in an AWGN channel

In this subsection, we analyze the system performance in an AWGN channel, assuming we have discontinuous phase between pulses. The goal is still to find the optimal 3-tuple: (z,h,r) defined in (2.5). We then compare the results with those from Section 2.1.3 and see how much is the gain the phase continuity can yield. We will only consider the more general case of non-orthogonal signaling here.

The definition of discontinuous phase is straightforward: the phase associated with each pulse is i.i.d. uniformly distributed between 0 and 2π. The waveform is, in general, discontinuous at the boundary between consecutive pulses. Mathematically, if $\underline{\theta}_p$ is the phase associated with the p^{th} pulse, then $\underline{\theta}_p \sim U[0,2\pi], \forall p$.

The analysis for the symbol error rate is similar to Section 2.1.3. We let $Ps_{in}^m(\theta_p)$ denote the probability that the current symbol is at frequency f_i but is detected as $f_n, n \neq i$, where the previous symbol is at frequency f_m, given that the phase associated with the pulse number p is θ_p (we still assume the phase associated with the pulse number $p-1$ is $\theta_{p-1} = 0$). Then the union

bound on the average symbol error rate is

$$\bar{P}_s = \frac{1}{M^2} \sum_{i=1}^{M} \sum_{n=1,n\neq i}^{M} \sum_{m=1}^{M} \left[\int_0^{2\pi} Ps_{in}^m(\theta_p) d\theta_p \right]. \tag{2.26}$$

By symmetry, the above equation can be simplified to

$$\bar{P}_s = \frac{2}{M^2} \sum_{i=1}^{M/2} \sum_{n=1,n\neq i}^{M} \sum_{m=1}^{M} \left[\int_0^{2\pi} Ps_{in}^m(\theta_p) d\theta_p \right], \tag{2.27}$$

where

$$Ps_{in}^m(\theta_p) = \frac{1}{2} \left[1 - Q(\sqrt{b_{in}^m(\theta_p)}, \sqrt{a_{in}^m(\theta_p)}) + Q(\sqrt{a_{in}^m(\theta_p)}, \sqrt{b_{in}^m(\theta_p)}) \right], \tag{2.28}$$

and where $a_{in}^m(\theta_p)$ and $b_{in}^m(\theta_p)$ are defined in (2.18), except that some parameters are now functions of θ_p.

Again, we do a 3D optimization to find the optimal 3-tuple. The optimal performance curves for $M = 2$ and 16 are shown in Fig. 2.7 and Fig. 2.8, respectively, in Section 2.4. Note that we are always better off with phase continuity, but the difference between the two cases decreases with alphabet size M, and is smaller than 0.2 dB at $M = 16$, as shown in Fig. 2.9.

2.2 Demodulator performance in flat, slow Rician fading channels

In a Rician fading channel, pulse train $\underline{S}(t)$ is given by

$$\underline{S}(t) = \sum_{l=1}^{\infty} \underline{R} P_{\frac{T}{2}}(t - (l-1)T - \frac{T}{2}) \cos(2\pi f^{(l)}[t - (l-1)T] + \theta_l), \tag{2.29}$$

where the signal amplitude $\underline{R}$ is Rician distributed:

$$f_{\underline{R}}(r) = \frac{r}{\sigma^2} e^{-\frac{A^2+r^2}{2\sigma^2}} I_0(\frac{Ar}{\sigma^2}). \tag{2.30}$$

Let γ_b denote the E_b/N_0 of the AWGN channel, and $\bar{\gamma}_b$ denote the average E_b/N_0 of the Rician fading channel. From chapter 2 of [16], the relationship between $\bar{\gamma}_b$ and γ_b is

$$p(\gamma_b) = \frac{(1+K)e^{-K}}{\bar{\gamma}_b} e^{-\frac{(1+K)\gamma_b}{\bar{\gamma}_b}} I_0\Big(\sqrt{4K(1+K)\frac{\gamma_b}{\bar{\gamma}_b}}\Big), \tag{2.31}$$

where K is the Rician K-factor defined as

$$K \triangleq \frac{A^2}{2\sigma^2}. \tag{2.32}$$

We have analyzed the performance in AWGN channels in Section 2.1.3 (continuous phase) and Section 2.1.4 (discontinuous phase), resulting in (2.15) and (2.26), respectively, for the symbol error rate. We now denote (2.15) by $\bar{Ps}^{cont}_{AWGN}$, and (2.26) by $\bar{Ps}^{disc}_{AWGN}$. The performance in a Rician fading channel with continuous and discontinuous phase are, respectively,

$$\bar{Ps}^{cont}_{Rice} = \int_0^\infty \bar{Ps}^{cont}_{AWGN} p(\gamma_b) d\gamma_b, \quad \bar{Ps}^{disc}_{Rice} = \int_0^\infty \bar{Ps}^{disc}_{AWGN} p(\gamma_b) d\gamma_b. \tag{2.33}$$

As is well known, the Rician fading channel is equivalent to the Rayleigh fading channel when $K = 0$, and is equivalent to an AWGN channel when $K = \infty$. We choose $K = 0, 10, \infty$ to illustrate the optimal performance curves, where we do the optimization by exhaustive search. The optimal parameter pairs (z, h) are summarized in Table 2.2, with precision 0.04 for both, and the optimal value is $r = 1$.

Table 2.2: Optimal parameter pairs (z,h) for different M and K

Continuous phase, optimal pair (z,h)				
K \ M	2	4	8	16
0	(0.4,0.8)	(0.44,0.88)	(0.44,0.96)	(0.44,1)
10	(0.48,0.8)	(0.52,0.92)	(0.48,0.96)	(0.48,1)
∞	(0.52,0.84)	(0.56,0.92)	(0.52,0.96)	(0.52,1)
discontinuous phase, optimal pair (z,h)				
K \ M	2	4	8	16
0	(0.56,1)	(0.52,1)	(0.48,1)	(0.44,1)
10	(0.64,1.04)	(0.56,1.04)	(0.52,1)	(0.48,1)
∞	(0.64,1.04)	(0.6,1.04)	(0.56,1.04)	(0.56,1)

The optimal MFSK demodulator performance is presented in Section 2.4. For $M = 2$ and 16, $K = 0, 10, \infty$, and continuous phase, the results are shown in Fig. 2.4 and Fig. 2.5, respectively. The optimal MFSK demodulator performance for $M = 2$ and 16, $K = 0, 10, \infty$, and discontinuous phase are shown in Fig. 2.7 and Fig. 2.8, respectively.

We summarize the performance of 2-pole BPF system with non-orthogonal signaling with continuous/discontinuous phase, and compare them with matched filter performance in Fig. 2.9 in Section 2.4. There is approximately a 1.2 dB gap between the matched filter and the 2-pole BPF system for the discontinuous phase case for all $M's$ and $K's$. The performance of the 2-pole BPF system for the continuous phase case is similar to matched filter performance when M is small, and approaches the discontinuous phase performance as M increases. This is because phase continuity is most beneficial when the previous symbol is the same as the current one,

which happens with a probability of $1/M$. In other words, phase continuity is less likely to help when M becomes larger, thus making the performance with continuous phase similar to that with discontinuous phase.

2.3 Demodulator Performance with Reed-Solomon Codes

The choice of RS codes with hard decision decoding here is particularly appropriate because of the lower complexity compared to, say, soft decision in general, and iterative decoding, in particular, and the straightforward manner in which the RS encoded codewords can be mapped to the MFSK signal set. The optimal RS codes for an optimal non-coherent MFSK receiver with hard-decision decoding in Rician channels are analyzed in [17]. We optimize for the suboptimal system the code dimension k in conjunction with the 3-tuple z,h,r for 16FSK with (n,k) RS codes, where the code length $n = 15$ or 255, i.e., one or two FSK symbols per RS symbol. We fixed the code length (at either 15 or 255) and exhaustively searched all possible values of code dimension, k, to find the k that minimizes the E_b/N_0 required at a BER of $P_b = 10^{-5}$. We will see that the optimal code dimension k is the same as those found in [17], when $n = 15$.

Application of this transmission scheme to a fading channel generally requires that coded data be interleaved after encoding in order to randomize symbol errors due to burst errors caused by deep fades, thus improving decoder performance [18]. Here we assume that perfect interleavers (i.e., infinitely long) are used. Let P_s be the MFSK symbol error rate, then the uncoded RS symbol error rate is

$$P_{RS,uncoded} = \begin{cases} P_s, & n = 15 \\ 1-(1-P_s)^2, & n = 255, \end{cases} \tag{2.34}$$

and the bit error rate for the coded system, from chapter 7 of [14], is given by

$$P_{RS,coded} = \frac{n+1}{2n} \cdot \frac{1}{n} \sum_{i=t+1}^{n} i \binom{n}{i} P_{RS,uncoded}^{i} (1 - P_{RS,uncoded})^{n-i}, \tag{2.35}$$

where

$$n = 15 \text{ or } 255, \quad k = 1, 3, \ldots, n-2, \quad t = \frac{n-k}{2}. \tag{2.36}$$

The optimal system parameters (time-bandwidth parameter (z) and code dimension (k)) are listed in Table 2.3. The other optimal parameters can be shown to be $h = \Delta f T = 1$ and $r = T_s/T = 1$ for all cases.

Table 2.3: Optimal Parameter Pairs (z, k) for different K and n

n	phase / K	continuous	discontinuous
15	0	(0.44,5)	(0.44,5)
	10	(0.44,9)	(0.48,9)
	∞	(0.48,11)	(0.48,11)
255	0	(0.44,117)	(0.44,117)
	10	(0.44,173)	(0.48,173)
	∞	(0.48,201)	(0.48,201)

Note that the (2.35) – (2.36) assume the modulator, the channel, and the demodulator form an equivalent discrete (M-ary) input, discrete (M-ary) output, symmetric memoryless channel. For the system with 2-pole BPFs, we do not retain symmetry because of the ICI and ISI. However, we can achieve an upper bound on the coded error rate by replacing P_s with the highest channel crossover probability among all the M possible transmitted symbols.

In general, the loss by using 2-pole BPFs (relative to matched filters) is consistent with or without coding. That performance degradation is no greater than 1.2 dB for $M = 16$. The optimal coded performance curves are shown in Figs. 2.10 – 2.13 in Section 2.4, where E_b is the average energy per information bit.

2.4 Numerical Results

In this section, we present the numerical results for the various systems. Figs. 2.4 and 2.5 show the performance analysis and simulation results with both ICI and ISI in AWGN, Rayleigh and Rician ($K = 10$) channels with continuous phase and nonorthogonal signaling for $M = 2$ and 16, respectively. Figure 2.6 shows the performance difference between orthogonal signaling and nonorthogonal signaling in an AWGN channel. Figs. 2.7 and 2.8 show the performance analysis and simulation results with both ICI and ISI in AWGN, Rayleigh and Rician ($K = 10$) channels with discontinuous phase and nonorthogonal signaling for $M = 2$ and 16, respectively. Fig. 2.9 shows the performance difference between continuous and discontinuous phase in AWGN, Rayleigh and Rician ($K = 10$) channels. Figs. 2.10 and 2.11 show the performance of RS ($n = 15$) coding in Rayleigh and Rician ($K = 10$) channels, respectively, for $M = 16$. Figs. 2.12 and 2.13 show the performance of RS ($n = 255$) coding in Rayleigh and Rician ($K = 10$) channels, respectively, for $M = 16$. Note that in Figs. 2.10 – 2.13, for both the coded and uncoded cases, the simulation curves for the continuous and discontinuous cases fall virtually on top of one another.

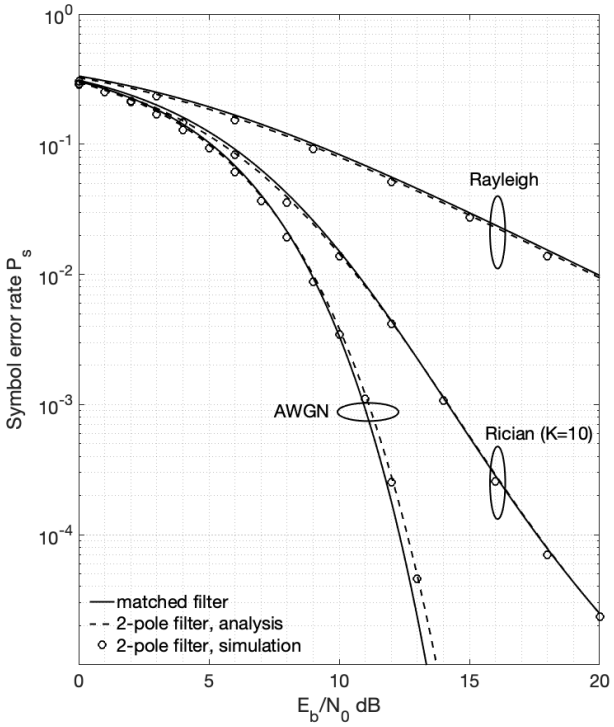

Figure 2.4: BFSK, continuous phase

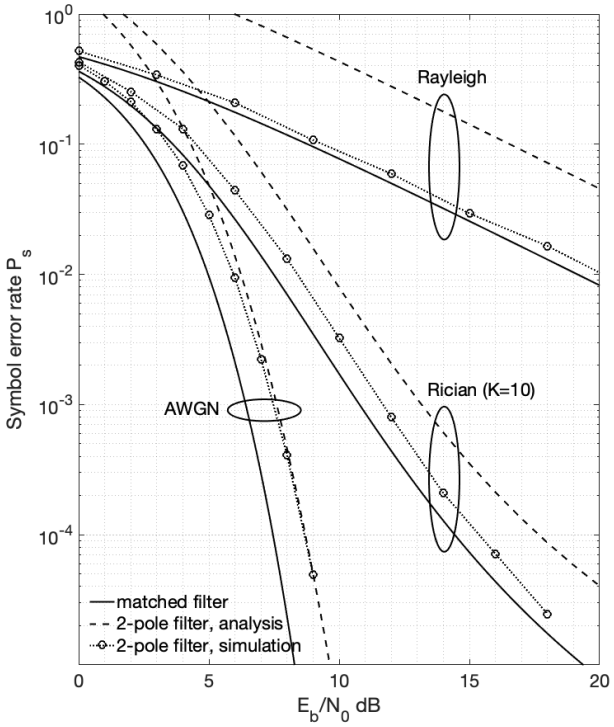

Figure 2.5: 16FSK, continuous phase

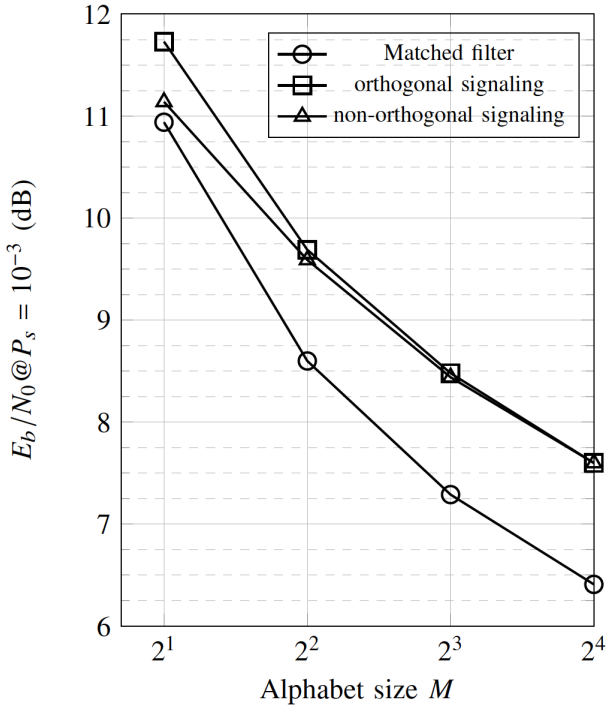

Figure 2.6: Orthogonal vs. nonorthogonal, AWGN

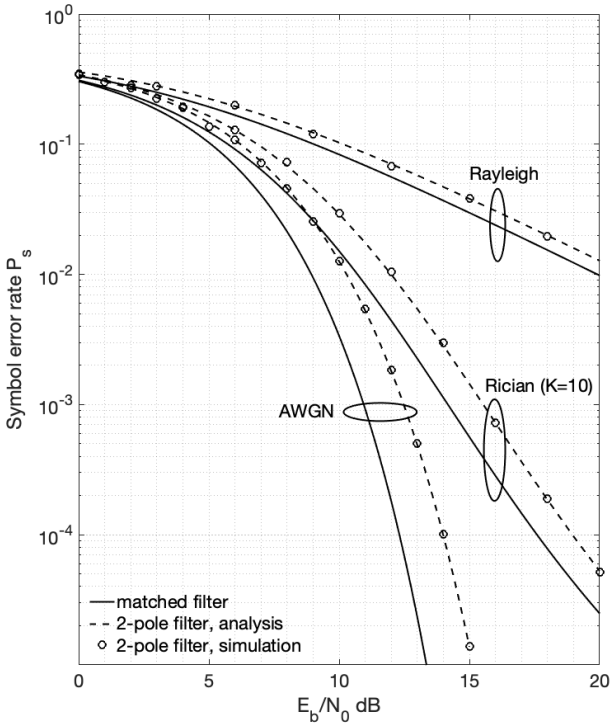

Figure 2.7: BFSK, discontinuous phase

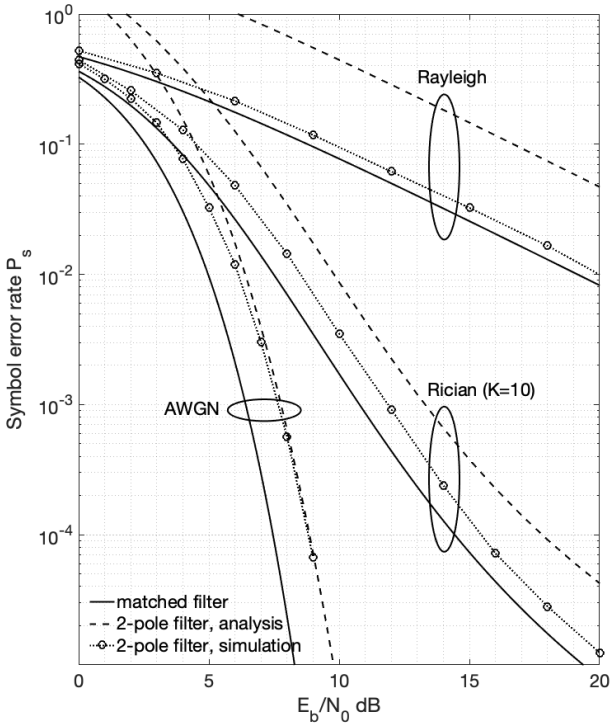

Figure 2.8: 16FSK, discontinuous phase

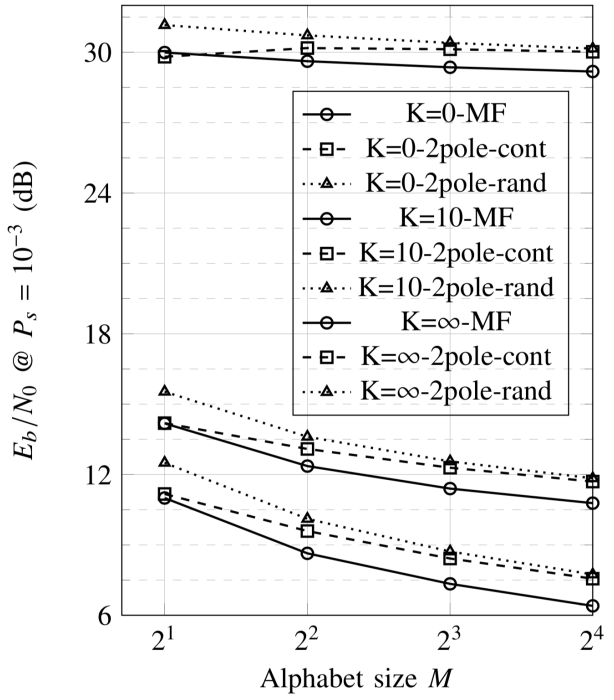

Figure 2.9: Continuous vs. discontinuous phase

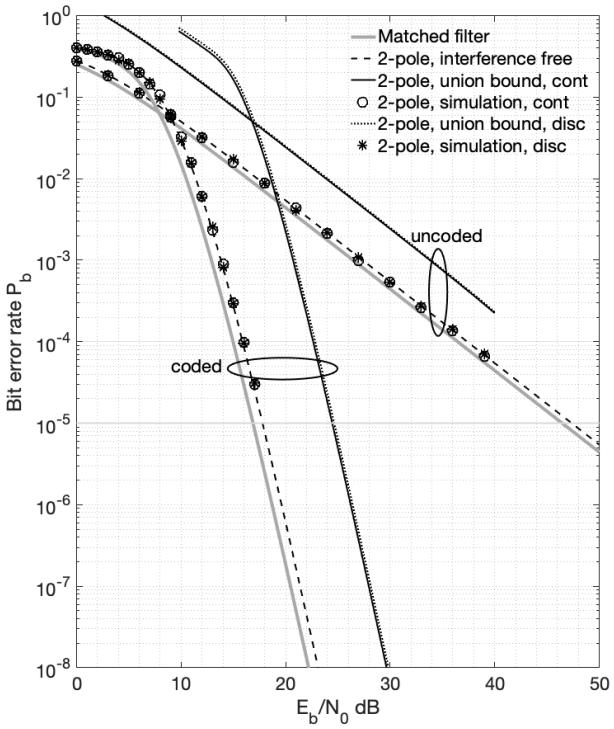

Figure 2.10: 16FSK-RS(15,5)-Rayleigh

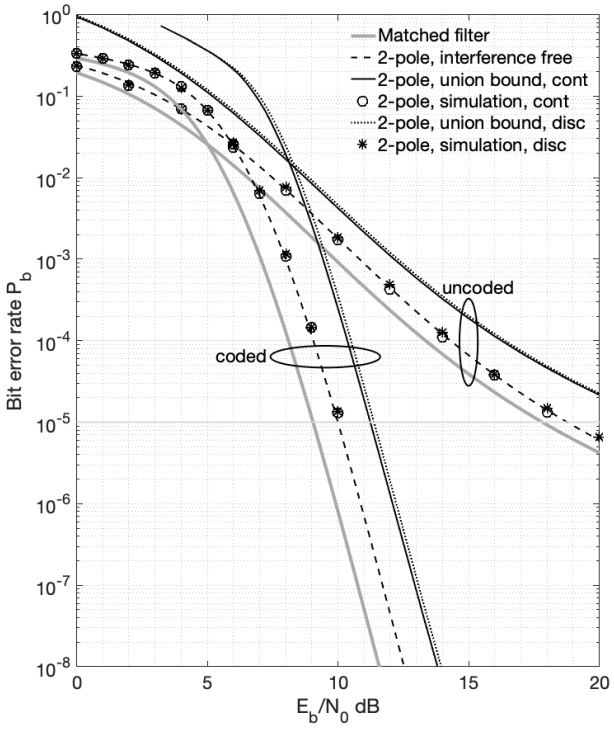

Figure 2.11: 16FSK-RS(15,9)-Rician

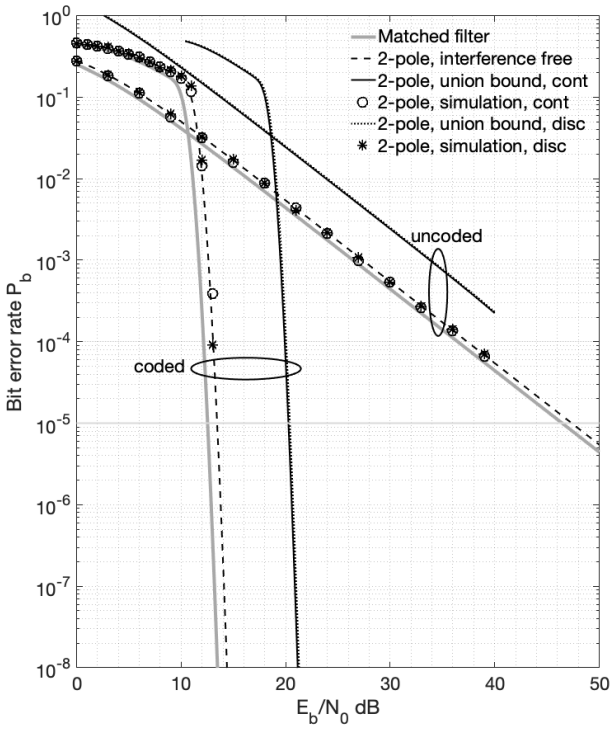

Figure 2.12: 16FSK-RS(255,117)-Rayleigh

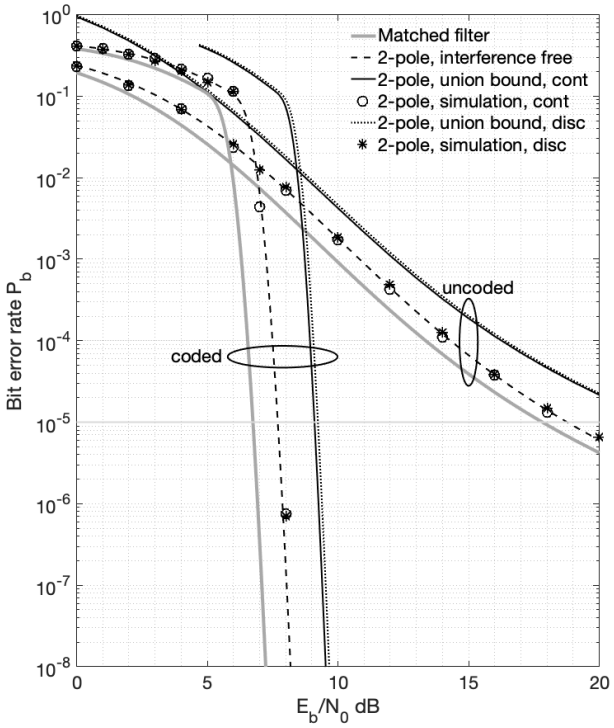

Figure 2.13: 16FSK-RS(255,173)-Rician

The text of this chapter is, in part, a reprint of the paper, Y. Xiang and L. B. Milstein, "Design and Performance Analysis for Short Range, Very Low-Power Communications," in *IEEE Transactions on Communications*, vol. 68, no. 9, pp. 5938-5950, Sept. 2020, doi: 10.1109/TCOMM.2020.3005454. The dissertation author is the primary researcher and author of the paper.

Chapter 3

On the use of FFH-MFSK for ultra-low power communications

3.1 Demodulator performance in full-band noise jamming

In this section, we analyze the performance of an FFH-MFSK non-coherent demodulator in full-band noise jamming. The analysis in this section serves as a basis so that we can easily generalize it to partial-band jamming in later sections. The transmitted signal is given by

$$\begin{aligned} s_0(t) = \sum_{m=1}^{\infty} & A_0 P_{\frac{T}{2}}\left(t-(m-1)T-\frac{T}{2}\right) \\ & \cos\left(2\pi f^{(m)}\left[t-(m-1)T\right]+\underline{\theta}_m\right), \end{aligned} \tag{3.1}$$

where A_0 is the amplitude of the transmitted signal, T is the symbol duration, so that the symbol energy is given by $E_s = A^2T/2$, bit energy is given by $E_b = E_s/\log_2 M$, and $P_a(x) \triangleq 1$ for $|x| \leqslant a$ and 0 elsewhere. Also, the random phase of the m^{th} symbol, $\underline{\theta}_m \sim U[0,2\pi]$, and $f^{(m)} \in \{f_1, f_2, \ldots, f_M\}$ is the frequency of the m^{th} symbol. The block diagram of an FFH-MFSK non-coherent demodulator is shown in Fig. 3.1 [14], [37] – [40], where the received dehopped

waveform, $\underline{r}(t)$, is given by

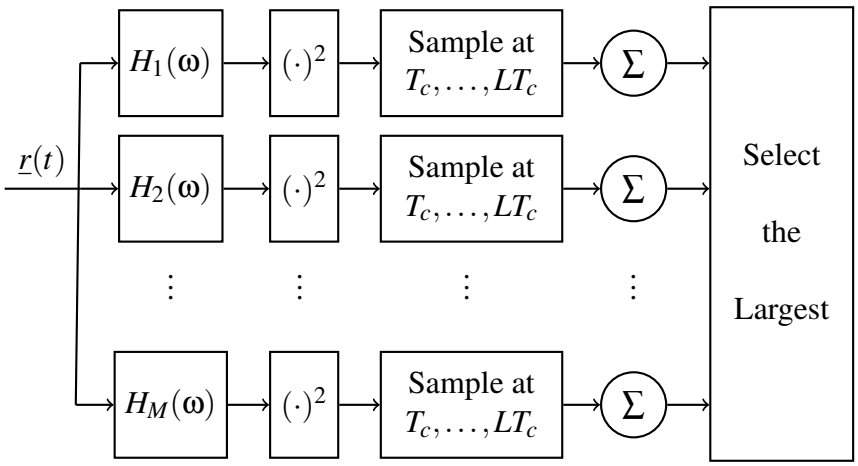

Figure 3.1: FFH-MFSK non-coherent demodulator structure

$$\underline{r}(t) = s(t) + \underline{n}_w(t) + \underline{n}_J(t). \tag{3.2}$$

In (3.2), $\underline{n}_J(t)$ and $\underline{n}_w(t)$ are additive Gaussian noise of the jammer and thermal noise, with single-sided power spectral density N_J and N_0, respectively, T_c is the hop duration, $L \geqslant 1$ is the number of hops/symbol, and $(\cdot)^2$ denotes square law detection. The dehopped FSK signal $s(t)$ is given by

$$s(t) = \sum_{l=1}^{\infty} A P_{\frac{T_c}{2}}\left(t - (l-1)T_c - \frac{T_c}{2}\right) \cdot \cos\left(2\pi f^{(l)}\left[t - (l-1)T_c\right] + \underline{\theta}_l\right), \tag{3.3}$$

where A is the amplitude of the received signal, $f^{(l)}$ is the frequency of the l^{th} hop, and the random phase of the l^{th} hop, $\underline{\theta}_l \sim U[0, 2\pi]$. Note that here the L hops of a symbol have the same frequency prior to hopping and after dehopping, i.e., $f^{(1)} = \cdots = f^{(L)}, f^{(L+1)} = \cdots = f^{(2L)}$ and so on, but they do not need to have the same frequency, as we will see later, when we use chip-interleaving. The filters are either matched filters or 2-pole BPFs. The transfer function and impulse response of the i^{th} 2-pole BPF are given by (2.4), where we set the tone spacing to be

$\Delta f \triangleq f_2 - f_1 = 1/T_c$, i.e., we use the minimum tone spacing that satisfies orthogonal signaling, since the optimal performance we found in [34] was almost always achieved with this tone spacing. We optimize the time-bandwidth parameter $z \triangleq WT_c$ to minimize the E_b/N_J required to achieve a predetermined BER for the 2-pole BPF system, and we compare the results to the corresponding matched filter system.

Lastly, we will ignore thermal noise in most of the following analysis, which is consistent with the typically dominant jamming power, as is done in references such as [14], [41], [42]. However, we will come back to show how insignificant the thermal noise is when we consider PBJ in Section 3.2.

3.1.1 Matched filter detection

The symbol error rate (SER) of an FFH-MFSK-MF system in full-band noise jamming, $P_{s,MF}$, is given in [14]. The numerical results for $M = 16$ and $L = 2$ are presented in [43]. In a slow, flat, Rician fading channel, the symbol amplitude $\underline{R}$ is Rician distributed, as shown in (2.30). If we let γ denote the instantaneous E_s/N_J, and $\bar{\gamma}$ denote the average $\bar{E}_s/N_J$ with Rician fading, the pdf of γ is given by (2.31).

Then, the FFH-MFSK-MF system performance in full-band noise jamming and slow, flat, Rician fading is given by Equation (5) of [43]. Numerical results for $M = 16$ and $L = 2$ with both no fading and Rician ($K = 10$) fading, are presented Section IV of [43].

3.1.2 Two-pole BPF detection

One problem with 2-pole BPF detection is that there exists both inter-carrier interference (ICI) and inter-symbol interference (ISI), where ISI primarily comes from the previous pulse [34]. Let Ps_{in}^{m} denote the probability that the current symbol is at frequency f_i but is detected as $f_n, n \neq i$, and where the previous symbol is at frequency f_m. With square-law combining of the

output signals from the corresponding 2-pole BPFs for the L hops, the output of either branch i or branch n is the sum of $2L$ correlated non-central chi-square random variables (rv). We employ the union bound and thus do pairwise comparison. The test statistic is a linear combination of $4L$ correlated non-central chi-square rv's, i.e., we are interested in the quadratic form

$$Q(X) = \sum_{i=1}^{2L} X_i^2 - \sum_{j=2L+1}^{4L} X_j^2 \triangleq X^T A X, \tag{3.4}$$

where X, defined in Appendix C, has a multi-normal distribution with mean vector $\mu = E[X]$ and covariance matrix $\Sigma = Cov(X)$. The weighting matrix A is given by

$$A = \begin{bmatrix} I_{2L} & 0_{2L} \\ 0_{2L} & -I_{2L} \end{bmatrix}, \tag{3.5}$$

where I_{2L} and 0_{2L} denote the $2L \times 2L$ identity matrix and zero matrix, respectively. Detailed analysis on computing μ and Σ can be found in Appendix C. It turns out that, as shown in [44], $Q(X)$ can be represented as a linear combination of $4L$ independent non-central chi-square rv's:

$$Q(X) = X^T A X = \sum_{i=1}^{4L} \lambda_i (U_i + b_i)^2, \tag{3.6}$$

where $\lambda_1, \ldots, \lambda_{4L}$ are eigenvalues of $\Sigma^{\frac{1}{2}} A \Sigma^{\frac{1}{2}}$, the $U_i's$ are i.i.d. standard normal random variables and $b = [b_1, \ldots, b_{4L}]^T = P^T \Sigma^{-\frac{1}{2}} \mu$, where P is a $4L \times 4L$ orthogonal matrix that diagonalizes $\Sigma^{\frac{1}{2}} A \Sigma^{\frac{1}{2}}$, i.e.,

$$P^T \Sigma^{\frac{1}{2}} A \Sigma^{\frac{1}{2}} P = diag(\lambda_1, \ldots, \lambda_{4L}), \quad PP^T = I. \tag{3.7}$$

Then the characteristic function of the random variable $Q(X)$ can be found as the product of the individual characteristic functions, and $Ps_{in}^m = Prob(Q(X) < 0)$ can be evaluated numerically.

The union bound on the average symbol error rate is, by symmetry,

$$\bar{P}_{s,2pole} = \frac{2}{M^2} \sum_{i=1}^{M/2} \sum_{n=1,n\neq i}^{M} \sum_{m=1}^{M} Ps_{in}^{m}. \tag{3.8}$$

In a Rician fading channel, the union bound on performance is given by

$$\bar{P}_{s,2pole-Rice} = \int_0^\infty \bar{P}_{s,2pole} \cdot f(\gamma) d\gamma, \tag{3.9}$$

where $f(\gamma)$ was defined in (2.31).

The optimal time-bandwidth parameter, z, and the corresponding performance of our ad-hoc receiver in comparison with the matched filter system performance for various 2-pole BPF systems are listed in Table I of [43], and the numerical results for $M = 16$ and $L = 2$ with both no fading and Rician ($K = 10$) fading are presented in Section IV of [43].

3.1.3 Demodulator performance with diversity and/or RS coding

Diversity can be achieved by interleaving the hops and thus improving the performance in a slow, flat, Rician fading channel. Detailed discussion including the optimal parameters and performance can be found in Section II of [43] and detailed analysis is shown in Appendix D. Alternatively, we can use FEC to improve performance. Detailed analysis including the optimal parameters and performance can be found in Section II of [43].

3.2 Demodulator performance in partial-band noise jamming

The previous section focused on full-band noise jamming, where the jammer jams the entire spectrum. In reality, the jammer may jam a fraction of the spectrum to degrade system performance. In this section, we consider an FFH-MFSK system using either matched filter or 2-pole BPF detection under PBJ. To be specific, for the matched filter system, we find the

worst-case performance, and for the 2-pole BPF system, we find the NE at a given BER.

Suppose the partial-band interference is a zero-mean Gaussian random process with a flat power spectral density over a fraction ρ of the total spread spectrum bandwidth, W_{ss}, and zero elsewhere. Furthermore, as is common in the literature, we assume that on a given hop, each M-ary band lies either entirely inside or entirely outside W_J [41]. In the region or regions where the power spectral density is nonzero, its value is N_J/ρ.

As in previous sections, we will ignore thermal noise. To justify this, we compare the performance with and without thermal noise when $M = 2$ and $L = 1$ with matched filter detection both in a non-fading channel and in a Rician fading channel. Let $a \triangleq N_J/N_0$, and since jamming is usually dominant over thermal noise, we assume $a > 1$ (typically $a \gg 1$). We denote $\gamma \triangleq E_b/N_J$ (so that $E_b/N_0 = a\gamma$) for an AWGN channel and $\bar{\gamma} \triangleq \bar{E}_b/N_J$ for a Rician fading channel, where $\bar{E}_b$ is the average (over the fade) received energy per bit.

Let $f(x) = \frac{1}{2}e^{-\frac{x}{2}}$ and $g(x) = \frac{K+1}{2(K+1)+x}e^{\frac{-Kx}{2(K+1)+x}}$ [45], so that the approximate BER, obtained by ignoring thermal noise, is given by $P_{b1} = \rho \cdot f(\rho\gamma)$ for the non-fading channel, and $P_{b1} = \rho \cdot g(\rho\bar{\gamma})$ for the Rician fading channel. Since $E_b/N_J = \gamma, N_J/N_0 = a$, we have $\frac{E_b}{\frac{N_J}{\rho}+N_0} = \frac{1}{\frac{1}{\rho E_b/N_J}+\frac{1}{E_b/N_0}} = \frac{\gamma}{\frac{1}{\rho}+\frac{1}{a}}$. Thus, the BER with jamming and noise is given by

$$\begin{aligned} P_b &= \rho \cdot f\left(\frac{E_b}{\frac{N_J}{\rho}+N_0}\right) + (1-\rho)\cdot f\left(\frac{E_b}{N_0}\right) \\ &= \rho \cdot f\left(\frac{\gamma}{\frac{1}{\rho}+\frac{1}{a}}\right) + (1-\rho)\cdot f\left(a\gamma\right), \end{aligned} \tag{3.10}$$

for a non-fading channel, and for a Rician fading channel,

$$P_b = \rho \cdot g\left(\frac{\bar{\gamma}}{\frac{1}{\rho}+\frac{1}{a}}\right) + (1-\rho)\cdot g\left(a\bar{\gamma}\right). \tag{3.11}$$

The exact BER and approximate BER, P_b and P_{b1} with different $\rho's$ in non-fading and

Rician ($K = 10$) fading channels are shown in Figs. 3.2 and 3.3, respectively, where $a = 5$ is used. The noise-free approximation is valid as long as E_b/N_J is reasonably large, and the approximation is better for smaller ρ. As we will see later, both conditions are satisfied in this paper. As a result, we will continue ignoring thermal noise, and the consequence of which will be error-free detection with a probability of $1 - \rho$.

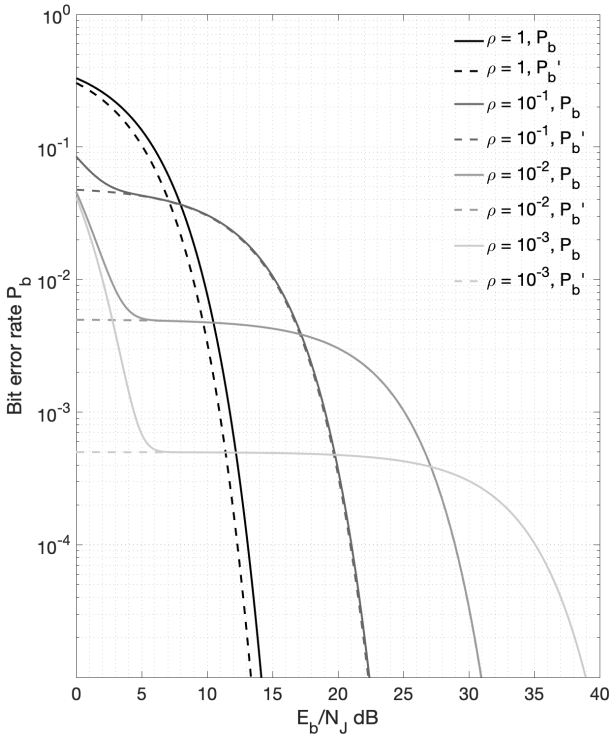

Figure 3.2: $M = 2, L = 1, K = \infty$

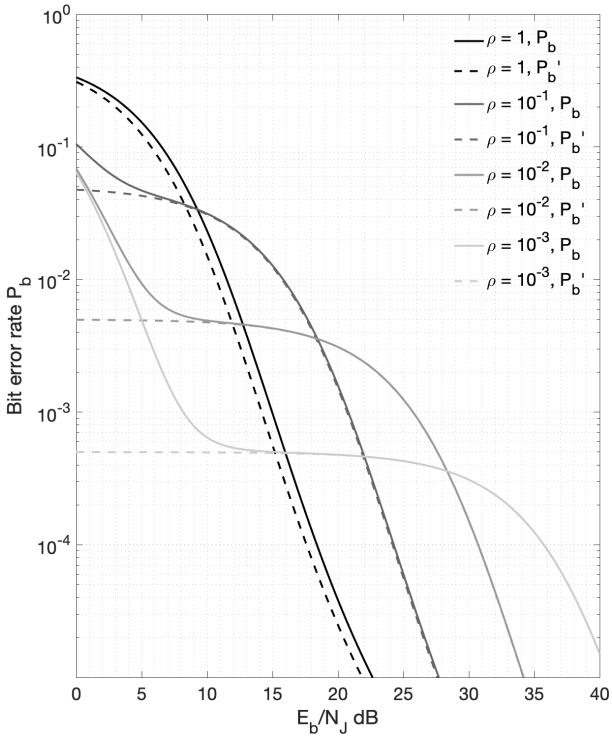

Figure 3.3: $M = 2, L = 1, K = 10$

Detailed discussion of the FFH-MFSK system with MF/2-pole BPF detection under PBJ can be found in [43] and detailed analysis on finding the worst-case performance of the FFH-MFSK-MF system both in a non-fading channel and in a Rician fading channel is shown in Appendix E.

3.3 Demodulator performance in multi-tone jamming

A second, sometimes more effective, class of intelligent FH jamming than PBJ is MTJ. In this category, the jammer divides its total received power into a number of distinct, equal power, random phase continuous wave (CW) tones, and distributes them over the spread spectrum bandwidth according to some strategies, as will be discussed shortly. Because CW tones are the most efficient way for a jammer to inject energy into the non-coherent detectors, MTJ is particularly effective against a FH/MFSK system. Unlike PBJ, where the performance improves with the alphabet size M, the performance in MTJ degrades with M. In this section, we analyze the performance of an FFH-MFSK non-coherent system under MTJ, both with MF detection and with 2-pole BPF detection, in a non-fading or slow, flat, Rician fading channel. To be specific, for the matched filter system, we find the worst-case partial-band jamming performance, and for the 2-pole BPF system, we find the NE at a given BER.

Some simplifying assumptions that allow us to focus on the issues of interest are [41]

- Thermal noise is dominated by jamming interference and thus negligible.
- Each jamming tone coincides exactly in frequency with one of the N_t available FH slots (no frequency offset).
- Changes of location of slots that are jammed coincides with hop transitions.

While these assumptions can never be achieved in practice, they simplify the analysis and yield somewhat pessimistic performance results.

There are two MTJ strategies: independent MTJ, where the jammer distributes the tones pseudorandomly over all slots, and band MTJ, where the jammer places $n \in [1, M]$ tones in each jammed M-ary band. Independent MTJ and $n = 1$ band MTJ are shown to result in the same performance when E_b/η_J is large, and $n = 1$ band MTJ is shown to result in more performance degradation than $n > 1$ MTJ. Therefore, we will focus on $n = 1$ MTJ in this paper.

In this section, we analyze the performance of an FFH-MFSK system under MTJ in a non-fading or slow, flat, Rician fading channel, with MF and 2-pole BPF detection. Specifically, for MF detection, we find the worst-case parameter and performance, and for 2-pole BPF detection, we find the parameter and performance at NE, and we compare the performances with different channel conditions and filters. The entire analysis is based on the assumption that E_b/η_J is large.

3.3.1 Matched filter detection

The asymptotic BER of an FFH-MFSK system with MF detection as $E_b/\eta_J \to \infty$ can be shown to be the same as that of a SFH system,

$$P_b = \frac{\alpha LM}{2\log_2 M \cdot \frac{E_b}{\eta_J}}, \tag{3.12}$$

where detailed analysis is provided in Appendix F.1. In (3.12), α is the SJR to be optimized by the jammer and the worst-case performance is found by optimizing α as

$$P_{b,wc} = \begin{cases} \frac{1}{2}, & \frac{E_b}{\eta_J} \leqslant \frac{M}{\log_2 M}, \\ \frac{M}{2\log_2 M} \cdot \frac{1}{E_b/\eta_J}, & \frac{E_b}{\eta_J} \geqslant \frac{M}{\log_2 M}, \end{cases} \tag{3.13}$$

with the worst-case parameter α be

$$\alpha_{wc} = \begin{cases} \frac{\log_2 M}{M} \cdot \frac{E_b}{\eta_J}, & \frac{E_b}{\eta_J} < \frac{M}{\log_2 M}, \\ 1_-, & \frac{E_b}{\eta_J} \geqslant \frac{M}{\log_2 M}. \end{cases} \tag{3.14}$$

In a Rician fading channel, we assume that the system and the jammer experience independent fades, with a Rician K-factor K_s for the signal, and K_j for the jammer. Then the performance is given as a function of $c \triangleq \alpha_r L$ (α_r is the average SJR), to be optimized by the jammer:

$$\begin{aligned} P_b(c) &= \frac{cM}{2\log_2 M \times \frac{E_b}{\eta_J}} \int_0^\infty \int_{x\sqrt{c}}^\infty h(x,K_s)h(y,K_j)dydx \\ &\triangleq \frac{G(c)}{E_b/\eta_J}, \end{aligned} \tag{3.15}$$

where

$$h(r,K) = 2(K+1)re^{-K-(K+1)r^2} I_0\left(2\sqrt{K(K+1)}r\right). \tag{3.16}$$

Detailed analysis is shown in Appendix F.2. The worst-case performance is found by differentiating P_b with c and setting to zero:

$$P_{b,wc} = P_b(c^*), \quad \text{where } P_b'(c^*) = 0. \tag{3.17}$$

The optimum value of c, denoted by c^*, along with the worst-case performance, characterized by $G(c^*)$, for $K_s, K_j \in \{0, 10, 10^4\}$ is shown in Table 3.1. Note that we have a sanity check that when $K_s, K_j \to \infty, c^* = G(c^*) = 1 - \varepsilon$ (the numbers are slightly off because K_s and K_j are not large enough). The $K_s = 0$ scenario is slightly different, as shown in Appendix F.3.

Table 3.1: Values of c^* and $G(c^*)$.

	$G(c^*)$			c^*		
K_s \ K_j	0	10	10^4	0	10	10^4
0	1			$E_b/\eta_J \cdot \log_2 M/M$		
10	0.4047	0.5145	0.5909	1.222	0.829	0.758
10^4	0.3679	0.5261	0.9454	1.000	0.745	0.952

3.3.2 Two-pole BPF detection

In a non-fading channel with 2-pole BPF detection, the average SER is given by

$$P_s = \frac{1}{L}P_1 + \frac{L-1}{L}P_2 \triangleq \frac{h(z,\alpha_2)}{E_b/\eta_J}, \tag{3.18}$$

where P_1 denotes the conditional SER when the jammed hop is the last one, P_2 denotes the conditional SER when the jammed hop is not the last one, and $\alpha_2 = \frac{r_s^2}{r_j^2}$ denotes the SJR, where r_s and r_j are the amplitudes of the signal and jamming waveforms, respectively. Detailed analysis can be found in Appendix J.

Note that the SER is a function of the system's parameter, z (time-bandwidth parameter), and the jammer's parameter α_2. From (3.18), in order to improve the performance, the system optimizes z to minimize $h(z,\alpha_2)$ (but subject to $z \geqslant 0.24$ for $M = 2$ or $z \geqslant 0.2$ for $M = 16$ to keep the eye open), and in order to degrade the performance the jammer optimizes α_2 to maximize $h(z,\alpha_2)$. The two players iteratively optimizes their strategies until a NE is reached. The numerical results for $L = 2$ hops/symbol are summarized in Table 3.2.

Table 3.2: Parameters and E_b/η_J at $P_b = 10^{-3}$ at NE.

M	z^*	α_2^*	$h(z^*, \alpha_2^*)$	2-pole performance	MF
2	0.24	0.34	0.582	27.6 dB	30.0 dB
16	0.2	0.38	2.263	30.8 dB	33.0 dB

We see that the 2-pole BPF detection results in better performance compared to MF detection, for both $M = 2$ and $M = 16$. This is because ISI is helping the system. With MF detection, there is no ISI, so the jammer only needs to win by ε in terms of power for each tone it jams, while with 2-pole BPF detection, since there is ISI, the jammer needs to put more power in each tone it jams in order to make sure jamming is effective. Therefore, with fixed jamming power, the jammer can jam fewer tones and the performance is better. Moreover, $M = 16$ results in a performance that is roughly 3 dB worse than that for $M = 2$, and this is consistent between MF and 2-pole BPF detection.

With Rician fading, the changes are that the amplitudes of the signal and jamming waveforms, r_s and r_j, are now random variables. The pdf of r_s is given by

$$f(r_s) = \frac{2(K_s+1)r_s}{\Omega_s} e^{-K_s - \frac{(K_s+1)r_s^2}{\Omega_s}} I_0\left(2\sqrt{\frac{K_s(K_s+1)}{\Omega_s}} r_s\right), \tag{3.19}$$

and for the pdf of r_j, we simply replace K_s by K_j in (3.19). The SJR is now defined as the ratio between the total power of the signal and jamming waveform: $\alpha_{r2} = \frac{\Omega_s}{\Omega_j}$. The performance with 2-pole BPF detection is found by integrating out the Rician amplitudes as

$$P_s^r = \frac{1}{L} P_1^r + \frac{L-1}{L} P_2^r \triangleq \frac{h_r(z, \alpha_{r2})}{E_b/\eta_J}, \tag{3.20}$$

where for $i = 1, 2$,

$$P_i^r = \frac{1}{E_b/\eta_J} \cdot \frac{\alpha_{r2} L}{(2\pi)^{L+1} M^2 \log_2 M} \sum_{i=1}^{M} \sum_{n=1, n\neq i}^{M} \sum_{m=1}^{M} \int_0^{2\pi} \cdots \int_0^{2\pi} \int_0^{2\pi} \int_0^{\infty} \int_0^{\infty} \left[1 - u(\mu_i^T A \mu_i)\right] f_{R_s}(r_s) f_{R_j}(r_j) dr_s dr_j d\theta_1 \ldots d\theta_L d\theta_J. \tag{3.21}$$

It can be shown that P_s^r is independent of Ω_s and Ω_j, using the same method described in Appendix F.2. Then, similar to the non-fading case, the system optimizes z to minimize $h_r(z, \alpha_{r2})$ and the jammer optimizes α_{r2} to maximize it. The two players iteratively optimize their strategies until an NE is reached. Different from the non-fading case, now the NE is achieved when $z \to \infty$, and α_{r2} and the corresponding performance are the same as the MF case, since ISI is diminishing for large z. However, we notice that when $z \geqslant 0.6, h_r(z, \alpha_{r2})$ is almost independent of z since ISI is small, and thus we will use $z = 0.6$ to generate the numerical results. The numerical results for $L = 2$ hops/symbol and $K_s = K_j = 10$ are summarized in the table below.

Table 3.3: Parameters and E_b/η_J at $P_b = 10^{-3}$ at NE.

M	z^*	α_2^*	$h(z^*, \alpha_2^*)$	2-pole performance	MF
2	0.6	0.4145	0.515	27.1 dB	27.1 dB
16	0.6	0.4145	1.935	30.1 dB	30.1 dB

We can use FEC to improve performance under MTJ. The idea is the same – we want to find the NE, but now the system has two parameter, the time-bandwidth parameter z and the code dimension k (suppose we fix the code length n), and thus the optimization is more time-consuming. The uncoded and (15,5) RS coded performances under MTJ in a non-fading or Rician ($K_s = K_j = 10$) fading channel are presented in Fig. 3.8 in Section 3.4.

3.4 Numerical results

In this section, we present the numerical results of previous sections. In all the figures of this section, $M = 16, L = 2$ and (15,5) RS code is used, where applicable. Figure 3.4 shows the performance analysis and the simulation results for both matched filter and 2-pole BPF detection for both non-fading and Rayleigh fading channels, with and without diversity, under full-band noise jamming. Figs. 3.5 and 3.6 show the performance where RS coding is used in a Rayleigh fading channel, with and without diversity, under full-band noise jamming, respectively. Fig. 3.7 shows the performance comparison for $K = 0, 10, \infty$, with and without coding, with and without diversity, under full-band noise jamming. Fig. 3.8 shows the results under MTJ in either a non-fading channel or a Rician ($K_s = K_j = 10$) fading channel, with and without coding. Fig. 3.9 shows the performance comparison of a FFH-16FSK system with MF or 2-pole BPF detection under PBJ or MTJ, in a non-fading or Rician ($K = 10$) fading channel. The 2-pole BPF system performs worse than the MF system by about 1 dB under PBJ, but is no worse than the MF system under MTJ.

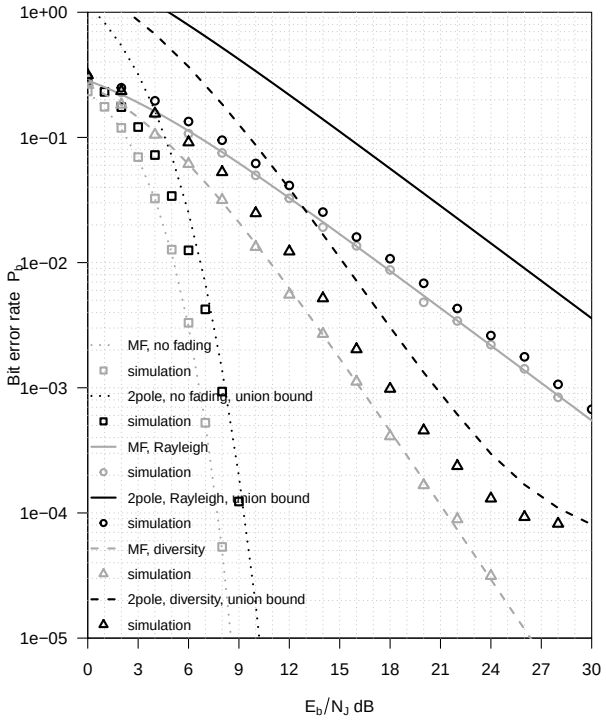

Figure 3.4: Rayleigh, uncoded, w/ & w/o diversity

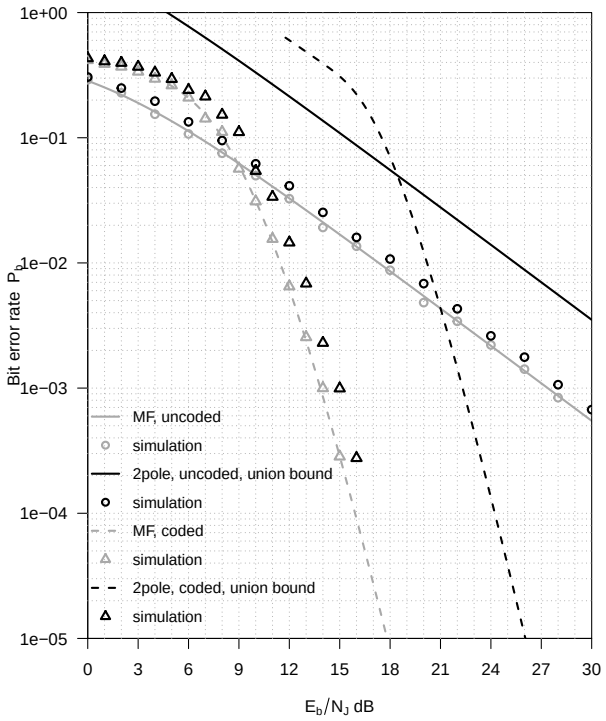

Figure 3.5: Rayleigh, no diversity, un/coded

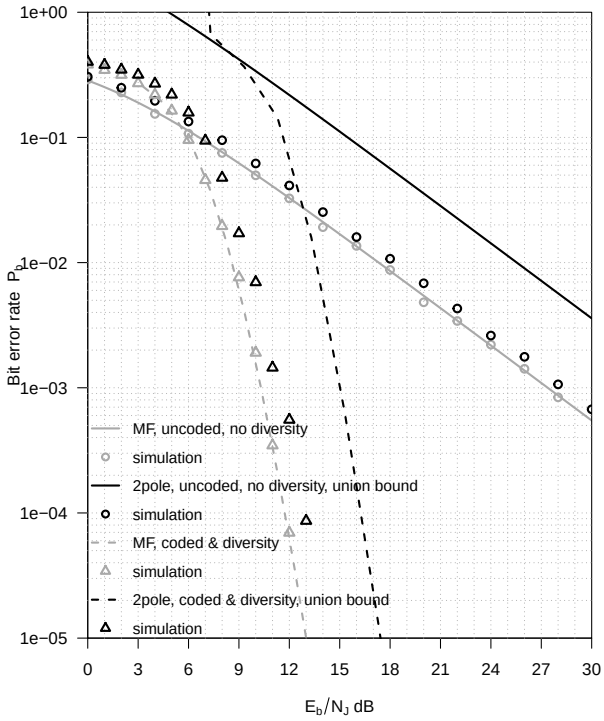

Figure 3.6: Rayleigh, coded with diversity

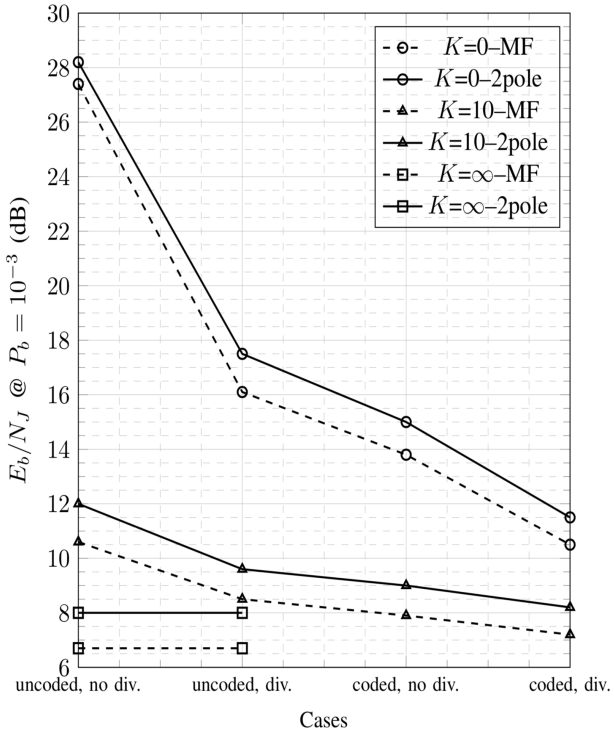

Figure 3.7: Performance comparison under FBJ

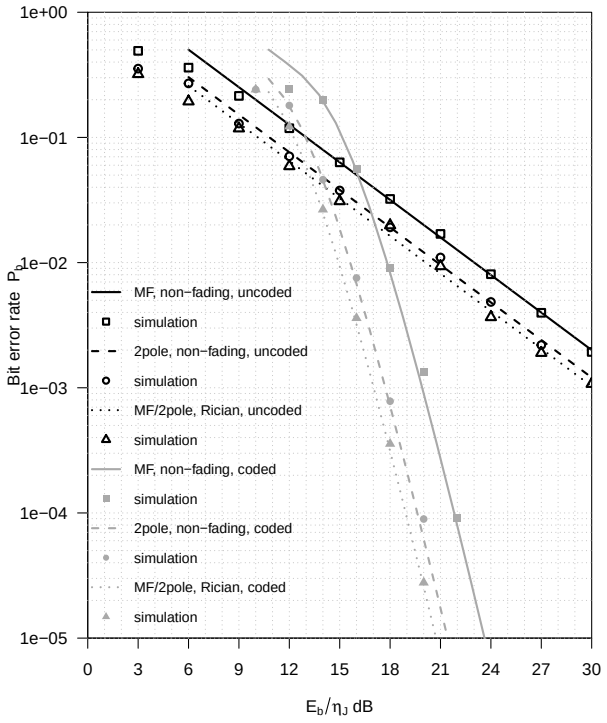

Figure 3.8: Performance under MTJ

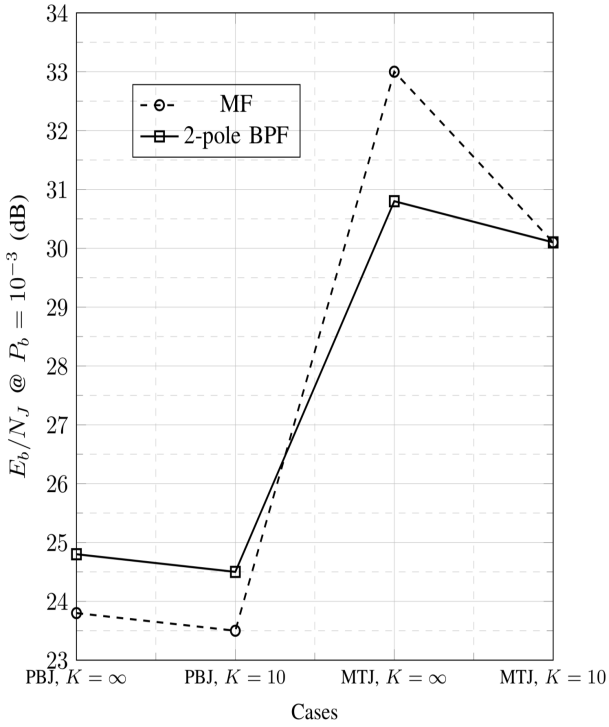

Figure 3.9: Performance comparison

The text of this chapter is, in part, a reprint of the papers, Y. Xiang and L. B. Milstein, "Design of an ultra-low power MFSK system in the presence of jamming," MILCOM 2021 - 2021 IEEE Military Communications Conference (MILCOM), 2021, pp. 652-657, doi: 10.1109/MILCOM52596.2021.9653041, and "On the use of FFH-MFSK for ultra-low power communications", submitted to *IEEE Transactions on Vehicular Technology*. The dissertation author is the primary researcher and author of these papers.

Chapter 4

Performance analysis for an ultra-low power GFSK system

4.1 Demodulator performance in an AWGN channel

In this section, we analyze the performance of a GFSK non-coherent demodulator with 2-pole BPF detection in an AWGN channel. The demodulator consists of a parallel bank of M branches, each with a BPF whose center frequency is the frequency of the corresponding tone, followed by an envelope detector and a sampler that takes a sample at time $t = T_s$. We choose the largest among the M test statistics from the samplers to make a decision, as shown in Fig. 4.1, where the received waveform is given by

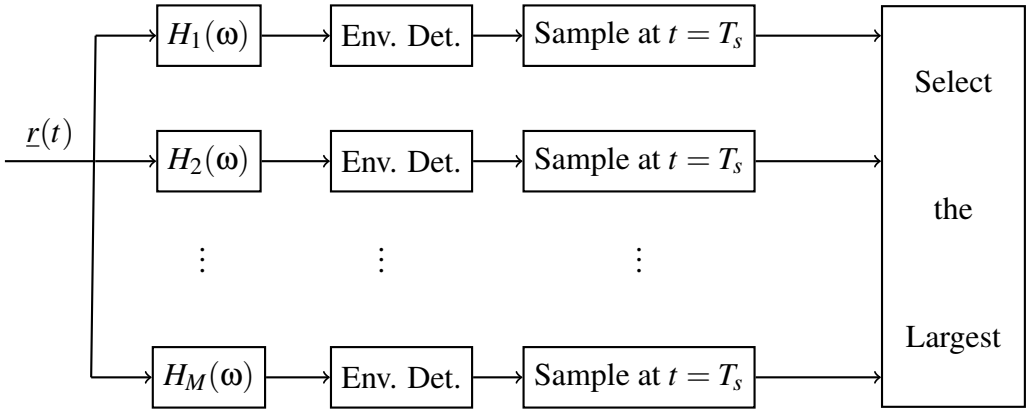

Figure 4.1: Receiver structure

$$\underline{r}(t) = s(t) + \underline{n}_w(t). \tag{4.1}$$

In (4.1), $\underline{n}_w(t)$ is additive white Gaussian noise (AWGN) with singled sided power spectral density η_0, and $s(t)$ is a pulse train of rectangular pulses of duration T, filtered by Gaussian filters. The lowpass equivalent signal of one pulse in $s(t)$ is given by

$$s_{lp}(t) = P_{\frac{T}{2}}(t - \frac{T}{2}) * g_{lp}(t), \tag{4.2}$$

where $P_a(x)$ is a rectangular pulse defined in (2.2) and the transfer function and impulse response of the lowpass equivalent Gaussian filter are,

$$\begin{aligned} G_{lp}(f) &= e^{-2\pi^2\delta^2 f^2}, \\ g_{lp}(t) &= \frac{e^{-\frac{t^2}{2\delta^2}}}{\sqrt{2\pi}\cdot\delta}, \end{aligned} \tag{4.3}$$

respectively. The detection filters $H(\omega)$ are 2-pole BPFs, and the transfer function and impulse response of the i^{th} filter were defined in (2.4). The impulse response of the lowpass equivalent

filter of the 2-pole BPF is given by

$$h_{lp}(t) = \pi W e^{-\pi W t} u(t). \tag{4.4}$$

We define

$$\begin{cases} z_g = \frac{\sqrt{\ln 2}}{2\pi\delta} T, \\ z = WT, \\ h = \Delta f T, \\ r = T_s/T, \end{cases} \tag{4.5}$$

where W is the bandwidth of the 2-pole BPF, Δf is the tone spacing, z_g is the time-bandwidth product of the lowpass equivalent Gaussian filter, z is the time-bandwidth product of the lowpass equivalent filter of the 2-pole BPF, h is the modulation index, T_s is the sampling time and r is the normalized sampling time. Note that all the parameters in (4.5) are dimensionless, meaning our results are independent of the symbol duration (or data rate). For each pair of (z_g, h), we optimize z, r to minimize the E_b/η_0 required at a bit error rate (BER) of 10^{-3}.

The total system bandwidth of an M-ary FSK system is given by

$$B = (M-1) \times \Delta f + B_{sig}, \tag{4.6}$$

where B_{sig} is the bandwidth of one FSK signal. While there are multiple ways of defining bandwidth of a signal, such as the null-to-null bandwidth and equivalent noise bandwidth (ENBW), all with their own advantages and disadvantages, B_{sig} is roughly on the same order as the tone spacing Δf. Therefore, for a large M (e.g., for our baseline design of $M = 16$), $B \approx M\Delta f$. Since $h = \Delta f T = 1$ was shown in [34] – [43] to yield optimal performance, the bandwidth saved by the system proposed in this paper can be represented as $1 - h$ compared to them.

It is easy to see that our system experiences both ICI and ISI due to Gaussian filtering, non-orthogonal tone spacing and 2-pole BPF detection. Therefore, we need to account for both types of interference when doing performance analysis. Because of the non-causality of the Gaussian filter, to detect the current transmitted symbol, we need to consider ISI from both the previous symbols and the future symbols. Based on the analysis in [34], the adjacent symbols contribute the most ISI, so we consider only one previous symbol and one future symbol as the source of ISI in this paper. If the transmitted symbol has frequency f_i, the ICI branch is the branch with 2-pole BPF centered at f_n, the previous symbol has frequency f_{m_1} and the future symbol has frequency f_{m_2}, then the union bound on the symbol error rate (SER) is given by

$$\bar{P}_s = \frac{1}{M^3}\frac{1}{(2\pi)^2}\sum_{i=1}^{M}\sum_{n=1,n\neq i}^{M}\sum_{m_1=1}^{M}\sum_{m_2=1}^{M}\int_0^{2\pi}\int_0^{2\pi} Ps_{in}^{m_1 m_2}\, d\theta_1 d\theta_2, \tag{4.7}$$

where $\theta_1, \theta_2 \sim U[0, 2\pi]$ and $Ps_{in}^{m_1 m_2}$ is the conditional SER, conditioned on θ_1 and θ_2, and is given by [15]

$$Ps_{in}^{m_1 m_2} = \frac{1}{2}\left[1 - Q(\sqrt{b}, \sqrt{a}) + Q(\sqrt{a}, \sqrt{b})\right], \tag{4.8}$$

with

$$\begin{Bmatrix} a \\ b \end{Bmatrix} = \frac{1}{2\sigma^2}\left[\frac{\frac{A_1^2+A_2^2}{2} - 2|\rho|\sqrt{\frac{A_1^2}{2}\frac{A_2^2}{2}}\cos(\theta_1 - \theta_2 + \phi)}{1-|\rho|^2} \mp \frac{\frac{A_1^2}{2} - \frac{A_2^2}{2}}{\sqrt{1-|\rho|^2}}\right], \tag{4.9}$$

where $Q(\cdot,\cdot)$ is the Marcum-Q function defined in (2.19) and $I_0(\cdot)$ is the modified Bessel function of the first kind and zeroth order, defined in (2.20). The parameters in (4.9) can be shown to be

given by

$$\begin{aligned}
A_2^2 &= I_2^2 + Q_2^2, \\
\theta_2 &= \tan^{-1}\left[\frac{-I_2 \sin\left(2\pi(i-n)hr\right) + Q_2 \cos\left(2\pi(i-n)hr\right)}{I_2 \cos\left(2\pi(i-n)hr\right) + Q_2 \sin\left(2\pi(i-n)hr\right)}\right], \\
A_1^2 &= I_1^2 + Q_1^2, \\
\theta_1 &= \tan^{-1}\left[\frac{Q_1}{I_1}\right],
\end{aligned} \tag{4.10}$$

where we use the four-quadrant definition of $\tan^{-1}(\cdot)$, and where

$$\begin{aligned}
I_2 &= m_{m_1 n}(r+1) + m_{in}(r)\cos\theta_1 + \mu_{in}(r)\sin\theta_1 + m_{m_2 n}(r-1)\cos\theta_2 + \mu_{m_2 n}(r-1)\sin\theta_2, \\
Q_2 &= \mu_{m_1 n}(r+1) - m_{in}(r)\sin\theta_1 + \mu_{in}(r)\cos\theta_1 - m_{m_2 n}(r-1)\sin\theta_2 + \mu_{m_2 n}(r-1)\cos\theta_2.
\end{aligned} \tag{4.11}$$

In (4.11), $m_{in}(r)$ and $\mu_{in}(r)$ are the real and imaginary parts of $y_{in}(r)$, respectively, i.e.,

$$m_{in}(r) = \Re\{y_{in}(r)\}, \quad \mu_{in}(r) = \Im\{y_{in}(r)\}, \tag{4.12}$$

and $y_{in}(r)$ (which is, in general, complex) is given by

$$\begin{aligned}
y_{in}(r) = &\frac{z}{z - j2(i-n)h}\left[\Phi\left(\frac{1-r}{\lambda}\right) - \Phi\left(\frac{-r}{\lambda}\right) - \frac{1}{2}e^{-\frac{[2\pi(i-n)h\lambda + j\pi z\lambda]^2}{2} + [-\pi z + j2\pi(i-n)h]r}\right. \\
&\left[\operatorname{erf}\left(\frac{-j2\pi(i-n)h\lambda + \pi z\lambda + \frac{1-r}{\lambda}}{\sqrt{2}}\right) - \operatorname{erf}\left(\frac{-j2\pi(i-n)h\lambda + \pi z\lambda - \frac{r}{\lambda}}{\sqrt{2}}\right)\right] \\
&+ \frac{e^{\pi z - j2\pi(i-n)h} - 1}{2} e^{-\frac{[2\pi(i-n)h\lambda + j\pi z\lambda]^2}{2} + [-\pi z + j2\pi(i-n)h]r} \\
&\left.\left[1 - \operatorname{erf}\left(\frac{-j2\pi(i-n)h\lambda + \pi z\lambda + \frac{1-r}{\lambda}}{\sqrt{2}}\right)\right]\right],
\end{aligned} \tag{4.13}$$

where j is the imaginary unit, $\Phi(\cdot)$ is the cumulative distribution (CDF) of the standard normal

distribution, erf$(\cdot)$ is the error function, and λ is defined as $\lambda \triangleq \frac{\delta}{T} = \frac{\sqrt{\ln 2}}{2\pi z_g}$. The parameters A_1 and θ_1 can be found by letting $n = i$ in Equations (4.11) – (4.13). Detailed analysis to find $y_{in}(r)$ is shown in Appendix K. For the noise parameters in (4.9), the filtered noise power σ^2, the magnitude of the normalized complex cross-covariance $|\rho|$, and the corresponding phase $\phi = \angle\rho$ when the transmitted signal has frequency f_i and the ICI branch is the branch with the 2-pole BPF centered at frequency f_n were found in [34] to be given by

$$\begin{aligned}
\sigma^2 &= \frac{\eta_0 \pi z}{2T}, \\
|\rho| &= \frac{z}{\sqrt{z^2 + [(i-n)h]^2}}, \\
\phi = \angle\rho &= \tan^{-1}\left[\frac{z\sin(2\pi(i-n)hr) - (i-n)h\cos(2\pi(i-n)hr)}{z\cos(2\pi(i-n)hr) + (i-n)h\sin(2\pi(i-n)hr)}\right],
\end{aligned} \tag{4.14}$$

where we still use the four-quadrant definition of the $\tan^{-1}(\cdot)$ function.

We do an exhaustive search to optimize the parameter pair (z, r) of the system with 2-pole BPF detection to minimize the E_b/η_0 required to achieve the BER of 10^{-3}, as a function of z_g and h. The optimal parameters z_{opt}, r_{opt}, and the corresponding performance (E_b/η_0 (dB) at the BER of 10^{-3}) of the optimal 2-pole system, for $z_g = \infty$(i.e., without the Gaussian filter), $1, 0.5$ and $h = 1, 0.95, 0.9, ..., 0.5$, are summarized in Table 4.1 and Fig. 4.2 in Section 4.4, where the accuracy of z is 0.04 (i.e., the values of z we search for are all integer multiples of 0.04), and the accuracy of r is 0.02.

4.2 Demodulator performance in flat, slow Rician fading channels

In a flat, slow Rician fading channel, the signal amplitude $\underline{R}$ is Rician distributed, as shown in (2.30) If we let γ denote the $\frac{E_s}{\eta_0}$ without fading, and $\bar{\gamma}$ denote the average (over the fade)

$\frac{E_s}{\eta_0}$ under Rician fading, then the probability density function (PDF) of γ is given by (2.31).

As is well known, the Rician fading channel reduces to an AWGN channel when $K \to \infty$ and reduces to a Rayleigh fading channel when $K = 0$. For all cases analyzed in the previous section, let $\bar{P}_{b,AWGN}$ denote the union bound on the BER in an AWGN channel. Then the union bound on the average BER in a Rician fading channel can be found by integrating the product of $\bar{P}_{b,AWGN}$ and (2.31) from 0 to ∞.

Note that while the union bound is a tight bound in an AWGN channel, it is not necessarily a tight bound in a Rician fading channel, and as a result, the performance analyzed by the union bound can be somewhat pessimistic in a Rician fading channel, especially in a Rayleigh fading channel, as we will see in Section 4.4.

Similar to the AWGN case, we do an exhaustive search to optimize the parameter pair (z,r) of the two-pole system to minimize E_b/η_0 required to reach the BER of 10^{-3}, as a function of z_g and h. We use the examples of a typical Rician fading channel ($K = 10$) and a Rayleigh fading channel ($K = 0$) to present the numerical results. The optimal parameters z_{opt}, r_{opt} and the corresponding performance of the optimal 2-pole system, for $z_g = \infty, 1, 0.5, h = 1, 0.95, 0.9, ..., 0.5$, and $K = 10, 0$, are summarized in Table 4.1 and Figs. 4.3 and 4.4, where the accuracy is 0.04 for z, and 0.02 for r.

For a coded system with RS coding, we optimize the code dimension k in conjunction with the time-bandwidth parameter z and the normalized sampling time r for the 2-pole system with (n,k) RS codes. We fixed the code length and exhaustively searched all possible values of code dimension, k, to find the k that minimizes the E_b/η_0 required to reach the BER of 10^{-3}.

For the code length of $n = 15$ and the alphabet size of $M = 16$ (i.e., one RS symbol corresponds to one FSK symbol), we repeat the same optimization by exhaustive search as in previous sections while adding one more parameter to optimize: the code dimension k. We optimize the triple (z,r,k) to find the optimal coded performance for a given z_g and h, in an AWGN, Rician ($K = 10$) or Rayleigh fading channel, and measure the coding gain at the BER of

10^{-3} for all cases evaluated in the previous sections. The numerical results are presented in Table 4.2 and Figs. 4.2 – 4.5 in Section 4.4.

If the target BER is smaller, we can use a stronger code. For example, the performance curves using length $n = 255$ RS code are shown in Figs. 4.7 – 4.9 in Section 4.4. While we are supposed to optimize the triple $(z_{opt}, r_{opt}, k_{opt})$ using length $n = 255$ RS code, since the range of code dimension k is $k \in \{1, 3, \ldots, 253\}$, the optimization would take too long and thus we use (z_{opt}, r_{opt}) of the corresponding cases for $n = 15$ RS code, and only optimize the code dimension k for $n = 255$ RS code.

4.3 Numerical Results

In this section, we present the numerical results of the previous sections. Our baseline design of $M = 16$ applies to all the figures in this section. Furthermore, the Rician K-factor is $K = 10$ and the RS code length is $n = 15$ r 255 for the coded cases. The metric to evaluate performance is the E_b/η_0 measured at the BER of 10^{-3}, and coding gain is also measured at this BER. Table 4.1 lists the optimal parameter pair (z_{opt}, r_{opt}) for the uncoded GFSK system with $z_g \in \{\infty, 1, 0.5\}$ in an AWGN, Rician and Rayleigh fading channel. Table 4.2 lists the optimal parameter triple $(z_{opt}, r_{opt}, k_{opt})$ for the coded GFSK system with $z_g \in \{\infty, 1, 0.5\}$ in an AWGN, Rician and Rayleigh fading channel. Figs. 4.2 – 4.4 show the optimal coded ($n = 15$) and uncoded performance as a function of the modulation index h and the time-bandwidth product of the lowpass equivalent Gaussian filter z_g, for h between 0.5 and 1 (i.e., up to 50% saving in bandwidth) and $z_g \in \{0.5, 1, \infty\}$, in an AWGN, Rician or Rayleigh fading channel, respectively. Fig. 4.5 summarizes the coding gain for different parameters (z_g, h) and channel conditions, and Fig. 4.6 summarizes the power-bandwidth tradeoff of the GFSK system in terms of system bandwidth saved vs. loss in E_b/η_0. Figs. 4.7 – 4.9 show three examples of optimal coded ($n = 15$ and 255) and uncoded performance curves in terms of P_b vs. E_b/η_0 (where the optimal parameters for the

coded and uncoded systems are possibly different). We use monte-carlo simulation to support the analysis in this paper, where the number of errors collected is 1000 for each data point.

Some observations from the figures and tables are as follows:

By the nature of union bound, it is an upper bound that is not always a tight bound, and for our case, in a fading channel, it provides a pessimistic estimate. We need to resort to accurate simulation (collect enough errors) for the exact performance. Furthermore, the gap between the actual performance and the union bound decreases with K: in a Rayleigh fading channel, it can be over 6 dB, in a Rician fading channel, it is roughly 1 dB and in an AWGN channel, since the union bound is tight, the gap is negligible at $P_b = 10^{-3}$, as can be seen in Figs. 4.7 – 4.9, for the uncoded cases. If we use the union bound to compare the performance in different channel conditions, we will get inaccurate results.

The analysis is less accurate when z_g is smaller. This is because ISI becomes more severe and more pulses other than the immediate previous and future pulse can affect the decision on the current symbol, and since the analysis only considers the immediate previous and future pulse as the source of ISI, it tends to give overly optimistic results. However, for the values of z_g we chose, the analysis is accurate, as can be seen in Figs. 4.7 – 4.9.

For any z_g and any channel condition, the performance degrades with decreasing h, but the performance degrades faster when K is larger and when z_g is smaller.

For any h and any channel condition, a smaller z_g can make the transition between FSK symbols smoother and thus decrease out-of-band spectrum, at the cost of more performance degradation.

For any z_g and any channel condition, the performance degrades faster with decreasing h for an uncoded system, compared to a coded system, meaning the power-bandwidth tradeoff leans towards bandwidth for a coded system. For example, for $z = 0.5$ in a Rician fading channel the performance degradation between $h = 0.5$ and $h = 1$ (i.e., the amount of performance loss to save 50% of bandwidth) is 2.4 dB for a coded system, and 6.8 dB for an uncoded system. It can

be inferred that if a more powerful code is used (e.g., $n = 255$ RS code) and optimized, then we could save more bandwidth for the same amount of performance degradation, and the results will be shown when they are ready... the joint optimization is impossible because the code dimension $k \in \{1, 3, ..., 253\}$ and this range is way too large to search in.

For any h and any channel condition, the coding gain increases with decreasing h. Furthermore, the coding gain is smaller when K is larger, but also increases faster with decreasing h. This is intuitive since coding is more effective for worse uncoded performance.

The performance degradation increases faster when h is smaller – when the bandwidth is already small, we need to sacrifice more power in order to further save bandwidth, e.g., for the case of coded 2-pole GFSK system with $z_g = 1$ in an AWGN channel, we sacrifice 0.8 dB in performance for 30% saving in bandwidth, but we need to sacrifice another 2.5 dB (i.e., 3.3 dB in total) in performance for another 20% (i.e., 50% in total) saving in bandwidth. This is similar (but opposite) to the diminishing return of M-ary FSK for large M.

As can be seen in Tables 4.1 and 4.2, the optimal z increases with decreasing h, regardless of whether the system is coded or not. This is because decreasing h results in more severe ICI and ISI, and we have to use larger z to reduce ISI, at the cost of increasing the noise power going into the system.

It can be seen from the tables that for all cases we evaluated, the optimal r is 1 without Gaussian filtering (i.e., $z_g = \infty$), which is consistent with what we found in [34], and for most cases we evaluated, the optimal r is in the vicinity of 0.9 with Gaussian filtering. This is due to the pulse shaping effect of the Gaussian filter, making the filtered signal waveform peak before the end of the symbol duration.

It can be seen from Fig. 4.6 that for all cases we analyzed, i.e., any $z_g \in \{\infty, 1, 0.5\}$ and any channel condition, we can achieve at least a 30% saving in bandwidth at the cost of no more than 0.9 dB loss in power when all the parameters of the coded 2-pole system are optimized.

The performance loss of a GFSK system compared to the corresponding MFSK system is

a function of z_g and h. Specifically, it is a decreasing function of both z_g and h.

Table 4.1: Optimal parameters (z_{opt}, r_{opt}), uncoded.

	z_g \ h		1	0.95	0.9	0.85	0.8	0.75	0.7	0.65	0.6	0.55	0.5
AWGN	∞	z_{opt}	0.52	0.52	0.56	0.56	0.56	0.6	0.64	0.72	0.8	0.88	0.96
		r_{opt}	1	1	1	1	1	1	1	1	1	1	1
	1	z_{opt}	0.6	0.6	0.6	0.6	0.64	0.68	0.76	0.88	0.96	1.08	1.2
		r_{opt}	0.92	0.92	0.92	0.94	0.94	0.94	0.94	0.92	0.92	0.9	0.88
	0.5	z_{opt}	0.64	0.64	0.64	0.64	0.68	0.72	0.8	0.92	1.08	1.28	1.44
		r_{opt}	0.88	0.9	0.9	0.92	0.92	0.92	0.92	0.9	0.88	0.84	0.82
Rician ($K = 10$)	∞	z_{opt}	0.48	0.48	0.48	0.48	0.52	0.52	0.56	0.64	0.72	0.8	0.88
		r_{opt}	1	1	1	1	1	1	1	1	1	1	1
	1	z_{opt}	0.52	0.52	0.52	0.52	0.56	0.6	0.68	0.8	0.88	1	1.08
		r_{opt}	0.92	0.92	0.94	0.94	0.94	0.94	0.94	0.92	0.92	0.9	0.9
	0.5	z_{opt}	0.56	0.56	0.56	0.56	0.6	0.64	0.76	0.88	1	1.16	1.4
		r_{opt}	0.9	0.9	0.92	0.92	0.92	0.92	0.92	0.92	0.88	0.86	0.82
Rayleigh	∞	z_{opt}	0.44	0.44	0.44	0.44	0.48	0.48	0.48	0.52	0.56	0.6	0.68
		r_{opt}	1	1	1	1	1	1	1	1	1	1	1
	1	z_{opt}	0.44	0.44	0.44	0.48	0.48	0.48	0.52	0.56	0.64	0.76	0.84
		r_{opt}	0.94	0.94	0.94	0.94	0.94	0.94	0.94	0.94	0.94	0.92	0.92
	0.5	z_{opt}	0.44	0.44	0.44	0.44	0.44	0.48	0.52	0.64	0.76	0.88	1
		r_{opt}	0.92	0.92	0.92	0.94	0.94	0.94	0.94	0.92	0.9	0.9	0.88

Table 4.2: Optimal parameters $(z_{opt}, r_{opt}, k_{opt})$, coded.

	z_g \ h		1	0.95	0.9	0.85	0.8	0.75	0.7	0.65	0.6	0.55	0.5
AWGN	∞	z_{opt}	0.48	0.48	0.52	0.52	0.52	0.52	0.56	0.6	0.64	0.72	0.72
		r_{opt}	1	1	1	1	1	1	1	1	1	1	1
		k_{opt}	13	13	13	13	11	11	11	11	11	11	9
	1	z_{opt}	0.52	0.52	0.52	0.52	0.56	0.56	0.6	0.64	0.68	0.72	0.84
		r_{opt}	0.92	0.94	0.94	0.94	0.94	0.94	0.94	0.94	0.94	0.94	0.92
		k_{opt}	11	11	11	11	11	11	11	11	11	9	9
	0.5	z_{opt}	0.56	0.56	0.56	0.56	0.56	0.56	0.56	0.56	0.6	0.64	0.68
		r_{opt}	0.9	0.9	0.9	0.9	0.9	0.92	0.94	0.94	0.94	0.94	0.92
		k_{opt}	11	11	11	11	11	11	11	9	9	9	7
Rician ($K = 10$)	∞	z_{opt}	0.48	0.48	0.48	0.48	0.52	0.52	0.52	0.56	0.6	0.68	0.72
		r_{opt}	1	1	1	1	1	1	1	1	1	1	1
		k_{opt}	11	11	11	11	11	11	11	11	9	9	9
	1	z_{opt}	0.52	0.48	0.52	0.52	0.52	0.52	0.56	0.6	0.64	0.72	0.84
		r_{opt}	0.92	0.92	0.92	0.94	0.94	0.94	0.94	0.94	0.94	0.94	0.92
		k_{opt}	11	11	11	11	9	9	9	9	9	9	9
	0.5	z_{opt}	0.48	0.52	0.52	0.52	0.52	0.52	0.52	0.56	0.6	0.68	0.76
		r_{opt}	0.92	0.92	0.92	0.92	0.92	0.92	0.94	0.94	0.94	0.94	0.92
		k_{opt}	9	9	9	9	9	9	9	9	9	9	9
Rayleigh	∞	z_{opt}	0.44	0.44	0.44	0.44	0.44	0.48	0.48	0.48	0.52	0.6	0.68
		r_{opt}	1	1	1	1	1	1	1	1	1	1	1
		k_{opt}	5	5	5	5	5	5	5	5	5	5	5
	1	z_{opt}	0.44	0.48	0.48	0.48	0.48	0.48	0.52	0.56	0.6	0.68	0.76
		r_{opt}	0.92	0.94	0.94	0.94	0.94	0.94	0.94	0.94	0.94	0.94	0.94
		k_{opt}	5	5	5	5	5	5	5	5	5	5	5
	0.5	z_{opt}	0.44	0.44	0.44	0.44	0.44	0.44	0.48	0.52	0.56	0.64	0.72
		r_{opt}	0.92	0.92	0.92	0.92	0.94	0.94	0.94	0.94	0.94	0.94	0.94
		k_{opt}	5	5	5	5	5	5	5	5	5	5	5

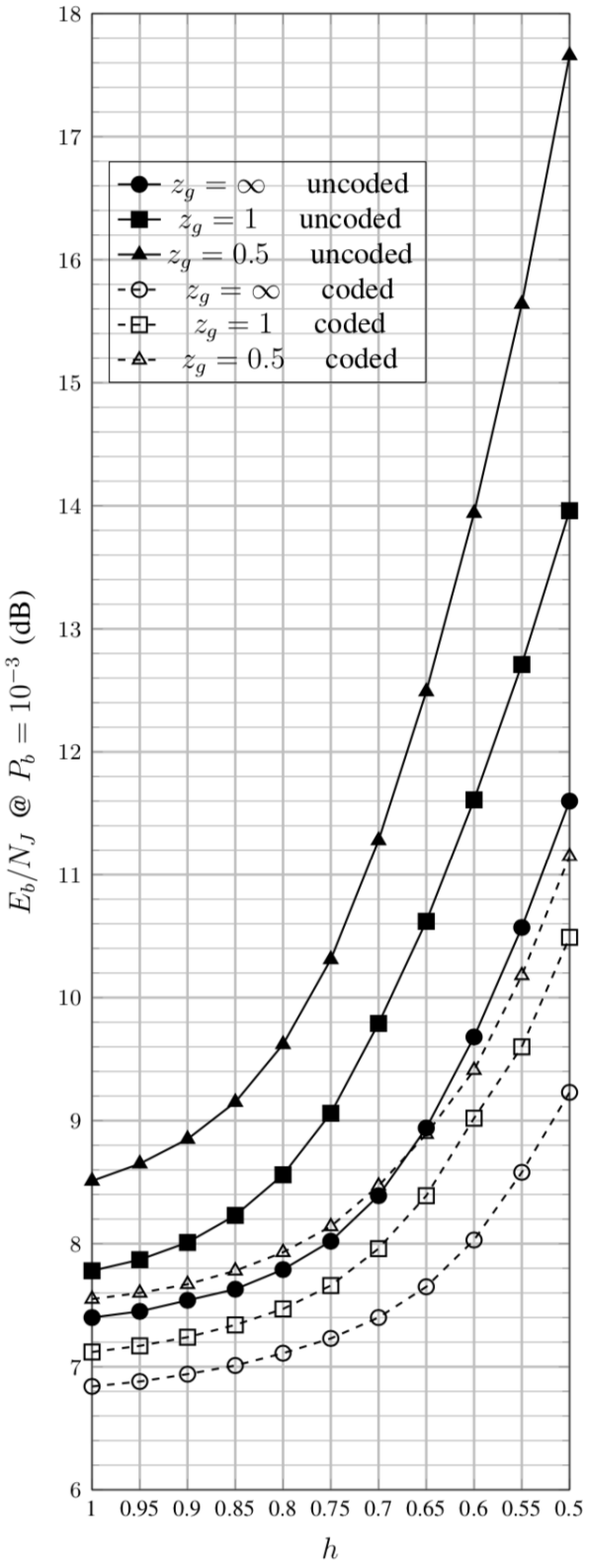

Figure 4.2: AWGN

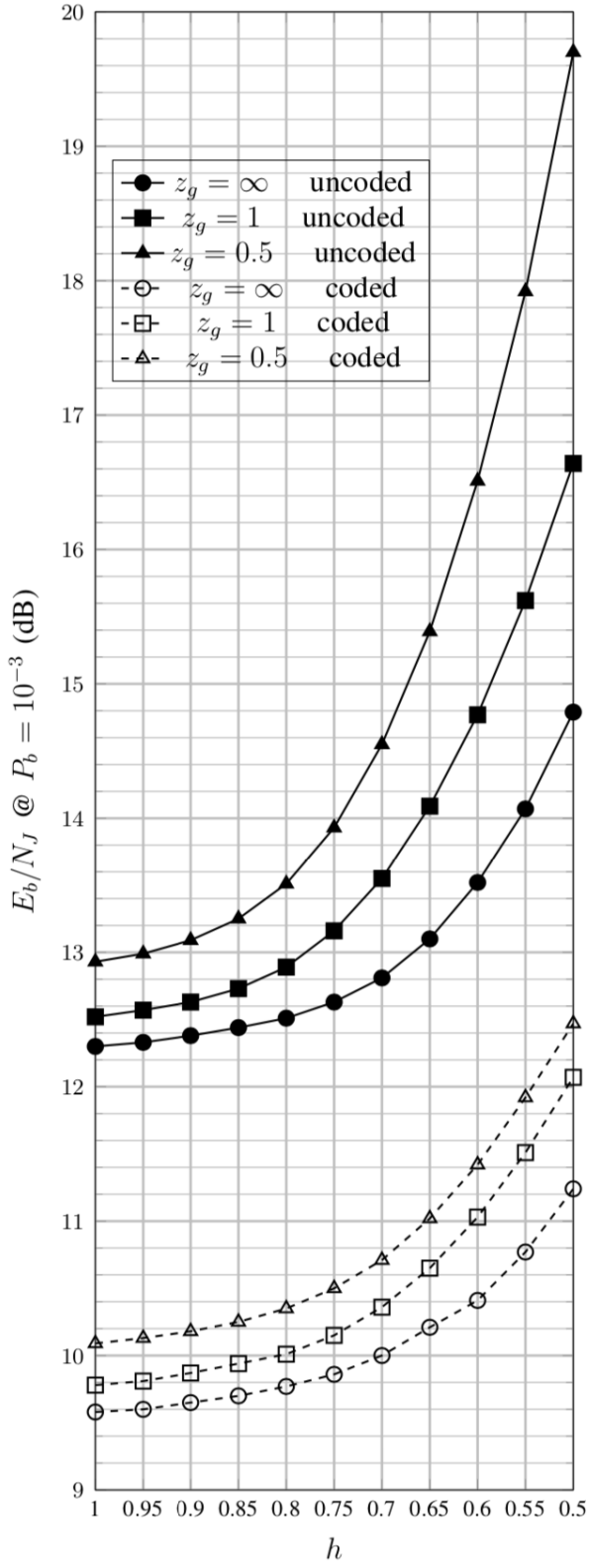

Figure 4.3: Rician ($K = 10$)

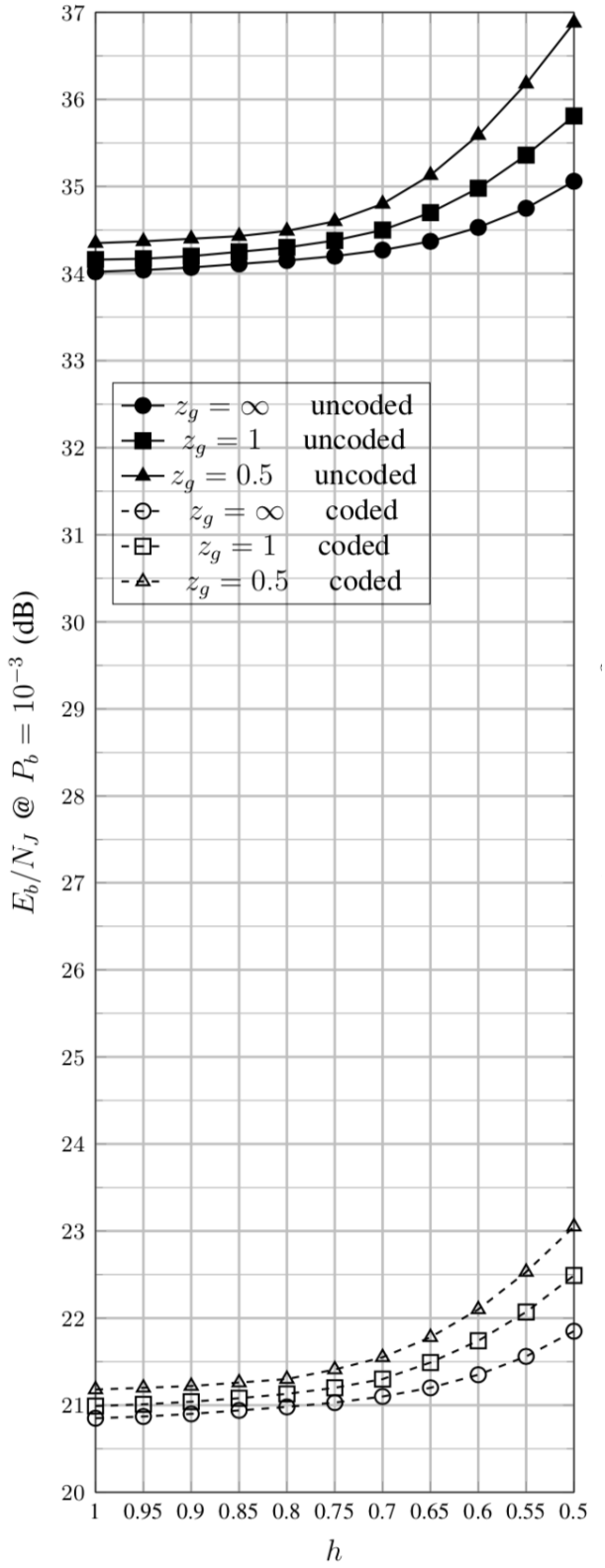

Figure 4.4: Rayleigh

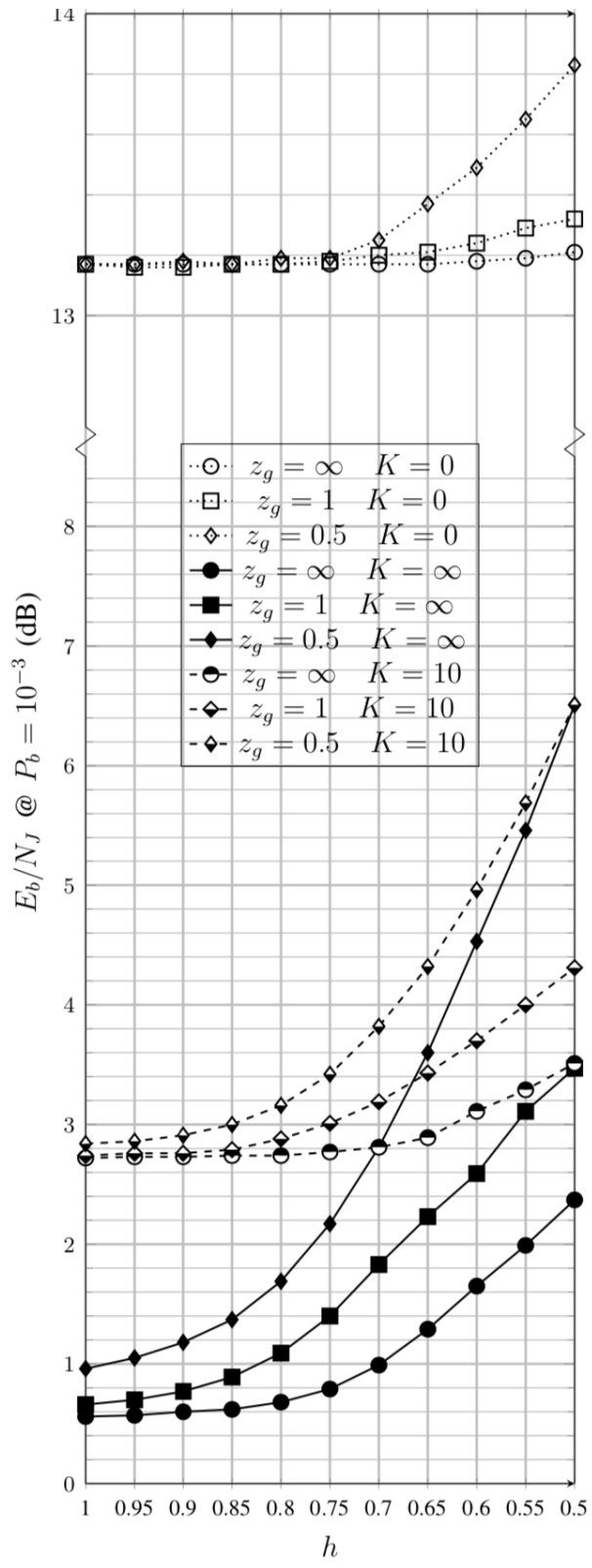

Figure 4.5: Coding gain

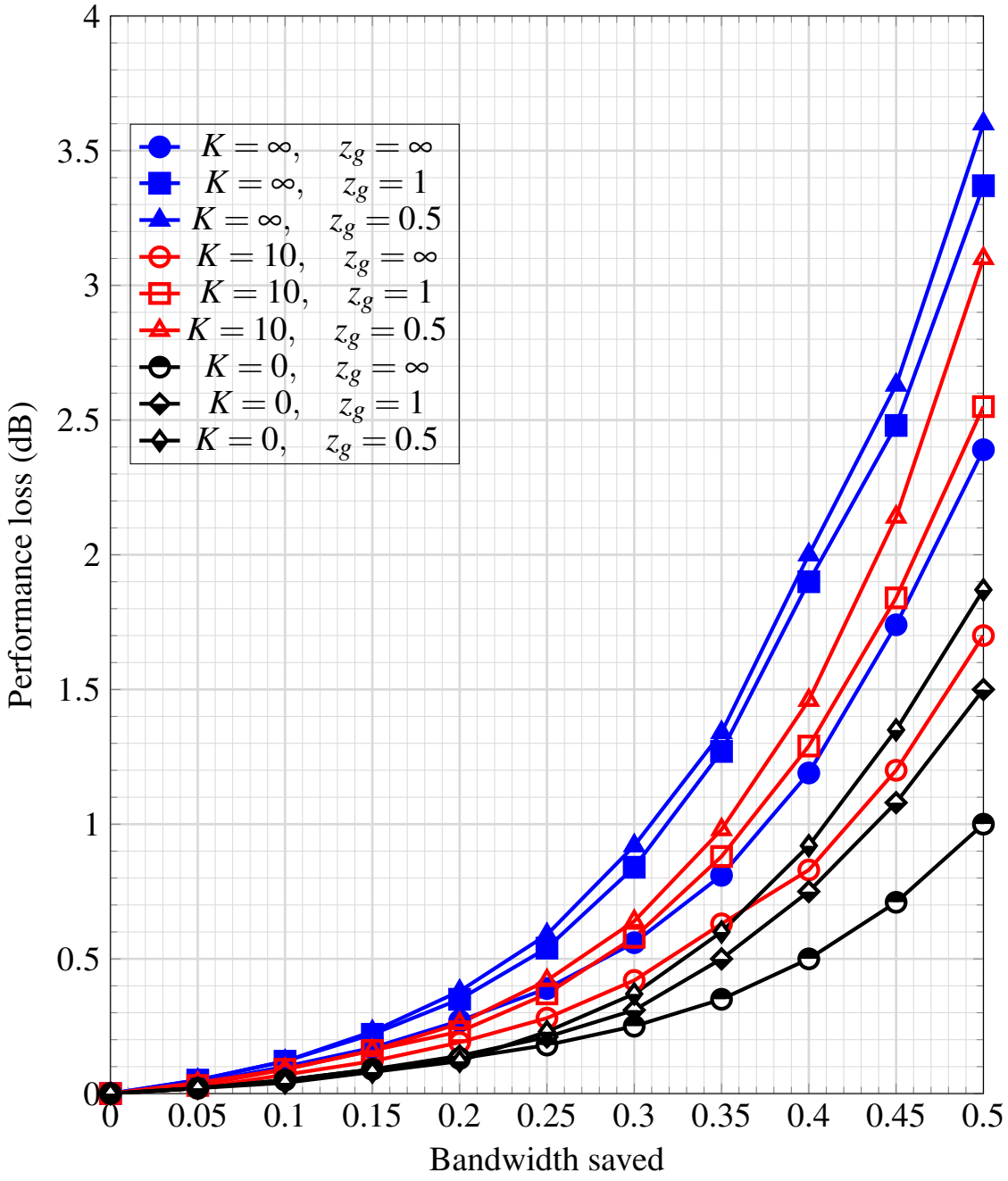

Figure 4.6: Performance loss vs. bandwidth saved

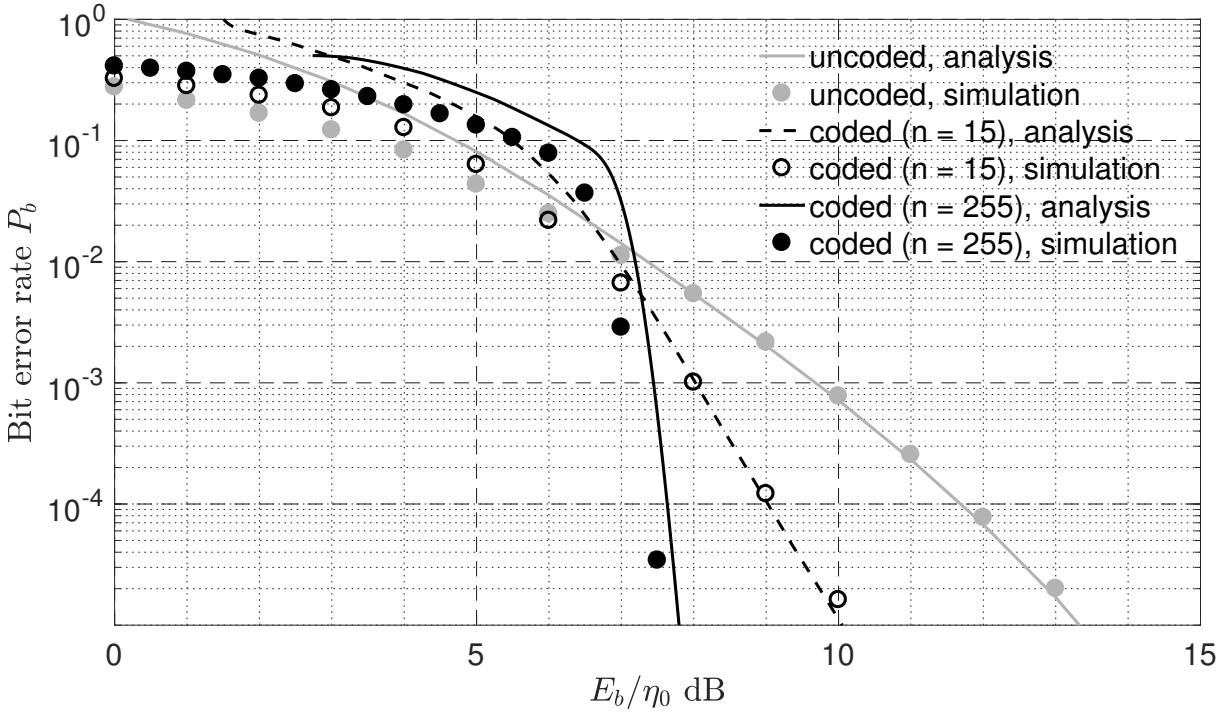

Figure 4.7: AWGN, $z_g = \infty, h = 0.6$.

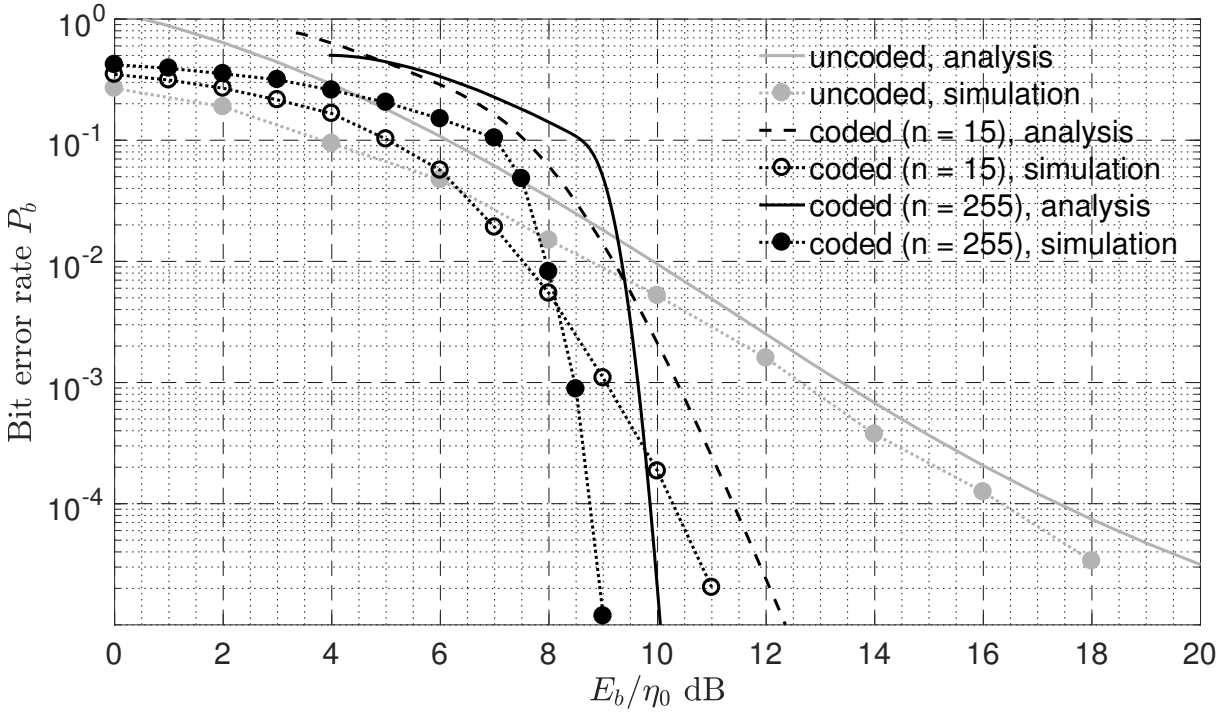

Figure 4.8: Rician ($K = 10$), $z_g = 1, h = 0.7$.

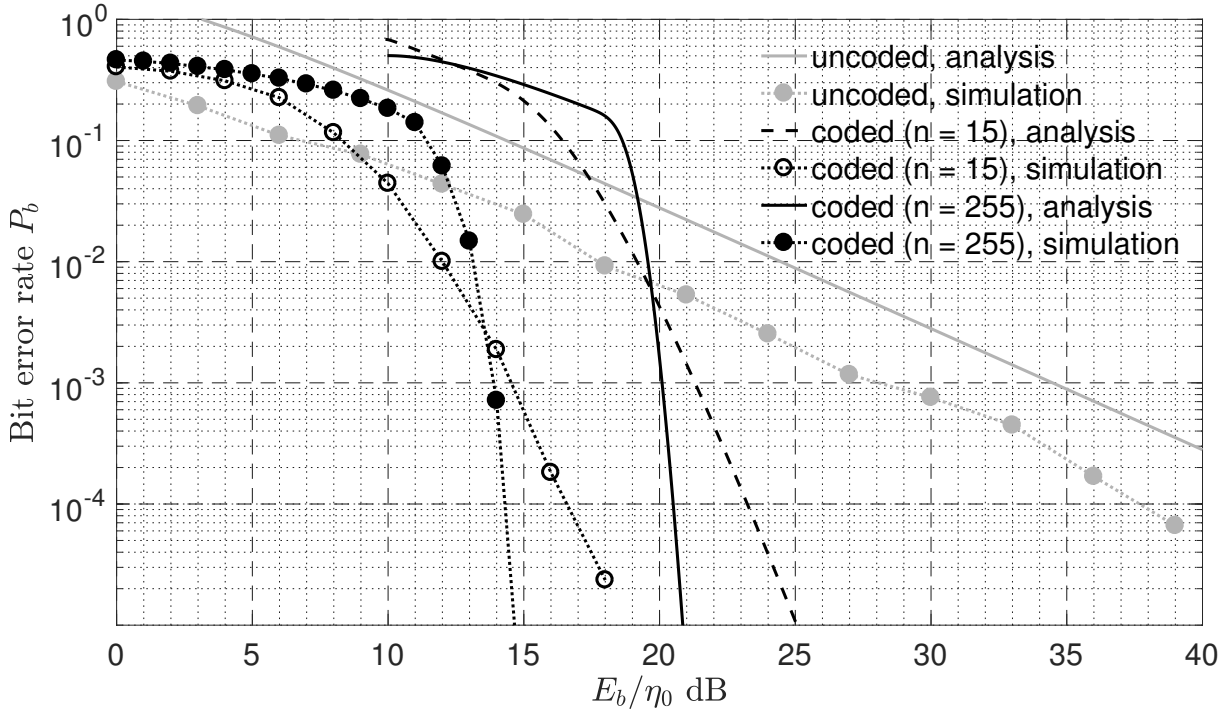

Figure 4.9: Rayleigh, $z_g = 0.5, h = 0.8$.

The text of this chapter is, in part, a reprint of the paper, "Performance analysis for an ultra-low power GFSK system", submitted to *IEEE Transactions on Communications*. The dissertation author is the primary researcher and author of the paper.

Chapter 5

Conclusion

The essence of Chapter 2 was the use of a spectrally-inefficient, but power-efficient, waveform, in conjunction with low complexity filtering, and low complexity demodulation, with the goal of minimizing transmission energy consumption, subject to a predetermined average probability of error. Hence we chose non-coherent MFSK instead of coherent MQAM, we chose RS encoding with hard-decision decoding instead of soft-decision iterative decoding for a capacity-approaching code, and we chose simple two-pole bandpass filters instead of matched filters. What we found was that by carefully optimizing the system parameters, such as filter bandwidth, tone spacing, sampling time and code dimension, we could achieve the desired performance with a penalty in E_b/N_0 of at most 1.2 dB compared to a more conventional design using non-coherent FSK with matched filter detection.

We specifically compared the performance of an MFSK non-coherent receiver when the matched filters are replaced by 2-pole BPFs, for AWGN, Rayleigh, and Rician (K=10) channels, both with and without phase continuity. We chose $M = 16$ as our baseline design, because going to $M = 32$ results in twice the bandwidth and twice the complexity, while only yielding roughly a 0.6dB gain in E_b/N_0, as can be seen in Table 2.1. We further considered a coded system with Reed-Solomon codes. For both coded and uncoded systems, the peak performance degradation

occurs in the absence of fading when we use BFSK and we have discontinuous phase, where the difference between using two-pole BPFs and matched filters is about 1.5dB. In all channels we evaluated, the demodulator performance with phase continuity was better than that without phase continuity, but the difference decreases with the alphabet size M. For BFSK, a continuous phase system can outperform its discontinuous phase counterpart by as much as 1.5dB, while the difference reduces to less than 0.2dB when $M = 16$. More specifically, for $M = 16$, the largest performance degradation is when the channel is AWGN, and the corresponding performance degradation is about 1dB with or without phase continuity. For an RS (code length 15 or 255)-encoded system with 16FSK in a Rician fading channel, the optimal code parameters, as well as the coding gain, vary with the K-factor. For a Rayleigh/Rician(K=10)/AWGN channel, the coding gain is about 30/9/1.4 dB, respectively, at bit error rate 10^{-5}, for code length 15, and about 34/11/2.9 dB, respectively, for code length 255.

In Chapter 3, we further considered fast frequency hopping and intentional jamming, in both fading and non-fading environments, with the goal of minimizing overall power consumption. We compared the performance of an FFH-MFSK non-coherent receiver when the matched filters are replaced by 2-pole BPFs, for AWGN, Rayleigh, and Rician (K=10) channels. We further considered a coded system with RS encoding and hard-decision decoding. What we found was that by carefully optimizing the system parameters, such as filter bandwidth and code dimension, we could achieve the desired performance with a penalty in E_b/N_J of 0.8–1.8 dB compared to the more conventional design using non-coherent FSK with matched filter detection. To be specific, with full-band noise jamming, the 1.8 dB, performance degradation only occurs when we use diversity combining in a Rayleigh fading channel. In all other cases, the performance degradation is between 1.0 dB and 1.4 dB, which is consistent with what we found in [34]. With PBJ, the performance degradation was between 0.8 dB and 0.9 dB. With MTJ, we found that the worst-case performance of an FFH-MFSK system with 2-pole BPF detection was no worse than the corresponding MF system: in a non-fading channel, the 2-pole system outperforms the

corresponding MF system by 2.4 dB for $M = 2$ and 2.2 dB for $M = 16$, and in a Rician fading channel, the performances of the two systems are identical at the NE, because an NE is reached when filter bandwidth is large, and thus ISI is negligible.

In Chapter 4, we further showed that compared to the system proposed in Chapter 2, we could potentially save a large fraction of total system bandwidth at the cost of a small extra performance loss by decreasing the tone spacing and optimizing key parameters, including filter bandwidth, sampling time and code dimension. For a fixed loss in performance, the saving in system bandwidth was greater when the channel condition was worse, i.e., when the Rician K-factor was smaller. For example, in an AWGN channel, we could save 30% of system bandwidth at the cost of 0.56 dB in performance, or we could save 50% of bandwidth at the cost of 2.4 dB in performance, where the metric to compare performance was E_b/η_0 measured at the BER of 10^{-3} for the optimal coded system; while in a Rayleigh fading channel, we could save 30% of system bandwidth at the cost of 0.25 dB in performance, or we could save 50% of system bandwidth at the cost of 1 dB in performance.

Furthermore, we extended the results to a GFSK system where a Gaussian filter is used to smooth the transition between pulses, and decrease out-of-band spectrum. We quantified the performance degradation of the GFSK system compared to the corresponding MFSK system, as a function of the time-bandwidth product (z_g) of the Gaussian filter, and the fraction of bandwidth saved. For example, if we want to save 25% of system bandwidth and we use Gaussian filter with time-bandwidth product $z_g = 1$, the optimal coded GFSK system is worse than the optimal coded MFSK system by 1.4 dB.

Appendix A

Non-orthogonal signaling and continuous phase

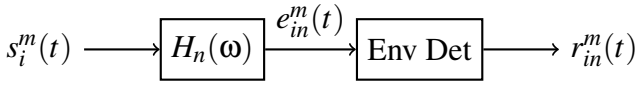

Figure A1: Signal filtering (2-pole)

For the block diagram shown in Fig. A1, we first consider filtering a single pulse given by

$$s_i(\theta,t) = A\cos(2\pi f_i t + \theta)P_{\frac{T}{2}}(t - \frac{T}{2}). \tag{A.1}$$

The output $e_{in}(\theta,t)$ can be expressed as

$$e_{in}(\theta,t) = m_{in}(t)\cos(2\pi f_n t + \theta) - \mu_{in}(t)\sin(2\pi f_n t + \theta), \tag{A.2}$$

where $\Delta\omega_{in} = 2\pi\Delta f_{in} = 2\pi(i-n)\Delta f$,

$$m_{in}(t) = \frac{A\pi W}{(\Delta\omega_{in})^2 + (\pi W)^2} \begin{cases} \Big[(\Delta\omega_{in}\sin(\Delta\omega_{in}t) + \pi W\cos(\Delta\omega_{in}t)) - \pi W e^{-\pi W t}\Big], & 0 \leqslant t \leqslant T \\ \Big[e^{\pi W T}(\Delta\omega_{in}\sin(\Delta\omega_{in}T) + \pi W\cos(\Delta\omega_{in}T)) - \pi W\Big]e^{-\pi W t}, & t \geqslant T \end{cases} \tag{A.3}$$

and

$$\mu_{in}(t) = \frac{A\pi W}{(\Delta\omega_{in})^2 + (\pi W)^2} \begin{cases} \Big[(\pi W\sin(\Delta\omega_{in}t) - \Delta\omega_{in}\cos(\Delta\omega_{in}t)) + \Delta\omega_{in}e^{-\pi W t}\Big], & 0 \leqslant t \leqslant T \\ \Big[e^{\pi W T}(\pi W\sin(\Delta\omega_{in}T) - \Delta\omega_{in}\cos(\Delta\omega_{in}T) + \Delta\omega_{in}\Big]e^{-\pi W t}, & t \geqslant T \end{cases} \tag{A.4}$$

Based on this, we consider filtering two consecutive pulses (p^{th} and $(p-1)^{st}$). Let the input signal be $s_i^m(t)$, where the current (p^{th}) symbol is at frequency f_i, and the previous symbol is at frequency f_m, and let the corresponding output signal of the n^{th} filter be $e_{in}^m(t)$. That is, if

$$\begin{aligned} s_i^m(t) =& s_i(\theta_p, t-(p-1)T) + s_m(\theta_{p-1}, t-(p-2)T) \\ =& A\cos(2\pi f_i(t-(p-1)T)+\theta_p)P_{\frac{T}{2}}(t-\frac{T}{2}-(p-1)T)+ \\ & A\cos(2\pi f_m(t-(p-2)T)+\theta_{p-1})P_{\frac{T}{2}}(t-\frac{T}{2}-(p-2)T), \end{aligned} \tag{A.5}$$

then the output is

$$\begin{aligned} e_{in}^m(t) &= e_{in}(\theta_p, t-(p-1)T) + e_{mn}(\theta_{p-1}, t-(p-2)T) \\ &= m_{in}(t-(p-1)T)\cos(2\pi f_n(t-(p-1)T)+\theta_p)- \\ &\quad \mu_{in}(t-(p-1)T)\sin(2\pi f_n(t-(p-1)T)+\theta_p)+ \\ &\quad m_{mn}(t-(p-2)T)\cos(2\pi f_n(t-(p-2)T)+\theta_{p-1})- \\ &\quad \mu_{mn}(t-(p-2)T)\sin(2\pi f_n(t-(p-2)T)+\theta_{p-1}). \end{aligned} \tag{A.6}$$

where we used (A.3) and (A.4). Simplifying (A.6) yields

$$e_{in}^{m}(t) \triangleq a(t)\cdot\cos(2\pi f_n t+\theta_{p-1})-b(t)\cdot\sin(2\pi f_n t+\theta_{p-1}), \tag{A.7}$$

where

$$\begin{aligned} a(t) \triangleq & m_{in}(t-(p-1)T)\cos[(2\pi f_n(p-1)T-(\theta_p-\theta_{p-1}))]+ \\ & \mu_{in}(t-(p-1)T)\sin[(2\pi f_n(p-1)T-(\theta_p-\theta_{p-1}))]+ \\ & m_{mn}(t-(p-2)T)\cos[2\pi f_n(p-2)T]+ \\ & \mu_{mn}(t-(p-2)T)\sin[2\pi f_n(p-2)T], \end{aligned} \tag{A.8}$$

and

$$\begin{aligned} b(t) \triangleq & -m_{in}(t-(p-1)T)\sin[(2\pi f_n(p-1)T-(\theta_p-\theta_{p-1}))] \\ & +\mu_{in}(t-(p-1)T)\cos[(2\pi f_n(p-1)T-(\theta_p-\theta_{p-1}))] \\ & -m_{mn}(t-(p-2)T)\sin[2\pi f_n(p-2)T] \\ & +\mu_{mn}(t-(p-2)T)\cos[2\pi f_n(p-2)T]. \end{aligned} \tag{A.9}$$

Next we find the envelope of $e_{in}^{m}(t)$ and sample at $t=(p-1)T+T_s \triangleq T'$. Without loss of generality, if we assume $\theta_{p-1}=0$, then the envelope and corresponding phase, when sampled at $t=T'$, are

$$r_{in}^{m}(T') = \sqrt{a^2(T')+b^2(T')}, \tag{A.10a}$$

$$\theta_{in}^{m}(T') = \tan^{-1}\left[\frac{b(T')}{a(T')}\right]. \tag{A.10b}$$

To simplify (A.10), first notice that

$$\Delta\omega_{in}T_s = 2\pi(i-n)\Delta f T_s = 2\pi(i-n)\Delta f T \cdot T_s/T = 2hr(i-n)\pi. \tag{A.11}$$

Then,

$$\begin{aligned} &m_{in}(t-(p-1)T)|_{t=(p-1)T+T_s} = m_{in}(T_s) \\ =&\frac{Az}{(2(i-n)h)^2+z^2}\left[\Big(2(i-n)h\sin(2hr(i-n)\pi)+z\cos(2hr(i-n)\pi)\Big)-ze^{-\pi zr}\right]. \end{aligned} \tag{A.12}$$

Similarly,

$$\begin{aligned} &\mu_{in}(t-(p-1)T)|_{t=(p-1)T+T_s} = \mu_{in}(T_s) \\ =&\frac{Az}{(2(i-n)h)^2+z^2}\left[\Big(z\sin(2hr(i-n)\pi)-2(i-n)h\cos(2hr(i-n)\pi)\Big)+2(i-n)he^{-\pi zr}\right], \end{aligned} \tag{A.13}$$

$$\begin{aligned} &m_{mn}(t-(p-2)T)|_{t=(p-1)T+T_s} = m_{mn}(T+T_s) \\ =&\frac{Aze^{-\pi z(1+r)}}{(2(m-n)h)^2+z^2}\left[e^{\pi z}\Big(2(m-n)h\sin(2h(m-n)\pi)+z\cos(2h(m-n)\pi)\Big)-z\right], \end{aligned} \tag{A.14}$$

and,

$$\begin{aligned} &\mu_{mn}(t-(p-2)T)|_{t=(p-1)T+T_s} = \mu_{mn}(T+T_s) \\ =&\frac{Aze^{-\pi z(1+r)}}{(2(m-n)h)^2+z^2}\left[e^{\pi z}\Big(z\sin(2h(m-n)\pi)-2(m-n)h\cos(2h(m-n)\pi)\Big)+2(m-n)h\right]. \end{aligned} \tag{A.15}$$

With the assumption $\theta_{p-1} = 0$ and sampling at $t = T'$, we rewrite (A.8) and (A.9) as

$$\begin{aligned}
&a(T') \\
=&m_{in}(T_s)\cos[(2\pi f_n(p-1)T - \theta_p)] + \mu_{in}(T_s)\sin[(2\pi f_n(p-1)T - \theta_p)] \\
+&m_{mn}(T+T_s)\cos[(2\pi f_n(p-1)T - 2\pi f_n T)] + \mu_{mn}(T+T_s)\sin[(2\pi f_n(p-1)T - 2\pi f_n T)] \\
=&[m_{in}(T_s)\cos(\theta_p) - \mu_{in}(T_s)\sin(\theta_p) + \\
&m_{mn}(T+T_s)\cos(2\pi f_n T) - \mu_{mn}(T+T_s)\sin(2\pi f_n T)]\cos(2\pi f_n(p-1)T) \\
+&[m_{in}(T_s)\sin(\theta_p) + \mu_{in}(T_s)\cos(\theta_p) + \\
&m_{mn}(T+T_s)\sin(2\pi f_n T) + \mu_{mn}(T+T_s)\cos(2\pi f_n T)]\sin(2\pi f_n(p-1)T) \\
\triangleq&A\cdot\cos(2\pi f_n(p-1)T) + B\cdot\sin(2\pi f_n(p-1)T),
\end{aligned} \tag{A.16}$$

and

$$\begin{aligned}
&b(T') \\
=&[m_{in}(T_s)\sin(\theta_p) + \mu_{in}(T_s)\cos(\theta_p) + \\
&m_{mn}(T+T_s)\sin(2\pi f_n T) + \mu_{mn}(T+T_s)\cos(2\pi f_n T)]\cos(2\pi f_n(p-1)T) \\
+&[-m_{in}(T_s)\cos(\theta_p) + \mu_{in}(T_s)\sin(\theta_p) \\
&- m_{mn}(T+T_s)\cos(2\pi f_n T) + \mu_{mn}(T+T_s)\sin(2\pi f_n T)]\sin(2\pi f_n(p-1)T) \\
=&B\cdot\cos(2\pi f_n(p-1)T) - A\cdot\sin(2\pi f_n(p-1)T).
\end{aligned} \tag{A.17}$$

From (A.16) and (A.17), we obtain

$$\begin{aligned}
&a^2((p-1)T+T_s) + b^2((p-1)T+T_s) \\
=&(A^2+B^2)\cdot\cos^2(2\pi f_n(p-1)T) + (A^2+B^2)\cdot\sin^2(2\pi f_n(p-1)T) = A^2+B^2.
\end{aligned} \tag{A.18}$$

Then, the output in Fig. A1, along with the phase, are given by

$$r_{in}^{m}(T') = \sqrt{a^2((p-1)T+T_s)+b^2((p-1)T+T_s)} = \sqrt{A^2+B^2}, \tag{A.19}$$

and

$$\theta_{in}^{m}(T') = \tan^{-1}\left[\frac{b((p-1)T+T_s)}{a((p-1)T+T_s)}\right]. \tag{A.20}$$

The signal amplitude and phase at the output of the filters in (2.18) are

$$A_1 = r_{ii}^{m}(T'), \quad A_2 = r_{in}^{m}(T'), \quad \theta_1 = \theta_{ii}^{m}(T'), \quad \theta_2 = \theta_{in}^{m}(T'). \tag{A.21}$$

Now consider the noise. We will derive the normalized complex cross-covariance and the corresponding phase between the two stationary Gaussian-noise processes $\underline{n}_i(t)$ and $\underline{n}_n(t)$ in Fig. A2.

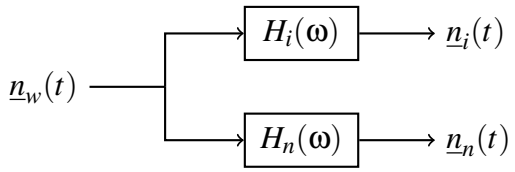

Figure A2: Noise filtering (2-pole)

We express $\underline{n}_i(t)$ and $\underline{n}_n(t)$ as

$$\begin{aligned} \underline{n}_i(t) &= \underline{n}_{ci}(t)\cos(\omega_i t) - \underline{n}_{si}(t)\sin(\omega_i t), \\ \underline{n}_n(t) &= \underline{n}_{cn}(t)\cos(\omega_n t) - \underline{n}_{sn}(t)\sin(\omega_n t). \end{aligned} \tag{A.22}$$

It can be shown that the filtered noise power σ^2 with 2-pole BPF is

$$\sigma^2 = \frac{N_0}{2}\oint h_i(\tau)^2 d\tau = \frac{N_0 \pi W}{2}, \quad \forall i. \tag{A.23}$$

From chapter 1 of [15], letting $\hat{n}(t)$ be the Hilbert transform of $n(t)$, we have

$$\begin{aligned}
&\underline{n}_{ci}(t) = \underline{n}_i(t)\cos(\omega_i t) + \hat{\underline{n}}_i(t)\sin(\omega_i t), \quad \underline{n}_{si}(t) = \hat{\underline{n}}_i(t)\cos(\omega_i t) - \underline{n}_i(t)\sin(\omega_i t), \\
&\underline{n}_{cn}(t) = \underline{n}_n(t)\cos(\omega_n t) + \hat{\underline{n}}_n(t)\sin(\omega_n t), \quad \underline{n}_{sn}(t) = \hat{\underline{n}}_n(t)\cos(\omega_n t) - \underline{n}_n(t)\sin(\omega_n t),
\end{aligned} \tag{A.24}$$

and

$$\begin{aligned}
E[\underline{n}_i(t)\underline{n}_n(t)] &= \frac{N_0}{2}\frac{1}{2\pi}\int_{-\infty}^{\infty} H_i(\omega)H_n^*(\omega)d\omega = E[\hat{\underline{n}}_i(t)\hat{\underline{n}}_n(t)], \\
E[\underline{n}_i(t)\hat{\underline{n}}_n(t)] &= \frac{N_0}{2}\frac{1}{2\pi}\int_{-\infty}^{\infty} H_i(\omega)H_n^*(\omega)[j\cdot sgn(\omega)]d\omega = -E[\hat{\underline{n}}_i(t)\underline{n}_n(t)].
\end{aligned} \tag{A.25}$$

The normalized complex cross-covariance is defined as

$$\rho_{in} = \frac{1}{2\sigma^2}\cdot E[(n_{ci}(T') + j\cdot n_{si}(T'))^*\cdot(n_{cn}(T') + j\cdot n_{sn}(T'))]. \tag{A.26}$$

Let

$$X \triangleq \Delta\omega_{in}T' = 2\pi(i-n)\Delta f((p-1)T + T_s) = (i-n)(p-1+r)2h\pi, \tag{A.27}$$

we can rewrite (A.26) as

$$\begin{aligned}
\rho_{in} = &\frac{1}{\sigma^2}\cdot\Big[\big(E[\underline{n}_i(T')\underline{n}_n(T')]\cos(X) - E[\underline{n}_i(T')\hat{\underline{n}}_n(T')]\sin(X)\big) \\
&+ j\cdot\big(E[\underline{n}_i(T')\underline{n}_n(T')]\sin(X) + E[\underline{n}_i(T')\hat{\underline{n}}_n(T')]\cos(X)\big)\Big].
\end{aligned} \tag{A.28}$$

Now let us find $E[\underline{n}_i(T')\underline{n}_n(T')]$ and $E[\underline{n}_i(T')\hat{\underline{n}}_n(T')]$ using (A.25). The filter transfer functions are

$$H_i(s) = \frac{2\pi W s}{s^2 + 2\pi W s + \omega_i^2} \simeq \frac{2\pi W s}{(s+\pi W)^2 + \omega_i^2}, \quad \omega_i \gg \pi W. \tag{A.29}$$

Then

$$\int_A^B H_i(\omega)H_n^*(\omega)d\omega \triangleq -j(2\pi W)^2 \int_{jA}^{jB} \frac{-s^2}{(s+a)(s+b)(s+c)(s+d)}ds, \tag{A.30}$$

where we define

$$\begin{Bmatrix} a \\ b \end{Bmatrix} \triangleq \pi W \pm j\omega_i, \quad \begin{Bmatrix} c \\ d \end{Bmatrix} \triangleq -\pi W \pm j\omega_n. \tag{A.31}$$

Then (A.30) can be rewritten as

$$\begin{aligned} \int_A^B H_i(\omega)H_n^*(\omega)d\omega = -j(\pi W)^2 \Bigg[& \frac{1}{2\pi W + j\cdot 2\pi\Delta f_{in}} \left(\log \frac{(jB+a)(jA+c)}{(jB+c)(jA+a)} \right) + \\ & \frac{1}{2\pi W - j\cdot 2\pi\Delta f_{in}} \left(\log \frac{(jB+b)(jA+d)}{(jB+d)(jA+b)} \right) \Bigg]. \end{aligned} \tag{A.32}$$

To simplify this, we use the assumption $f_i \gg W, \forall i$. Define

$$\begin{aligned} r &\triangleq \sqrt{\omega_i^2 + (\pi W)^2} \simeq \sqrt{\omega_n^2 + (\pi W)^2}, \\ \varepsilon &\triangleq \tan^{-1}\left(\frac{\pi W}{\omega_i}\right) \simeq \tan^{-1}\left(\frac{\pi W}{\omega_n}\right). \end{aligned} \tag{A.33}$$

where $\varepsilon \ll 1$. If we let $A = 0$ and $B \to \infty$, we obtain

$$\begin{aligned}
&\int_0^\infty H_i(\omega)H_j^*(\omega)d\omega \\
=&\lim_{B\to\infty} -j(\pi W)^2\left[\frac{1}{2\pi W + j\cdot 2\pi\Delta f_{in}}\left(\log\frac{c(jB+a)}{a(jB+c)}\right)+\right. \\
&\qquad\left.\frac{1}{2\pi W - j\cdot 2\pi\Delta f_{in}}\left(\log\frac{d(jB+b)}{b(jB+d)}\right)\right] \\
=&-j(\pi W)^2\left[\frac{1}{2\pi W + j\cdot 2\pi\Delta f_{in}}\left(\log\frac{(-\omega_j - j\pi W)}{(-\omega_i + j\pi W)}\right)+\right. \\
&\qquad\left.\frac{1}{2\pi W - j\cdot 2\pi\Delta f_{in}}\left(\log\frac{(\omega_j - j\pi W)}{(\omega_i + j\pi W)}\right)\right] \\
\simeq&-j(\pi W)^2\left[\frac{1}{2\pi W + j\cdot 2\pi\Delta f_{in}}\left(\log\frac{re^{j(\pi+\varepsilon)}}{re^{j(\pi-\varepsilon)}}\right)+\frac{1}{2\pi W - j\cdot 2\pi\Delta f_{in}}\left(\log\frac{re^{j(2\pi-\varepsilon)}}{re^{j\varepsilon}}\right)\right] \\
\simeq&-j(\pi W)^2\left[\frac{1}{2\pi W + j\cdot 2\pi\Delta f_{in}}\cdot 0+\frac{1}{2\pi W - j\cdot 2\pi\Delta f_{in}}\cdot(j2\pi)\right] \\
=&\frac{(\pi W)^2}{W - j\cdot\Delta f_{in}}.
\end{aligned} \tag{A.34}$$

where the approximations on the 3^{rd} and 4^{th} lines of the derivation follow from (A.33). Similarly, if we let $A \to -\infty$ and $B = 0$, we have

$$\int_{-\infty}^0 H_i(\omega)H_j^*(\omega)d\omega \simeq \frac{(\pi W)^2}{W + j\cdot\Delta f_{in}}. \tag{A.35}$$

Substituting (A.34) and (A.35) in (A.25), we get

$$\begin{aligned}
E[\underline{n}_i(T')\underline{n}_n(T')] &= \frac{N_0}{2}\cdot\frac{1}{2\pi}\cdot\frac{2W(\pi W)^2}{W^2+(\Delta f_{in})^2} = \frac{N_0}{2}\cdot\pi W\cdot\frac{W^2}{W^2+(\Delta f_{in})^2}, \\
E[\underline{n}_i(T')\hat{\underline{n}}_n(T')] &= \frac{N_0}{2}\cdot\frac{1}{2\pi}\cdot\frac{-2\Delta f_{in}(\pi W)^2}{W^2+(\Delta f_{in})^2} = \frac{N_0}{2}\cdot\pi W\cdot\frac{-W\Delta f_{in}}{W^2+(\Delta f_{in})^2}.
\end{aligned} \tag{A.36}$$

Recall from (A.23) that $\sigma^2 = \frac{N_0}{2} \cdot \pi W$. Finally, we simplify (A.28) as

$$\begin{aligned}\rho_{in} = \frac{1}{\sigma^2} \cdot \big[&\big(E[\underline{n}_i(T')\underline{n}_n(T')]\cos(X) - E[\underline{n}_i(T')\hat{\underline{n}}_n(T')]\sin(X)\big) \\ &+ j \cdot \big(E[\underline{n}_i(T')\underline{n}_n(T')]\sin(X) + E[\underline{n}_i(T')\hat{\underline{n}}_n(T')]\cos(X)\big)\big] \\ = \frac{W(W\cos(X) + \Delta f_{in}\sin(X))}{W^2 + (\Delta f_{in})^2} &+ j \cdot \frac{W(W\sin(X) - \Delta f_{in}\cos(X))}{W^2 + (\Delta f_{in})^2}.\end{aligned} \tag{A.37}$$

Thus,

$$\begin{aligned}|\rho_{in}| &= \frac{W}{\sqrt{W^2 + (\Delta f_{in})^2}} = \frac{z}{\sqrt{z^2 + ((i-n)h)^2}}, \\ \phi_{in} = \angle\rho_{in} &= \tan^{-1}\left[\frac{W\sin(X) - \Delta f_{in}\cos(X)}{W\cos(X) + \Delta f_{in}\sin(X)}\right] = \tan^{-1}\left[\frac{z\sin(X) - (i-n)h\cos(X)}{z\cos(X) + (i-n)h\sin(X)}\right].\end{aligned} \tag{A.38}$$

where we use the four-quadrant definition for $\tan^{-1}$ and $X = (i-n)(p-1+r)2h\pi$ was defined in (A.27). Notice that both terms in (A.38) are independent of the pulse duration T. While $|\rho_{in}|$ is independent of pulse index p, ϕ_{in} is dependent on p. It can be shown that the dependence will cancel out the phase terms in (A.21), making the final results of (2.18) independent of p.

Appendix B

Orthogonal signaling

B.1 MFSK

With orthogonal signaling and sampling at the end of each pulse, the parameters in (A.21) can be simplified as

$$
\begin{aligned}
A_1 &= \sqrt{(m_{ii}(T_s)+m_{mi}(T+T_s))^2+(\mu_{ii}(T_s)+\mu_{mi}(T+T_s))^2},\\
A_2 &= \sqrt{(m_{in}(T_s)+m_{mn}(T+T_s))^2+(\mu_{in}(T_s)+\mu_{mn}(T+T_s))^2},\\
\theta_1 &= \tan^{-1}\left[\frac{\mu_{ii}(T_s)+\mu_{mi}(T+T_s)}{m_{ii}(T_s)+m_{mi}(T+T_s)}\right],\\
\theta_2 &= \tan^{-1}\left[\frac{\mu_{in}(T_s)+\mu_{mn}(T+T_s)}{m_{in}(T_s)+m_{mn}(T+T_s)}\right].
\end{aligned}
\tag{B.1}
$$

From (A.12) $\sim$ (C.5), with $h \in \mathbb{I}^+$ and $r = 1$, we have

$$
\begin{aligned}
&m_{in}(T_s) = \frac{Az^2(1-e^{-\pi z})}{(2(i-n)h)^2+z^2}, \quad m_{ii}(T_s) = A(1-e^{-\pi z}),\\
&\mu_{in}(T_s) = \frac{Az(-2h(i-n))(1-e^{-\pi zr})}{(2(i-n)h)^2+z^2}, \quad \mu_{ii}(T_s) = 0,\\
&m_{mn}(T+T_s) = \frac{Az^2e^{-\pi z}(1-e^{-\pi z})}{(2(m-n)h)^2+z^2}, \quad m_{mi}(T+T_s) = \frac{Az^2e^{-\pi z}(1-e^{-\pi z})}{(2(m-i)h)^2+z^2},\\
&\mu_{mn}(T+T_s) = \frac{Az(-2h(m-n))e^{-\pi z}(1-e^{-\pi z})}{(2(m-n)h)^2+z^2}, \quad \mu_{mi}(T+T_s) = \frac{Az(-2h(m-i))e^{-\pi z}(1-e^{-\pi z})}{(2(m-i)h)^2+z^2}.
\end{aligned}
\tag{B.2}
$$

Simplifying (A.23) and (A.38) yields

$$
\sigma^2 = \frac{N_0\pi W}{2} = \frac{N_0\pi z}{2T}, \quad |\rho_{in}| = \frac{z}{\sqrt{z^2+((i-n)h)^2}}, \quad \phi_{in} = \tan^{-1}\left[\frac{-(i-n)h}{z}\right]. \tag{B.3}
$$

B.2 BFSK

Letting $i = 1, n = 2, m = 1$ in (B.1) $\sim$ (B.3), we have

$$
\begin{aligned}
&A_1 = A(1-e^{-2\pi z}), \quad A_2 = A(1-e^{-2\pi z})\sqrt{\frac{z^2}{4h^2+z^2}},\\
&\theta_1 = 0, \quad \theta_2 = \tan^{-1}\left[\frac{2h}{z}\right],\\
&\sigma^2 = \frac{N_0\pi z}{2T}, \quad \rho_{12} = \frac{z}{\sqrt{z^2+h^2}}, \quad \phi_{12} = \tan\left[\frac{h}{z}\right].
\end{aligned}
\tag{B.4}
$$

Then, pluging (B.4) in (2.18), we obtain

$$
\begin{Bmatrix} a_{12}^1 \\ b_{12}^1 \end{Bmatrix} = \frac{E_b}{N_0} \cdot \frac{2(1-e^{-2\pi z})^2 \cdot (\sqrt{h^2+z^2} \mp h)^2}{\pi z(4h^2+z^2)}, \tag{B.5}
$$

where the bit energy is $E_b = A^2T/2$. Similarly, leting $i = 1, n = 2$ and $m = 2$ and following the same procedure, we obtain

$$\begin{Bmatrix} a_{12}^2 \\ b_{12}^2 \end{Bmatrix} = \frac{E_b}{N_0} \cdot \frac{2(1-e^{-\pi z})^2}{\pi z(4h^2+z^2)} \cdot \{[\sqrt{h^2+z^2}(1+e^{-\pi z}) \mp h(1-e^{-\pi z})]^2 - \frac{16h^2z^2e^{-\pi z}}{4h^2+z^2}\}. \quad \text{(B.6)}$$

Appendix C

FFH-MFSK system with 2-pole BPF detection

We use the union bound and, thus do pairwise comparison. The block diagram is shown in Fig. 4.1, where, as discussed in more detail in Appendix A, the output of the i^{th} filter can be expressed in terms of the in-phase and quadrature components as

$$\underline{x}_i(t) = [a_i(t) + \underline{n}_{ci}(t)]\cos\omega_i t - [b_i(t) + \underline{n}_{si}(t)]\sin\omega_i t, \tag{C.1}$$

where $a_i(t)$ and $b_i(t)$ are the in-phase and quadrature parts of the output signal, respectively, as will be defined in (C.3) and (C.5), $\underline{n}_{ci}(t)$ and $\underline{n}_{si}(t)$ are the in-phase and quadrature parts of the output noise, respectively, and we sample at $T_c, \ldots, LT_c$. Without loss of generality, we assume "i" is transmitted and "n" is the ICI branch. Thus, after the square law detector and summation, both the i^{th} and the n^{th} branch are the sum of $2L$ correlated non-central chi-square random variables, with different non-centrality parameters. We take the difference to form a new random variable, which is a linear combination of $4L$ correlated non-central chi-square random variables. Let X be

a multi-normal random vector defined as

$$X = \begin{bmatrix} X_{11} \\ \vdots \\ X_{1L} \\ X_{21} \\ \vdots \\ X_{2L} \\ Y_{11} \\ \vdots \\ Y_{1L} \\ Y_{21} \\ \vdots \\ Y_{2L} \end{bmatrix} \triangleq \begin{bmatrix} a_i(T_c) + \underline{n}_{ci}(T_c) \\ \vdots \\ a_i(LT_c) + \underline{n}_{ci}(LT_c) \\ b_i(T_c) + \underline{n}_{si}(T_c) \\ \vdots \\ b_i(LT_c) + \underline{n}_{si}(LT_c) \\ a_n(T_c) + \underline{n}_{cn}(T_c) \\ \vdots \\ a_n(LT_c) + \underline{n}_{cn}(LT_c) \\ b_n(T_c) + \underline{n}_{sn}(T_c) \\ \vdots \\ b_n(LT_c) + \underline{n}_{sn}(LT_c) \end{bmatrix} \triangleq \mu + X_0. \tag{C.2}$$

We compute the mean and covariance matrix of X, i.e., $\mu = E[X]$ and $\Sigma = Cov(X)$. It was shown in [34] that only the adjacent hop gives significant ISI, so that only the first hop of each symbol experiences ISI from the previous symbol, while all other hops experience ISI from the previous hop of the current symbol. From Appendix B of [34], given that the current symbol is "i", the ICI branch is "n" and the previous symbol is "m", we have, for the first hop,

$$\mu_a = \begin{bmatrix} a_i(T_c) \\ b_i(T_c) \\ a_n(T_c) \\ b_n(T_c) \end{bmatrix} = A \begin{bmatrix} m_{ii} & -\mu_{ii} & m'_{mi} \\ \mu_{ii} & m_{ii} & \mu'_{mi} \\ m_{in} & -\mu_{in} & m'_{mn} \\ \mu_{in} & m_{in} & \mu'_{mn} \end{bmatrix} \begin{bmatrix} \cos\theta_1 \\ \sin\theta_1 \\ 1 \end{bmatrix} \tag{C.3}$$

where

$$
\begin{aligned}
m_{in} &= \frac{z^2(1-e^{-\pi z})}{(2(i-n))^2+z^2}, \\
\mu_{in} &= \frac{z(-2(i-n))(1-e^{-\pi z})}{(2(i-n))^2+z^2}, \\
m'_{mn} &= \frac{z^2 e^{-\pi z}(1-e^{-\pi z})}{(2(m-n))^2+z^2}, \\
\mu'_{mn} &= \frac{z(-2(m-n))e^{-\pi z}(1-e^{-\pi z})}{(2(m-n))^2+z^2}.
\end{aligned}
\tag{C.4}
$$

Note that the terms in (C.4) are very similar to the corresponding parameters in Appendix B of [34], and θ_1 is the difference between the phase of the first hop of the current symbol and the last hop of the previous symbol. Let $\theta'_1, \theta'_2, \ldots, \theta'_L$ denote the random phases associated with each hop of the current symbol, and let θ'_0 denote the random phase associated with the last hop of the previous symbol. We define $\theta_i \triangleq \theta'_i - \theta'_{i-1}, 1 \leqslant i \leqslant L$. Then for all other hops, we have

$$
\mu_b = \begin{bmatrix} a_i(2T_c) & \ldots & a_i(LT_c) \\ b_i(2T_c) & \ldots & b_i(LT_c) \\ a_n(2T_c) & \ldots & a_n(LT_c) \\ b_n(2T_c) & \ldots & b_n(LT_c) \end{bmatrix} = A \begin{bmatrix} m_{ii} & -\mu_{ii} & m'_{ii} \\ \mu_{ii} & m_{ii} & \mu'_{ii} \\ m_{in} & -\mu_{in} & m'_{in} \\ \mu_{in} & m_{in} & \mu'_{in} \end{bmatrix} \begin{bmatrix} \cos\theta_2 & \ldots & \cos\theta_L \\ \sin\theta_2 & \ldots & \sin\theta_L \\ 1 & \ldots & 1 \end{bmatrix}, \tag{C.5}
$$

and thus

$$
\mu' \triangleq \begin{bmatrix} \mu_a & \mu_b \end{bmatrix} = \begin{bmatrix} a_i(T_c) & \ldots & a_i(LT_c) \\ b_i(T_c) & \ldots & b_i(LT_c) \\ a_n(T_c) & \ldots & a_n(LT_c) \\ b_n(T_c) & \ldots & b_n(LT_c) \end{bmatrix} \tag{C.6}
$$

which can be easily reshaped to μ in the form of a column vector.

Representing the in-phase and quadrature components of filtered noise of the i^{th} branch

using Hilbert transforms gives [15]

$$\begin{aligned} \underline{n}_{ci}(t) &= \underline{n}_i(t)\cos(\omega_i t) + \hat{\underline{n}}_i(t)\sin(\omega_i t), \\ \underline{n}_{si}(t) &= \hat{\underline{n}}_i(t)\cos(\omega_i t) - \underline{n}_i(t)\sin(\omega_i t). \end{aligned} \tag{C.7}$$

Since we use orthogonal signaling and sample at the end of each hop, (C.7) can be simplified to

$$\underline{n}_{ci}(kT_c) = \underline{n}_i(kT_c), \quad \underline{n}_{si}(kT_c) = \hat{\underline{n}}_i(kT_c), \quad k \in \mathbb{I}. \tag{C.8}$$

The covariance matrix Σ can be represented as

$$\Sigma = Cov(X) = Cov(X_0) = \begin{bmatrix} A & 0 & B & C \\ 0 & A & -C & B \\ B & -C & A & 0 \\ C & B & 0 & A \end{bmatrix} \tag{C.9}$$

where A, B, C are $L \times L$ matrices with the $(x,y)^{th}$ element, respectively,

$$\begin{aligned} A_{xy} &= R_{ci}(|x-y|T_c), \\ B_{xy} &= R_{ci,cn}(|x-y|T_c), \\ C_{xy} &= R_{ci,sn}(|x-y|T_c), \end{aligned} \tag{C.10}$$

and 0 is the $L \times L$ all zero matrix. The diagonal terms in A, B and C can be found using the same

technique described in Appendix A of [34] as

$$\begin{aligned} R_{ci}(0) &= E[\underline{n}_{ci}^2(T_c)] = \frac{\eta_0 \pi z}{2T_c}, \\ R_{ci,cn}(0) &= E[\underline{n}_{ci}(T_c)\underline{n}_{cn}(T_c)] = \frac{\eta_0 \pi z}{2T_c} \cdot \frac{z^2}{z^2+(i-n)^2}, \\ R_{ci,sn}(0) &= E[\underline{n}_{ci}(T_c)\underline{n}_{sn}(T_c)] = \frac{\eta_0 \pi z}{2T_c} \cdot \frac{-(i-n)z}{z^2+(i-n)^2}. \end{aligned} \tag{C.11}$$

For the non-diagonal terms, we have the following relationship:

$$\frac{R_{ci}(xT_c)}{R_{ci}(0)} = \frac{R_{ci,cn}(xT_c)}{R_{ci,cn}(0)} = \frac{R_{ci,sn}(xT_c)}{R_{ci,sn}(0)} = e^{-\pi z \cdot x}, \tag{C.12}$$

where x is a non-negative integer. The impulse response of the i^{th} filter is

$$h_i(t) = \frac{2\pi z}{T_c} e^{-\pi z \cdot t/T_c} \cos(\omega_i t) u(t). \tag{C.13}$$

Letting $x \triangleq t/T_c$, then

$$\begin{aligned} h_i(t+xT_c) &= \frac{2\pi z}{T_c} e^{-\pi z \cdot (t+xT_c)/T_c} \cos(\omega_i (t+xT_c)) u(t+xT_c) \\ &= e^{-\pi z \cdot x} \cdot \frac{2\pi z}{T_c} e^{-\pi z \cdot t/T_c} \cos(\omega_i t) u(t+xT_c), \quad x \in \mathbb{I}. \end{aligned} \tag{C.14}$$

From (C.8),

$$\begin{aligned} R_{ci,cn}(0) &= E[\underline{n}_{ci}(T_c)\underline{n}_{cn}(T_c)] = E[\underline{n}_{si}(T_c)\underline{n}_{sn}(T_c)] \\ &= E[\underline{n}_i(T_c)\underline{n}_n(T_c)] = \frac{\eta_0}{2} \cdot h_i(t) * h_n(-t)\Big|_{t=0} \end{aligned} \tag{C.15}$$

Similarly, for a non-negative integer x,

$$\begin{aligned} R_{ci,cn}(xT_c) &= E[\underline{n}_{ci}(T_c)\underline{n}_{cn}((x+1)T_c)] = E[\underline{n}_{si}(T_c)\underline{n}_{sn}((x+1)T_c)] \\ &= E[\underline{n}_i(T_c)\underline{n}_n((x+1)T_c)] = \frac{\eta_0}{2} \cdot h_i(t+xT_c) * h_n(-t)\Big|_{t=0} \end{aligned} \tag{C.16}$$

Now (C.16) can be rewritten as

$$\begin{aligned} R_{ci,cn}(xT_c) &= \frac{\eta_0}{2} \cdot h_i(t+xT_c) * h_n(-t)\Big|_{t=0} \\ &= \frac{\eta_0}{2} \cdot \int_{-\infty}^{\infty} h_i(\tau+xT_c) \cdot h_n(\tau) d\tau \\ &= \frac{\eta_0}{2} \int_{-\infty}^{\infty} e^{-\pi z \cdot x} \cdot \frac{2\pi z}{T_c} e^{-\pi z \cdot \tau / T_c} \cos(\omega_i \tau) u(\tau) \\ &\qquad \cdot \frac{2\pi z}{T_c} e^{-\pi z \cdot \tau / T_c} \cos(\omega_n t) u(\tau) d\tau \\ &= \frac{\eta_0}{2} \cdot e^{-\pi z \cdot x} \cdot \int_{-\infty}^{\infty} h_i(\tau) \cdot h_n(\tau) d\tau = e^{-\pi z \cdot x} R_{ci,cn}(0). \end{aligned} \tag{C.17}$$

With μ and Σ, we can numerically find the pdf of $Q(X)$, defined in (3.4), using characteristic functions. The probability of error, where i is sent but n is detected, and where m is the previous symbol, conditioned on the set of random phases, $\theta_1, \ldots, \theta_L$ is given by

$$Ps(i,n,m,\theta_1,\ldots,\theta_L) = Pr(Q(X) < 0). \tag{C.18}$$

Then finally, the conditional SER, Ps_{in}^{m}, is found by averaging over the L random phases.

Appendix D

FFH-MFSK system with diversity

We again use the block diagram shown in Fig. 3.1. The only difference now is that the input hops have i.i.d. amplitudes, that is,

$$S(t) = \sum_{l=1}^{\infty} \underline{R}_l P_{\frac{T_c}{2}}(t-(l-1)T_c - \frac{T_c}{2}) \cos(2\pi f^{(l)}[t-(l-1)T_c] + \underline{\theta}_l), \tag{D.1}$$

where $\underline{R}_l$ are i.i.d. Rician distributed. As in Appendix D, we compute in this appendix the mean and covariance matrix of the test statistic X, i.e., $\mu = E[X]$ and $\Sigma = Cov(X)$.

D.1 Matched filter detection

Let $R_1, \ldots, R_L$ denote the amplitude of the $1^{st}, \ldots, L^{th}$ hop, respectively, of the current symbol. For matched filter detection, since there is no ISI or ICI, the parameters are

$$\mu = \begin{bmatrix} R_1 & R_2 & \ldots & R_L & 0_{3L} \end{bmatrix}^T, \quad \Sigma = \frac{N_0}{T_c} I_{4L}, \tag{D.2}$$

where 0_{3L} is the $3L \times 1$ zero column vector and I_{4L} is the $4L \times 4L$ identity matrix. After a simple normalization, the parameters are equivalent to

$$\mu = \left[\begin{array}{cccc} \sqrt{\frac{2\gamma_1}{L}} & \sqrt{\frac{2\gamma_2}{L}} & \dots & \sqrt{\frac{2\gamma_L}{L}} \quad 0_{3L} \end{array} \right]^T, \quad \Sigma = I_{4L}, \tag{D.3}$$

where $\gamma_i = \left(\frac{E_b}{N_0}\right)_i = \left(\frac{LE_c}{N_0}\right)_i = \frac{LR_i^2 T_c}{2N_0}$ and the pdf of $\gamma_i, f(\gamma_i)$, was defined in (2.31).

Similar to Appendix D, with μ and Σ, we can numerically find the probability of error, conditioned on the set of instantaneous E_b/N_J, $\gamma_1, \dots, \gamma_L$, denoted as $Ps(\gamma_1, \dots, \gamma_L)$. Then,

$$P_b = \frac{M}{2M-2} \int_0^\infty \cdots \int_0^\infty Ps(\gamma_1, \dots, \gamma_L) \prod_{i=1}^{L} f(\gamma_i) d\gamma_1 \dots d\gamma_L. \tag{D.4}$$

D.2 2-pole BPF detection

Interleaving has no effect on the noise components, so we retain the same Σ as in Appendix D. Let $\underline{R}_0$ denote the amplitude of the last hop of the previous symbol, and $\underline{R}_1, \dots, \underline{R}_L$ denote the amplitude of the $1^{st}, \dots, L^{th}$ hop of the current symbol, respectively. The construction of the mean vector μ is similar to that in Appendix D – just replace the constant amplitude A is by Rician distributed amplitudes $R_0, R_1, \dots, R_L$. Similar to Appendix D, with μ and Σ, we can numerically find the probability of error, where i is sent but n is detected and m is the previous symbol, conditioned on the set of random phases $\theta_1, \dots, \theta_L$, and the set of instantaneous E_b/N_J, $\gamma_0, \dots, \gamma_L$, denoted as $Ps(i, n, m, \theta_1, \dots, \theta_L, \gamma_0, \dots, \gamma_L)$. Then finally, the conditional probability of error can be represented by the following integral:

$$Ps_{in}^m = \frac{1}{(2\pi)^L} \int_0^\infty \cdots \int_0^\infty \int_0^{2\pi} \cdots \int_0^{2\pi} Ps(i, n, m, \theta_1, \dots, \theta_L, \gamma_0, \dots, \gamma_L) \cdot \prod_{i=0}^{L} f(\gamma_i) d\theta_1 \dots d\theta_L d\gamma_0 \dots d\gamma_L. \tag{D.5}$$

To find the union bound on average SER, we average over i and m, and sum over n.

Appendix E

FFH-MFSK-MF system under PBJ

E.1 Non-fading channels

Taking the derivative of $P_s(\rho)$ defined in equation (10) of [43] with respect to ρ yields

$$\begin{aligned} P_s'(\rho) \triangleq & 1 - \int_0^{\infty} \Big(1 - e^{-v} \sum_{k=0}^{L-1} \frac{v^k}{k!}\Big)^{M-1} \Big(\frac{v}{y}\Big)^{\frac{L-1}{2}} e^{-(y+v)} \\ & \cdot \Big[\frac{\sqrt{vy}}{2}\Big(I_{L-2}(2\sqrt{vy}) + I_L(2\sqrt{vy})\Big) - \Big(\frac{L-3}{2} + y\Big) I_{L-1}(2\sqrt{vy})\Big] dv, \end{aligned} \tag{E.1}$$

where $y \triangleq \rho\gamma = \rho(\log_2 M)\frac{E_b}{N_J}$, and the derivative of the modified Bessel function of the first kind, n^{th} order, is given by $I_n'(x) = \frac{1}{2}[I_{n-1}(x) + I_{n+1}(x)]$. Let y_0 be the value of y resulting in $P_s'(\rho) = 0$. It is known that when E_b/N_J is sufficiently small, full-band jamming is optimal. Let γ_0 be the threshold so that when $E_b/N_J < \gamma_0$, full-band jamming is optimal. Then γ_0 is found by setting $\rho = 1$, and thus $\gamma_0 = \frac{y_0}{\log_2 M}$. Finally, plugging $y = y_0$ in (E.1) yields

$$\begin{aligned} P_{s,worst} &= \frac{1}{E_b/N_J} \cdot \frac{y_0}{\log_2 M} \Big[1 - \int_0^{\infty} \Big(1 - e^{-v} \sum_{k=0}^{L-1} \frac{v^k}{k!}\Big)^{M-1} \cdot \Big(\frac{v}{y_0}\Big)^{\frac{L-1}{2}} e^{-(y_0+v)} I_{L-1}(2\sqrt{y_0 v}) dv\Big] \\ &\triangleq \frac{\beta}{E_b/N_J}. \end{aligned} \tag{E.2}$$

The worst-case bit error rate can be expressed as $P_{b,worst} = \frac{\beta_b}{E_b/N_J}$, where $\beta_b \triangleq \frac{\beta M}{2M-2}$.

E.2 Slow, flat, Rician fading channel

Taking the derivative of $P_s(\rho)$ defined in equation (13) of [43] with respect to ρ yields

$$\begin{aligned} P_s'(\rho) &= 1 - \int_0^\infty \int_0^\infty \frac{(1+K)e^{-K}}{\bar{\gamma}} \cdot \frac{\partial}{\partial \rho}\left[e^{-\frac{(1+K)\gamma}{\rho\bar{\gamma}}} I_0\left(\sqrt{4K(1+K)\frac{\gamma}{\rho\bar{\gamma}}}\right)\right] \\ &\quad \cdot \left(1 - e^{-v}\sum_{k=0}^{L-1}\frac{v^k}{k!}\right)^{M-1}\left(\frac{v}{\gamma}\right)^{\frac{L-1}{2}} e^{-(\gamma+v)} I_{L-1}(2\sqrt{\gamma v})\,dv\,d\gamma \\ &\triangleq 1 - ye^{-K} \cdot \int_0^\infty \int_0^\infty e^{-y\gamma}\left[y\gamma I_0\left(\sqrt{4Ky\gamma}\right) - \sqrt{Ky\gamma} I_1\left(\sqrt{4Ky\gamma}\right)\right] \\ &\quad \cdot \left(1 - e^{-v}\sum_{k=0}^{L-1}\frac{v^k}{k!}\right)^{M-1}\left(\frac{v}{\gamma}\right)^{\frac{L-1}{2}} e^{-(\gamma+v)} I_{L-1}(2\sqrt{\gamma v})\,dv\,d\gamma, \end{aligned} \tag{E.3}$$

where $y \triangleq \frac{1+K}{\rho\bar{\gamma}}$. Let y_0 be the value of y resulting in $P_s'(\rho) = 0$. Then γ_0 is found by setting $\rho = 1$, and thus $\gamma_0 = \frac{1+K}{y_0 \log_2 M}$ is the threshold for partial-band jamming as the optimal strategy, i.e., when $E_b/N_J < \gamma_0$, full-band jamming is optimal. The worst case SER is given by

$$\begin{aligned} P_{s,worst} &= \frac{1}{\bar{\gamma}} \cdot \frac{1+K}{y_0 M \log_2 M}\left[1 - y_0 e^{-K}\int_0^\infty \int_0^\infty e^{-y_0\gamma} \cdot I_0\left(\sqrt{4Ky_0\gamma}\right)\left(1 - e^{-v}\sum_{k=0}^{L-1}\frac{v^k}{k!}\right)^{M-1}\right. \\ &\quad \left. \cdot \left(\frac{v}{\gamma}\right)^{\frac{L-1}{2}} e^{-(\gamma+v)} I_{L-1}(2\sqrt{\gamma v})\,dv\,d\gamma\right] \triangleq \frac{\beta}{\bar{\gamma}}. \end{aligned} \tag{E.4}$$

The worst-case BER can be expressed as $P_{b,worst} = \frac{\beta_b}{E_b/N_J}$, where $\beta_b \triangleq \frac{\beta M}{2M-2}$.

Appendix F

FFH-MFSK-MF system under MTJ

F.1 Non-fading channels

Let R_c be the hop rate, R_b be the bit rate, $R_s = R_b/\log_2 M$ be the symbol rate and N_t be the total number of slots. Then the total spread spectrum bandwidth is given by $W_{ss} = N_t R_s$. Letting J be the total jamming power, Q be the number of jamming tones, and S be the signal power, we have $E_b = S/R_b$ as the energy per bit, $\eta_J = J/W_{ss}$ as the power spectral density of the jammer, and finally we define $\alpha \triangleq \frac{S}{J/Q}$ as the SJR.

For each hop, the probability that the M-ary band containing the keyed tone is jammed is

$$\mu' = \frac{QM}{N_t} = \frac{\alpha M}{\log_2 M \times \frac{E_b}{\eta_J}}. \tag{F.1}$$

When E_b/η_J is large, μ' is small and the probability that multiple hops of the M-ary band with the keyed tone are jammed is orders of magnitude smaller, so we can assume that, at most, one hop of the M-ary bad with the keyed tone is jammed at large E_b/η_J. Therefore, the probability

that any hop of the M-ary band with the keyed tone is jammed is

$$\mu \approx L\mu' = \frac{\alpha LM}{\log_2 M \times \frac{E_b}{\eta_J}}. \tag{F.2}$$

A symbol error occurs when a hop of the M-ary band with the keyed tone is jammed in an unkeyed slot, and $\frac{1}{\alpha} > L \Rightarrow \alpha < \frac{1}{L}$. Thus, the bit error rate is

$$\begin{aligned} P_b &= \frac{M}{2(M-1)} P_s \\ &= \frac{M}{2(M-1)} \cdot \frac{M-1}{M} \cdot \mu \\ &= \frac{M}{2(M-1)} \cdot \frac{M-1}{M} \cdot \frac{\alpha LM}{\log_2 M \times \frac{E_b}{\eta_J}} \\ &= \frac{\alpha LM}{2\log_2 M \cdot \frac{E_b}{\eta_J}}. \end{aligned} \tag{F.3}$$

Obviously, the worst case performance is achieved by maximizing α under the constraints $\alpha < 1/L$ and $\mu \leqslant 1$:

$$\alpha < \frac{1}{L}, \alpha \leqslant \frac{\log_2 M E_b/\eta_J}{LM}. \tag{F.4}$$

Therefore,

$$\alpha_{wc} = \begin{cases} \frac{\log_2 M}{LM} \cdot \frac{E_b}{\eta_J}, & \frac{E_b}{\eta_J} < \frac{M}{\log_2 M} \\ \frac{1}{L} -, & \frac{E_b}{\eta_J} \geqslant \frac{M}{\log_2 M} \end{cases} \tag{F.5}$$

and let $\alpha = \alpha_{wc}$ in (F.3), we find the worst-case BER as

$$P_{b,wc} = \begin{cases} \frac{1}{2}, & \frac{E_b}{\eta_J} \leqslant \frac{M}{\log_2 M} \\ \frac{M}{2\log_2 M} \cdot \frac{1}{E_b/\eta_J}, & \frac{E_b}{\eta_J} \geqslant \frac{M}{\log_2 M} \end{cases} \tag{F.6}$$

This happens to be the same as the SFH case analyzed in [41]. Note that $P_{b,wc}$ increases with M since the key parameter, μ, increases with M.

F.2 Slow, flat Rician fading channels

In a Rician fading channel, let Ω_s and Ω_j be the total power of the signal and jamming power per jammed slot, respectively, and denote $\alpha_r \triangleq \Omega_s/\Omega_j$ as the SJR. Then, at large E_b/η_J, the probability that any hop of the M-ary band with the keyed tone is jammed is roughly

$$\mu_r \approx \frac{\alpha_r LM}{\log_2 M \frac{E_b}{\eta_J}}. \tag{F.7}$$

The BER as a function of α_r is given by

$$\begin{aligned} P_b &= \frac{M}{2(M-1)} \cdot \frac{M-1}{M} \cdot \mu_r \cdot \int_0^\infty \int_0^\infty u(r_j^2 - Lr_s^2) f(r_s) f(r_j) dr_s dr_j \\ &= \frac{\alpha_r LM}{2\log_2 M \frac{E_b}{\eta_J}} \int_0^\infty \int_0^\infty u(r_j^2 - Lr_s^2) f(r_s) f(r_j) dr_s dr_j, \end{aligned} \tag{F.8}$$

where $f(r_s)$ was defined in (3.19) and $f(r_j)$ follows in a similar manner. If we let

$$c = \alpha_r L, \quad x = \frac{r_s}{\sqrt{\Omega_s}}, \quad y = r_j \frac{\sqrt{\alpha}_r}{\sqrt{\Omega_s}}, \tag{F.9}$$

then

$$\begin{aligned} P_b =& \frac{cM}{2\log_2 M \frac{E_b}{\eta_J}} \int_0^\infty \int_0^\infty u(r_j^2 - Lr_s^2) \frac{2(K_s+1)r_s}{\Omega_s} \cdot e^{-K_s - \frac{(K_s+1)r_s^2}{\Omega_s}} I_0\left(2\sqrt{\frac{K_s(K_s+1)}{\Omega_s}} r_s\right) \\ & \cdot \frac{2(K_j+1)r_j}{\Omega_j} e^{-K_j - \frac{(K_j+1)r_j^2}{\Omega_j}} I_0\left(2\sqrt{\frac{K_j(K_j+1)}{\Omega_j}} r_j\right) dr_s dr_j \\ =& \frac{cM}{2\log_2 M \frac{E_b}{\eta_J}} \int_0^\infty \int_{x\sqrt{c}}^\infty h(x, K_s) h(y, K_j) dy dx \\ \triangleq& \frac{G(c)}{E_b/\eta_J}, \end{aligned} \tag{F.10}$$

where $h(r,K)$ was defined in (3.16).

F.3 Signal experiences slow, flat Rayleigh fading

For $K_s = 0$, $G(c)$ in (F.10) is monotonically increasing, for all K_j. Therefore, the jammer would use the largest permissible c. The constraint on c is

$$\mu_r = \frac{cM}{\log_2 M \times \frac{E_b}{\eta_J}} \leqslant 1 \Rightarrow c \leqslant \frac{\log_2 M \times \frac{E_b}{\eta_J}}{M}, \tag{F.11}$$

and thus the worst-case BER is given by letting $c = \frac{\log_2 M \times \frac{E_b}{\eta_J}}{M}$ in (F.10)

$$P_{b,wc} = \frac{1}{2} \int_0^\infty \int_{x\sqrt{\frac{\log_2 M \times \frac{E_b}{\eta_J}}{M}}}^\infty h(x, K_s) h(y, K_j) dy dx. \tag{F.12}$$

On the other hand, the worst-case BER is also

$$P_{b,wc} = \frac{G\left(\frac{\log_2 M \times \frac{E_b}{\eta_J}}{M}\right)}{E_b/\eta_J}. \tag{F.13}$$

Since it can be shown that, for any K_j, $\lim_{c\to\infty} G(c) = 1$, we have the asymptotic performance

$$\lim_{E_b/\eta_J \to \infty} P_{b,wc} = \frac{1}{E_b/\eta_J}. \tag{F.14}$$

Appendix G

FFH-MFSK-2pole system under MTJ in a non-fading channel

We consider two conditional SER: when the jammed hop is the last one (with probability $\frac{1}{L}$), denoted by P_1, and when the jammed hop is not the last one (with probability $\frac{L-1}{L}$), denoted by P_2, and thus the average SER is given by (3.18).

First consider the case that the last (L^{th}) hop is jammed. The filter output of the jamming waveform in terms of the in-phase and quadrature components is, for the L^{th} hop,

$$\mu_{aJ} = r_j \begin{bmatrix} m_{ni} & -\mu_{ni} \\ \mu_{ni} & m_{ni} \\ m_{nn} & -\mu_{nn} \\ \mu_{nn} & m_{nn} \end{bmatrix} \begin{bmatrix} \cos\theta_J \\ \sin\theta_J \end{bmatrix}, \tag{G.1}$$

and zero for all other hops, where r_j is the amplitude of the jamming waveform. Thus the filter output of the signal plus jamming waveform is

$$\mu_1' = \begin{bmatrix} \mu_a & \mu_b \end{bmatrix} + \begin{bmatrix} 0_{4\times(L-1)} & \mu_{aJ} \end{bmatrix}, \tag{G.2}$$

where $[\mu_a \quad \mu_b]$ was found in (C.6) (replace A by r_s) and we reshape μ_1' to the form of a column vector, denoted by μ_1. A symbol error is made if the square-law detector output of the jammed branch exceeds that of the signal branch, i.e., if ${\mu_1}^T A \mu_1 < 0$, where A was defined in (3.5).

Finally, the conditional SER is found by averaging over the transmitted symbol i, the jammed symbol n, and the previous symbol m, integrating over the $L+1$ random phases, and multiplying by the probability that the M-ary band with the keyed tone is jammed, μ, found in (F.2), as

$$\begin{aligned} P_1 =& \frac{\mu}{M^3(2\pi)^{L+1}} \sum_{i=1}^{M} \sum_{n=1,n\neq i}^{M} \sum_{m=1}^{M} \int_0^{2\pi} \cdots \int_0^{2\pi} \int_0^{2\pi} \left[1 - u({\mu_1}^T A \mu_1)\right] d\theta_1 \ldots d\theta_L d\theta_J \\ =& \frac{1}{E_b/\eta_J} \cdot \frac{\alpha_2 L}{(2\pi)^{L+1} M^2 \log_2 M} \sum_{i=1}^{M} \sum_{n=1,n\neq i}^{M} \sum_{m=1}^{M} \int_0^{2\pi} \cdots \int_0^{2\pi} \int_0^{2\pi} 1 - u({\mu_1}^T A \mu_1) d\theta_1 \ldots d\theta_L d\theta_J. \end{aligned} \tag{G.3}$$

The other case is that the jammed hop is not the last one. We assume the l^{th} hop is jammed where $1 \leqslant l \leqslant L-1$. It is easy to see that the performance is not a function of l. The filter output of the jamming waveform in terms of the in-phase and quadrature components is μ_{aJ} for the l^{th} hop, and

$$\mu_{bJ} = r_j \begin{bmatrix} m'_{ni} & -\mu'_{ni} \\ \mu'_{ni} & m'_{ni} \\ m'_{nn} & -\mu'_{nn} \\ \mu'_{nn} & m'_{nn} \end{bmatrix} \begin{bmatrix} \cos\theta_J \\ \sin\theta_J \end{bmatrix} \tag{G.4}$$

for the $l+1^{st}$ hop. The filter output of the signal plus jamming waveform is

$$\mu_2' \triangleq \begin{bmatrix} \mu_a & \mu_b \end{bmatrix} + \begin{bmatrix} 0_{4\times(l-1)} & \mu_{aJ} & \mu_{bJ} & 0_{4\times(L-1-l)} \end{bmatrix}, \tag{G.5}$$

$1 \leqslant l \leqslant L-1$, and we reshape μ_2' to the form of a column vector, denoted by μ_2. The conditional SER, P_2, can be found using (G.3) – just replace μ_1 by μ_2.

Appendix H

GFSK system with 2-pole BPF detection

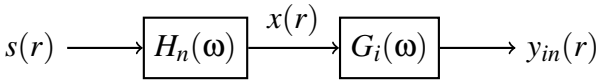

Figure K1: Signal filtering (Gaussian & 2-pole)

We start by filtering an isolated rectangular pulse cosine wave with frequency f_i and phase θ through a 2-pole BPF centered at frequency f_n, and a Gaussian filter centered at frequency f_i. We use lowpass equivalent filtering for simplicity. The input signal can be expressed as a function of the normalized time $r = t/T$ as

$$s(r) = \cos(\omega_i r T + \theta) P_{\frac{1}{2}}\left(r - \frac{1}{2}\right), \tag{H.1}$$

where T is the symbol duration, and the lowpass equivalent signal is given by

$$s_{lp}(r) = P_{\frac{1}{2}}\left(r - \frac{1}{2}\right). \tag{H.2}$$

The impulse response of the n^{th} 2-pole BPF is

$$\begin{aligned} h_n(t) &= \pi W e^{-\pi W t}\cos(\omega_n t)u(t) \\ &= \frac{\pi z}{T}e^{-\pi z t/T}\cos(\omega_i - \Delta\omega_{in}t)u(t) \\ &= \frac{\pi z}{T}e^{-\pi z t/T}u(t)[\cos\Delta\omega_{in}t\cos\omega_i t + \sin\Delta\omega_{in}t\sin\omega_i t], \end{aligned} \tag{H.3}$$

and the lowpass equivalent impulse response of the filter is given by

$$\begin{aligned} h_{lp}(t) &= \frac{\pi z}{T}e^{-\pi z t/T}u(t)\left(\cos\Delta\omega_{in}t + j\sin\Delta\omega_{in}t\right) \\ &= \frac{\pi z}{T}e^{-\pi z t/T + j\Delta\omega_{in}t}u(t) \\ \Rightarrow h_{lp}(r) &= \frac{\pi z}{T}e^{[-\pi z + j2\pi(i-n)h]r}u(r) \end{aligned} \tag{H.4}$$

where

$$\Delta\omega_{in} \triangleq \omega_i - \omega_n = 2\pi(f_i - f_n) \Rightarrow \Delta\omega_{in}T = 2\pi(i-n)h. \tag{H.5}$$

Therefore, the lowpass equivalent output the rectangular pulse through the 2-pole BPF is given by

$$\begin{aligned} x_{lp}(r) &= T\cdot s_{lp}(r) * h_{lp}(r) \\ &= T\int_{-\infty}^{\infty}\frac{\pi z}{T}e^{[-\pi z + j2\pi(i-n)h]\tau}u(\tau)P_{\frac{1}{2}}\left(r-\tau-\frac{1}{2}\right)d\tau \\ &= \pi z u(r)\int_{\max\{0,r-1\}}^{r} e^{[-\pi z + j2\pi(i-n)h]\tau}d\tau \\ &= \pi z u(r)\cdot\frac{e^{[-\pi z + j2\pi(i-n)h]\tau}\Big|_{\max\{0,r-1\}}^{r}}{-\pi z + j2\pi(i-n)h} \\ &= \frac{z}{z-2j(i-n)h}\times\begin{cases} 1-e^{-\pi z r + j2\pi(i-n)hr}, & 0\leqslant r\leqslant 1 \\ (e^{\pi z - j2\pi(i-n)h}-1)e^{-\pi z r + j2\pi(i-n)hr}, & r\geqslant 1 \end{cases} \end{aligned} \tag{H.6}$$

and the corresponding bandpass output is given by

$$x(r) = \Re\{x_{lp}(r)e^{-j(\omega_i rT+\theta)}\}. \tag{H.7}$$

Now we add the Gaussian filter. Using the integral [55]

$$\int e^{-\frac{x^2}{2}+jbx-cx}dx = \sqrt{\frac{\pi}{2}}e^{-\frac{(b+jc)^2}{2}}\,\mathrm{erf}\left(\frac{-jb+c+x}{\sqrt{2}}\right), \tag{H.8}$$

where $\mathrm{erf}(\cdot)$ is the error function. We further define

$$\lambda \triangleq \frac{\delta}{T} = \frac{\sqrt{\ln 2}}{2\pi z_g}. \tag{H.9}$$

Then, we can find the lowpass equivalent output of the Gaussian filter as

$$
\begin{aligned}
&y_{lp}(r) = T \cdot x_{lp}(r) * g_{lp}(r) \\
&= \int_0^1 \frac{z\left(1-e^{[-\pi z+j2\pi(i-n)h]\tau}\right)}{z-2j(i-n)h} \frac{e^{-\frac{(r-\tau)^2}{2\lambda^2}}}{\sqrt{2\pi}\lambda} d\tau + \int_1^\infty \frac{z\left(e^{\pi z-j2\pi(i-n)h}-1\right)e^{[-\pi z+j2\pi h]\tau}}{z-2j(i-n)h} \frac{e^{-\frac{(r-\tau)^2}{2\lambda^2}}}{\sqrt{2\pi}\lambda} d\tau \\
&= \frac{z}{\sqrt{2\pi}\,[z-2j(i-n)h]} \left[\int_{-\frac{r}{\lambda}}^{\frac{1-r}{\lambda}} e^{-\frac{x^2}{2}} - e^{-\frac{x^2}{2}+(-\pi z+j2\pi(i-n)h)(\lambda x+r)} dx \quad \left(x=\frac{\tau-r}{\lambda}\right) \right. \\
&\left. + \left(e^{\pi z-j2\pi(i-n)h}-1\right) \int_{\frac{1-r}{\lambda}}^{\infty} e^{-\frac{x^2}{2}+(-\pi z+j2\pi(i-n)h)(\lambda x+r)} dx \right] \\
&= \frac{z}{\sqrt{2\pi}\,[z-2j(i-n)h]} \left[\sqrt{2\pi}\left[\Phi\left(\frac{1-r}{\lambda}\right)-\Phi\left(\frac{-r}{\lambda}\right)\right] - e^{-\pi z r+j2\pi(i-n)hr}\sqrt{\frac{\pi}{2}}e^{-\frac{(2\pi(i-n)h\lambda+j\pi z\lambda)^2}{2}} \right. \\
&\left[\operatorname{erf}\left(\frac{-j2\pi(i-n)h\lambda+\pi z\lambda+\frac{1-r}{\lambda}}{\sqrt{2}}\right) - \operatorname{erf}\left(\frac{-j2\pi(i-n)h\lambda+\pi z\lambda-\frac{r}{\lambda}}{\sqrt{2}}\right) \right] \\
&+ \left(e^{\pi z-j2\pi(i-n)h}-1\right) e^{-\pi z r+j2\pi(i-n)hr}\sqrt{\frac{\pi}{2}}e^{-\frac{(2\pi(i-n)h\lambda+j\pi z\lambda)^2}{2}} \\
&\left. \left[1-\operatorname{erf}\left(\frac{-j2\pi(i-n)h\lambda+\pi z\lambda+\frac{1-r}{\lambda}}{\sqrt{2}}\right)\right]\right] \\
&= \frac{z}{z-2j(i-n)h} \left[\Phi\left(\frac{1-r}{\lambda}\right)-\Phi\left(\frac{-r}{\lambda}\right) - \frac{1}{2}e^{-\frac{(2\pi(i-n)h\lambda+j\pi z\lambda)^2}{2}+(-\pi z+j2\pi(i-n)h)r} \right. \\
&\left[\operatorname{erf}\left(\frac{-j2\pi(i-n)h\lambda+\pi z\lambda+\frac{1-r}{\lambda}}{\sqrt{2}}\right) - \operatorname{erf}\left(\frac{-j2\pi(i-n)h\lambda+\pi z\lambda-\frac{r}{\lambda}}{\sqrt{2}}\right) \right] \\
&\left. + \frac{e^{\pi z-j2\pi(i-n)h}-1}{2} e^{-\frac{(2\pi(i-n)h\lambda+j\pi z\lambda)^2}{2}+(-\pi z+j2\pi(i-n)h)r} \left[1-\operatorname{erf}\left(\frac{-j2\pi(i-n)h\lambda+\pi z\lambda+\frac{1-r}{\lambda}}{\sqrt{2}}\right)\right]\right]
\end{aligned}
\tag{H.10}
$$

and the corresponding bandpass output signal is given by

$$
\begin{aligned}
y_{in}(r) =& \Re\{y_{lp}(r)e^{-j(\omega_i rT+\theta_1)}\} \\
=& \Re\{y_{lp}(r)\}\cos(\omega_i rT+\theta_1) + \Im\{y_{lp}(r)\}\sin(\omega_i rT+\theta_1) \\
\triangleq& m_{in}(r)\cos(\omega_i rT+\theta_1) + \mu_{in}(r)\sin(\omega_i rT+\theta_1),
\end{aligned}
\tag{H.11}
$$

where θ_1 is the phase associated with the transmitted symbol.

Now that we know the output of signal with frequency f_i through branch "n", $y_{in}(r)$, we can find the output of the previous pulse with frequency f_{m_1} through branch "n", $y_{m_1 n}(r)$, in a similar manner, to be

$$\begin{aligned}
&y_{m_1 n}(r+1) \\
=&\Re\{y_{lp}(r+1)e^{-j(\omega_{m_1}(r+1)T+\theta_0)}\} \\
=&\Re\{y_{lp}(r+1)\}\cos(\omega_{m_1}(r+1)T+\theta_0)+\Im\{y_{lp}(r+1)\}\sin(\omega_{m_1}(r+1)T+\theta_0) \\
=&m_{m_1 n}(r+1)\cos(\omega_i rT+\Delta\omega_{m_1 i}rT+\omega_{m_1}T+\theta_0) \\
&+\mu_{m_1 n}(r+1)\sin(\omega_i rT+\Delta\omega_{m_1 i}rT+\omega_{m_1}T+\theta_0) \\
\triangleq&m_{m_1 n}(r+1)\cos(\omega_i rT+X)+\mu_{m_1 n}(r+1)\sin(\omega_i rT+X),
\end{aligned} \tag{H.12}$$

where

$$X \triangleq \Delta\omega_{m_1 i}rT+\omega_{m_1}T+\theta_0, \tag{H.13}$$

and θ_0 is the phase associated with the previous transmitted symbol. Note that we can assume $\theta_0 = -\Delta\omega_{m_1 i}rT-\omega_{m_1}T \Rightarrow X = 0$ without loss of generality. Letting $X = 0$ in (H.12) yields

$$y_{m_1 n}(r+1) = m_{m_1 n}(r+1)\cos(\omega_i rT). \tag{H.14}$$

Similarly, for the future pulse that has frequency f_{m_2} and phase θ_2, the bandpass output is given

by

$$
\begin{aligned}
& y_{m_2 n}(r-1) \\
=& \Re\{y_{lp}(r-1) e^{-j(\omega_{m_2}(r-1)T+\theta_2)}\} \\
=& \Re\{y_{lp}(r-1)\}\cos(\omega_{m_2}(r-1)T+\theta_2) + \Im\{y_{lp}(r-1)\}\sin(\omega_{m_2}(r-1)T+\theta_2) \\
=& m_{m_2 n}(r-1)\cos(\omega_i rT + \Delta\omega_{m_2 i} rT - \omega_{m_2} T + \theta_2) \\
& + \mu_{m_2 n}(r-1)\sin(\omega_i rT + \Delta\omega_{m_2 i} rT - \omega_{m_2} T + \theta_2) \\
\triangleq& m_{m_2 n}(r-1)\cos(\omega_i rT + Y) + \mu_{m_2 n}(r-1)\sin(\omega_i rT + Y),
\end{aligned}
\tag{H.15}
$$

where

$$
Y \triangleq \Delta\omega_{m_2 i} rT - \omega_{m_2} T + \theta_2. \tag{H.16}
$$

Note that since $\theta_2 \sim U[0, 2\pi]$, for any fixed sampling time r, the trigonometries of $Y = \Delta\omega_{m_2 i} rT - \omega_{m_2} T + \theta_2$ are essentially the same as those of θ_2, and thus we can replace Y with θ_2 in (H.15) when calculating the average error rate, where we need to integrate out θ_2. Letting $Y = \theta_2$ yields

$$
y_{m_2 n}(r-1) = m_{m_2 n}(r-1)\cos(\omega_i rT + \theta_2) + \mu_{m_2 n}(r-1)\sin(\omega_i rT + \theta_2). \tag{H.17}
$$

Finally, the bandpass output signal of three consecutive pulses of frequencies f_i (current symbol), f_{m_1} previous symbol, and f_{m_2} (future symbol) coming through the 2-pole BPF whose center frequency is f_n, is the superposition of the three bandpass output signals $y_{in}(r), y_{m_1 n}(r+1)$

and $y_{m_2n}(r-1)$, and is given by

$$\begin{aligned}
y_{in}^{m_1m_2}(r) =& y_{in}(r)+y_{m_1n}(r+1)+y_{m_2n}(r-1)\\
=&[m_{in}(r)\cos\theta_1+\mu_{in}(r)\sin\theta_1+m_{m_1n}(r+1)\\
&+m_{m_2n}(r-1)\cos\theta_2+\mu_{m_2n}(r-1)\sin\theta_2]\cos\omega_i rT\\
&+[-m_{in}(r)\sin\theta_1+\mu_{in}(r)\cos\theta_1+\mu_{m_1n}(r+1)\\
&-m_{m_2n}(r-1)\sin\theta_2+\mu_{m_2n}(r-1)\cos\theta_2]\sin\omega_i rT\\
\triangleq& I_{in}^{m_1m_2}(r)\cos\omega_i rT+Q_{in}^{m_1m_2}(r)\sin\omega_i rT\\
=&[I_{in}^{m_1m_2}(r)\cos(2\pi(i-n)hr)+Q_{in}^{m_1m_2}(r)\sin(2\pi(i-n)hr)]\cos(\omega_n rT)\\
&+[-I_{in}^{m_1m_2}(r)\sin(2\pi(i-n)hr)+Q_{in}^{m_1m_2}(r)\cos(2\pi(i-n)hr)]\sin(\omega_n rT),
\end{aligned} \tag{H.18}$$

where the in-phase and quadrature components are defined as

$$\begin{aligned}
I_{in}^{m_1m_2}(r) =& m_{m_1n}(r+1)+m_{in}(r)\cos\theta_1+\mu_{in}(r)\sin\theta_1\\
&+m_{m_2n}(r-1)\cos\theta_2+\mu_{m_2n}(r-1)\sin\theta_2,\\
Q_{in}^{m_1m_2}(r) =& \mu_{m_1n}(r+1)-m_{in}(r)\sin\theta_1+\mu_{in}(r)\cos\theta_1\\
&-m_{m_2n}(r-1)\sin\theta_2+\mu_{m_2n}(r-1)\cos\theta_2.
\end{aligned} \tag{H.19}$$

Note that (H.19) is a function of θ_1 and θ_2, both uniformly distributed between 0 and 2π. Then, the parameters A_1, A_2, θ_1 and θ_2 in (**??**) can be represented as

$$\begin{aligned}
A_1 &= (A_{ii}^{m_1m_2})^2 = A^2\left([I_{ii}^{m_1m_2}(r)]^2+[Q_{ii}^{m_1m_2}(r)]^2\right),\\
\theta_1 &= \theta_{ii}^{m_1m_2} = \tan^{-1}\left[\frac{Q_{ii}^{m_1m_2}(r)}{I_{ii}^{m_1m_2}(r)}\right],\\
A_2 &= (A_{in}^{m_1m_2})^2 = A^2\left([I_{in}^{m_1m_2}(r)]^2+[Q_{in}^{m_1m_2}(r)]^2\right),\\
\theta_2 &= \theta_{in}^{m_1m_2} = \tan^{-1}\left[\frac{-I_{in}^{m_1m_2}(r)\sin(2\pi(i-n)hr)+Q_{in}^{m_1m_2}(r)\cos(2\pi(i-n)hr)}{I_{in}^{m_1m_2}(r)\cos(2\pi(i-n)hr)+Q_{in}^{m_1m_2}(r)\sin(2\pi(i-n)hr)}\right],
\end{aligned} \tag{H.20}$$

where again we use the four-quadrant definition of $\tan^{-1}(\cdot)$.

The output of a rectangular pulse through a Gaussian filter is

$$\begin{aligned} s(t) &= s_{lp}(t) * g_{lp}(t) \\ &= P_{\frac{T}{2}}(t - \frac{T}{2}) * \frac{e^{-\frac{t^2}{2\delta^2}}}{\sqrt{2\pi}\delta} \\ &= \Phi\left(\frac{2\pi z_g(1-t/T)}{\sqrt{\ln 2}}\right) - \Phi\left(-\frac{2\pi z_g t/T}{\sqrt{\ln 2}}\right), \\ \Rightarrow s(r) &= \Phi\left(\frac{1-r}{\lambda}\right) - \Phi\left(-\frac{r}{\lambda}\right), \end{aligned} \tag{H.21}$$

where $\lambda = \frac{\sqrt{\ln 2}}{2\pi z_g}$ was defined in (H.9), and $\Phi(\cdot)$ is the CDF of the standard normal distribution, and thus the received symbol energy is given by

$$\begin{aligned} E_s &= \frac{A^2 T}{2} \int_{-\infty}^{\infty} s^2(r) dr \\ &= \frac{A^2 T}{2} \int_{-\infty}^{\infty} \left[\Phi\left(\frac{1-r}{\lambda}\right) - \Phi\left(-\frac{r}{\lambda}\right)\right]^2 dr \end{aligned} \tag{H.22}$$

and the received bit energy is $E_b = E_s / \log_2 M$.

Finally, the filtered noise power σ^2, the normalized complex cross-covariance ρ and the corresponding phase $\phi = \angle\rho$ when "i" is the signal branch and "n" is the ICI branch, were found in [34] as

$$\begin{aligned} &\sigma^2 = \frac{\eta_0 \pi z}{2T}, \\ &|\rho| = \frac{z}{\sqrt{z^2 + ((i-n)h)^2}}, \\ &\phi = \angle\rho = \tan^{-1}\left[\frac{z\sin(2\pi(i-n)hr) - (i-n)h\cos(2\pi(i-n)hr)}{z\cos(2\pi(i-n)hr) + (i-n)h\sin(2\pi(i-n)hr)}\right]. \end{aligned} \tag{H.23}$$

Bibliography

[1] M. S. Mahmoud, A. A. H. Mohamad, "A Study of Efficient Power Consumption Wireless Communication Techniques 1 Modules for Internet of Things (IoT) Applications," *Advances in Internet of Things*, vol. 06, no. 02, pp. 19–29, Jan. 2016.

[2] Borja Martinez, Mrius Montn, Ignasi Vilajosana, Xavier Vilajosana, "Early Scavenger Dimensioning in Wireless Industrial Monitoring Applications," *IEEE Internet Things J.*, vol. 3, no. 2, pp. 170–178, Apr. 2016.

[3] S. Bi, C.K. Ho, R. Zhang, "Wireless powered communication: opportunities and challenges," *IEEE Commun. Mag.*, vol. 53, no. 4, pp. 117–125, Apr. 2015.

[4] David D. Wentzloff, Abdullah Alghaihab, Jaeho Im, "Ultra-Low Power Receivers for IoT Applications: A Review," in Proc. *IEEE Custom Integrated Circuits Conference (CICC)*, Mar. 2020.

[5] Rajeev Piyare, Amy L. Murphy, Csaba Kiraly, Pietro Tosato, Davide Brunelli, "Ultra Low Power Wake-Up Radios: A Hardware and Networking Survey," *IEEE Communications Surveys & Tutorials,* Vol. 19, No. 4, Fourth Quarter 2017.

[6] H. R. Kooshkaki, P. P. Mercier, "A 0.55mW Fractional-N PLL with a DC-DC Powered Class-D VCO Achieving Better than -66dBc Fractional and Reference Spurs for NB-IoT," in Proc. *IEEE Custom Integrated Circuits Conference (CICC)*, Mar. 2020.

[7] K. Spyridis and C. Robertson, "Performance simulation and analysis of M-ary frequency-shift keying with Reed Solomon encoding, noncoherent demodulation, and hybrid soft decision-hard decision decoding," 2011 - *MILCOM 2011 Military Communications Conference*, Baltimore, MD, 2011, pp. 610-615, doi: 10.1109/MILCOM.2011.6127741.

[8] C. Schurgers, O. Aberthorne, and M. B. Srivastava, "Modulation scaling for energy aware communication systems," *International Symposium on Low Power Electronics and Design*, pp. 96–99, 2001.

[9] R. Min, A. Chadrakasan, "A framework for energy-scalable communication in high-density wireless networks," *International Symposium on Low Power Electronics Design*, pp. 36–41, 2002.

[10] S. Cui, A. J. Goldsmith, A. Bahai, "Energy-constrained Modulation Optimization for Coded Systems," *Proceedings of Globecom'03*, San Francisco, USA, 2003.

[11] Shuguang Cui, A. J. Goldsmith and A. Bahai, "Energy-constrained modulation optimization," in *IEEE Transactions on Wireless Communications*, vol. 4, no. 5, pp. 2349-2360, Sept. 2005, doi: 10.1109/TWC.2005.853882.

[12] J. Sun, I. S. Reed, "Performance of MDPSK, MPSK and noncoherent FSK in Rician wireless fading channels," *IEEE Trans. Commun.*, vol. 47, no. 6, pp. 813–815, June 1999.

[13] G. M. Vitetta, U. Mengali, D. P. Taylor, "An error probability formula for noncoherent orthogonal binary FSK with dual diversity on correlated Rician channels," *IEEE Commun. Lett.*, vol. 3, no. 2, pp. 43–45, Feb. 1999.

[14] J. Proakis, *Digital Communications*, 2nd ed. New York: McGraw-Hill, 1989.

[15] M Schwartz, W Bennett and S Stein, *Communication Systems and Techniques*, McGraw-Hill, 1966.

[16] M. K. Simon and M.-S. Alouini, *Digital communication over fading channels*, vol. 95. John Wiley & Sons, 2005.

[17] R. A. Khalona, "Optimum Reed-Solomon codes for M-ary FSK modulation with hard decision decoding in Rician-fading channels", *IEEE Trans. Commun.*, vol. 44, no. 4, pp. 409–412, Apr. 1996.

[18] E. Lutz, "Code and interleaver design for data transmission over fading channels," in *Proc. IEEE GLOBECOM*, Atlanta, GA, Nov. 1984, pp. 381–386.

[19] A. Pouttu, H. Saarnisaari and S. Glisic, "Noncoherent m MCSK-m MFSK Modulation in Rayleigh Fading Channel," *MILCOM 2006 - 2006 IEEE Military Communications conference*, Washington, DC, 2006, pp. 1-5, doi: 10.1109/MILCOM.2006.302022.

[20] S. Ahmed, R. G. Maunder, L. Yang and L. Hanzo, "Iterative Detection of Unity-Rate Precoded FFH-MFSK and Irregular Variable-Length Coding," in *IEEE Transactions on Vehicular Technology*, vol. 58, no. 7, pp. 3765-3770, Sept. 2009, doi: 10.1109/TVT.2009.2013989.

[21] T. C. Royster, "Current designs for fast frequency hopping with MFSK," *2011 - MILCOM 2011 Military Communications Conference*, Baltimore, MD, 2011, pp. 543-548, doi: 10.1109/MILCOM.2011.6127728.

[22] Y. Liu, "Diversity-Combining and Error-Correction Coding for FFH/MFSK Systems over Rayleigh Fading Channels under Multitone Jamming," in *IEEE Transactions on Wireless Communications*, vol. 11, no. 2, pp. 771-779, February 2012, doi: 10.1109/TWC.2011.120911.110462.

[23] J. Zhang, K. C. Teh and K. H. Li, "Error probability analysis of FFH/MFSK receivers over frequency-selective Rician-fading channels with partial-band-noise jamming," in *IEEE Transactions on Communications*, vol. 57, no. 10, pp. 2880-2885, October 2009, doi: 10.1109/TCOMM.2009.10.080114.

[24] L. Le, K. C. Teh and K. H. Li, "Jamming Rejection Using FFH/MFSK ML Receiver Over Fading Channels With the Presence of Timing and Frequency Offsets," in *IEEE Transactions on Information Forensics and Security*, vol. 8, no. 7, pp. 1195-1200, July 2013, doi: 10.1109/TIFS.2013.2264053.

[25] Y. Han and K. C. Teh, "Error probabilities and performance comparisons of various FFH/MFSK receivers with multitone jamming," in *IEEE Transactions on Communications*, vol. 53, no. 5, pp. 769-772, May 2005, doi: 10.1109/TCOMM.2005.847139.

[26] Y. Han and K. C. Teh, "Performance study of suboptimum maximum-likelihood receivers for FFH/MFSK systems with multitone jamming over fading channels," in *IEEE Transactions on Vehicular Technology*, vol. 54, no. 1, pp. 82-90, Jan. 2005, doi: 10.1109/TVT.2004.838895.

[27] T. Wu, "A Suboptimal Maximum-Likelihood Receiver for FFH/BFSK Systems With Multitone Jamming Over Frequency-Selective Rayleigh-Fading Channels," in *IEEE Transactions on Vehicular Technology*, vol. 57, no. 2, pp. 1316-1322, March 2008, doi: 10.1109/TVT.2007.905623.

[28] Gang Huo and M. -. Alouini, "Another look at the BER performance of FFH/BFSK with product combining over partial-band jammed Rayleigh-fading channels," in IEEE Transactions on Vehicular Technology, vol. 50, no. 5, pp. 1203-1215, Sept. 2001, doi: 10.1109/25.950321.

[29] Y. T. Su and Li-Der Jeng, "Antijam capability analysis of RS-coded slow frequency-hopped systems," in *IEEE Transactions on Communications*, vol. 48, no. 2, pp. 270-281, Feb. 2000, doi: 10.1109/26.823560.

[30] S. Ahmed, L. Yang and L. Hanzo, "Erasure Insertion in RS-Coded SFH MFSK Subjected to Tone Jamming and Rayleigh Fading," in *IEEE Transactions on Vehicular Technology*, vol. 56, no. 6, pp. 3563-3571, Nov. 2007, doi: 10.1109/TVT.2007.901861.

[31] Y. Shi, K. An and Y. Li, "Index Modulation Based Frequency Hopping: Anti-Jamming Design and Analysis," in *IEEE Transactions on Vehicular Technology*, vol. 70, no. 7, pp. 6930-6942, July 2021, doi: 10.1109/TVT.2021.3087640.

[32] H. Jung, B. V. Nguyen, I. Song and K. Kim, "Design of Anti-Jamming Waveforms for Time-Hopping Spread Spectrum Systems in Tone Jamming Environments," in *IEEE Transactions on Vehicular Technology*, vol. 69, no. 1, pp. 728-737, Jan. 2020, doi: 10.1109/TVT.2019.2954070.

[33] Heung-Gyoon Ryu, Yingshan Li and Jin-Soo Park, "Effects of frequency instability caused by phase noise on the performance of the fast FH communication system," in *IEEE Transactions on Vehicular Technology*, vol. 53, no. 5, pp. 1626-1632, Sept. 2004, doi: 10.1109/TVT.2004.832409.

[34] Y. Xiang and L. B. Milstein, "Design and Performance Analysis for Short Range, Very Low-Power Communications," in *IEEE Transactions on Communications*, vol. 68, no. 9, pp. 5938-5950, Sept. 2020, doi: 10.1109/TCOMM.2020.3005454.

[35] Ali Nikoofard, Hamed Abbasi Zadeh, Patrick P. Mercier, "A 0.6-mW 16-FSK Receiver Achieving a Sensitivity of 103 dBm at 100 kb/s", *Solid-State Circuits IEEE Journal of*, vol. 56, no. 4, pp. 1299-1309, 2021.

[36] K. Binmore, 2007, *Game theory a very short introduction*, Oxford University Press.

[37] H. Ma and M. Poole, "Error-Correcting Codes Against the Worst-Case Partial-Band Jammer," in *IEEE Transactions on Communications*, vol. 32, no. 2, pp. 124-133, February 1984, doi: 10.1109/TCOM.1984.1096036.

[38] J. Wang and M. Moeneclaey, "Multiple hops/symbol FFH-SSMA with MFSK modulation and Reed-Solomon coding for indoor radio," in *IEEE Transactions on Communications*, vol. 41, no. 5, pp. 793-801, May 1993, doi: 10.1109/26.225494.

[39] R. Viswanathan and K. Taghizadeh, "Diversity combining in FH/BFSK systems to combat partial band jamming," in *IEEE Transactions on Communications*, vol. 36, no. 9, pp. 1062-1069, Sept. 1988, doi: 10.1109/26.7518.

[40] R. C. Robertson and Kang Yeun Lee, "Performance of fast frequency-hopped MFSK receivers with linear and self-normalization combining in a Rician fading channel with partial-band interference," in *IEEE Journal on Selected Areas in Communications*, vol. 10, no. 4, pp. 731-741, May 1992, doi: 10.1109/49.136068.

[41] M. K. Simon, J. K. Omura, R. A. Scholtz and B. K. Levitt, *Spread Spectrum Communications Handbook*

[42] R. E. Ziemer and R. L. Peterson, *Digital Communications and Spread Spectrum Systems*, New York:Macmillan Publishing Company, 1985.

[43] Y. Xiang and L. B. Milstein, "Design of an ultra-low power MFSK system in the presence of jamming," MILCOM 2021 - 2021 IEEE Military Communications Conference (MILCOM), 2021, pp. 652-657, doi: 10.1109/MILCOM52596.2021.9653041.

[44] A. M. Mathai and Serge B. Provost *Quadratic Forms in Random Variables, Theory and Applications*, 1992.

[45] A. A. Ali, "Worst-case partial-band noise jamming of Rician fading channels," in *IEEE Transactions on Communications*, vol. 44, no. 6, pp. 660-662, June 1996, doi: 10.1109/26.506381.

[46] Y. Xiang and L. B. Milstein, "On the use of FFH-MFSK for ultra-low power communications", submitted to IEEE Transactions on Vehicular Technology.

[47] B. Yu, L. Yang and C. Chong, "Optimized Differential GFSK Demodulator," in *IEEE Transactions on Communications*, vol. 59, no. 6, pp. 1497-1501, June 2011, doi: 10.1109/TCOMM.2011.041111.100010A.

[48] B. Chi, J. Yao, P. Chiang and Z. Wang, "A 0.18-μm CMOS GFSK Analog Front End Using a Bessel-Based Quadrature Discriminator With On-Chip Automatic Tuning," in *IEEE Transactions on Circuits and Systems I: Regular Papers*, vol. 56, no. 11, pp. 2498-2510, Nov. 2009, doi: 10.1109/TCSI.2009.2015728.

[49] R. -F. Ye, T. -S. Horng and J. -M. Wu, "Ultralow Power Injection-Locked GFSK Receiver for Short-Range Wireless Systems," in *IEEE Transactions on Circuits and Systems II: Express Briefs*, vol. 59, no. 11, pp. 706-710, Nov. 2012, doi: 10.1109/TCSII.2012.2220695.

[50] Tai-Cheng Lee and Chin-Chi Chen, "A mixed-signal GFSK demodulator for Bluetooth," in *IEEE Transactions on Circuits and Systems II: Express Briefs*, vol. 53, no. 3, pp. 197-201, March 2006, doi: 10.1109/TCSII.2005.858320.

[51] S. Hong, A. K. George, D. Im, M. Je and J. Lee, "A 1.0 V, 5.4 pJ/bit GFSK Demodulator Based on an Injection Locked Ring Oscillator for Low-IF Receivers," in *IEEE Access*, vol. 8, pp. 185209-185217, 2020, doi: 10.1109/ACCESS.2020.3029863.

[52] M. Silva Pereira, J. Caldinhas Vaz, C. Azeredo Leme, J. T. de Sousa and J. Costa Freire, "A 170 μA All-Digital GFSK Demodulator With Rejection of Low SNR Packets for Bluetooth-LE," in *IEEE Microwave and Wireless Components Letters*, vol. 26, no. 6, pp. 452-454, June 2016, doi: 10.1109/LMWC.2016.2562639.

[53] D. Mototolea, R. Youssef, E. Radoi and I. Nicolaescu, "Non-Cooperative Low-Complexity Detection Approach for FHSS-GFSK Drone Control Signals," in *IEEE Open Journal of the Communications Society*, vol. 1, pp. 401-412, 2020, doi: 10.1109/OJCOMS.2020.2984312.

[54] M. Shimizu, N. Aoki, K. Shirakawa, Y. Tozawa, N. Okubo and Y. Daido, "New method of analyzing BER performance of GFSK with postdetection filtering," in IEEE Transactions on Communications, vol. 45, no. 4, pp. 429-436, April 1997, doi: 10.1109/26.585918.

[55] Wolfram Alpha LLC. 2016. Wolfram—Alpha. https://www.wolframalpha.com/input?i=integral+e%5E%28-x%5E2%2F2-i*b*x%2Bc*x%29(access April 22, 2022).